



# Light-matter interaction with atomic ensembles

Brice Dubost

## ► To cite this version:

Brice Dubost. Light-matter interaction with atomic ensembles. Quantum Physics [quant-ph]. Université Paris-Diderot - Paris VII; Universitat Politècnica de Catalunya, 2012. English. NNT: . tel-00818499

**HAL Id: tel-00818499**

<https://theses.hal.science/tel-00818499>

Submitted on 27 Apr 2013

**HAL** is a multi-disciplinary open access archive for the deposit and dissemination of scientific research documents, whether they are published or not. The documents may come from teaching and research institutions in France or abroad, or from public or private research centers.

L'archive ouverte pluridisciplinaire **HAL**, est destinée au dépôt et à la diffusion de documents scientifiques de niveau recherche, publiés ou non, émanant des établissements d'enseignement et de recherche français ou étrangers, des laboratoires publics ou privés.

**Université Paris Diderot, Paris 7**  
**Laboratoire Matériaux et Phénomènes Quantiques**  
**CNRS UMR 7162**

Thèse réalisée en co-tutelle avec  
**Universitat Politècnica de Catalunya. BarcelonaTech.**  
**Institut de Ciències Fotòniques**

**Thèse pour obtenir le diplôme de  
docteur de l'Université Paris Diderot, Paris 7  
en sciences**

**Par : BRICE DUBOST**

Sous la direction de  
**Dr. GUIBAL Samuel (Université Paris Diderot, Paris 7)**  
**Prof. MITCHELL W. Morgan (Universitat Politècnica de  
Catalunya. BarcelonaTech.)**

Sujet :  
**Interaction lumière matière avec des ensembles atomiques**

**Défendue publiquement le 26 novembre 2012**

**Jury :**

M.	<b>Julien Laurat</b>	<b>Rapporteur</b>
M.	<b>Aurélien Dantan</b>	<b>Rapporteur</b>
M.	<b>Carlo Sirtori</b>	
M.	<b>Hugues De Riedmatten</b>	

# Abstract

The study of quantum light-matter interaction with atomic ensembles is an active research area. This kind of system allows fundamental studies on measurement in the context of continuous variables, in collective entanglement and in quantum simulations. This field of research is also interesting in the context of quantum metrology, quantum networking and quantum computation. In this thesis two complementary aspects of light matter interaction with atomic ensembles have been studied with trapped ions and cold neutral atoms. The trapped ion experiment is intended to evaluate the possibility to use large ion clouds for realizing a quantum memory with long coherence times. Whereas the cold atom experiment focused on the use of quantum non demolition measurements to evaluate non-Gaussian states. This experiment is similar to quantum networking experiment currently planned.

Laser cooled trapped ions can reach a crystalline phase due to the strong Coulomb repulsion between ions. In this phase the relative positions between the ions is fixed avoiding collisions and the ions to explore magnetic field inhomogeneities which can be a source of coherence loss. At low ion number, long coherence times have been demonstrated. With large ion numbers, the trapping mechanism can induce heating of the ion cloud thus making more difficult to obtain the crystallized regime. During this thesis, large Coulomb crystals containing more than  $1 \times 10^6$  ions have been obtained and signature of electromagnetically induced transparency in such system have been obtained. This study also revealed limitations of this kind of systems which have to be further studied to allow strong light matter interaction probability with cold large ion ensembles in a regime allowing for long coherence times.

Neutral atoms systems allow strong light matter coupling probabilities but usually reduced coherence times. Quantum memories, entanglement between atoms and light, high precision magnetometry have been demonstrated with neutral atomic vapors. The system used during this thesis is designed to allow strong light matter coupling probability with detuned polarized light pulses, allowing to precisely measure the spin state of the atomic system without destruction and low noise. The measurement noise of the system is lower than the atomic noise opening the way for collective entanglement (via measurement induced spin squeezing) and ultra sensitive magnetic field measurements. This system is closely related with systems designed for quantum networking and quantum memories. Non Gaussian atomic states are a resource for quantum computation and quantum communication, in the context of atomic physics experiments, their detection can be difficult. The work presented in this thesis focuses on the detection of non Gaussian states in atomic ensembles using cumulants, and in particular their noise properties.

## Résumé

L'étude de l'interaction lumière matière avec des ensembles atomiques est un domaine de recherche actif. Ce type de système permet des études fondamentales sur la mesure dans le contexte de variables continues, l'intrication collective, et les simulations quantiques. Ce domaine de recherche est également intéressant dans le contexte de la métrologie quantique, la communication quantique et l'informatique quantique. Dans cette thèse, deux aspects complémentaires de l'interaction lumière matière avec des ensembles atomiques ont été étudiés avec des ions piégés et des atomes neutres refroidis par laser. L'expérience basée sur les ions piégés a pour but d'évaluer la possibilité d'utiliser de grands nuages d'ions afin d'obtenir une mémoire quantique possédant un long temps de cohérence. Alors que l'expérience atomes froids c'est concentrée sur l'utilisation de mesures non destructives pour détecter les états non gaussiens atomiques. Cette expérience est semblable aux expériences de communication quantique qui sont actuellement menées.

Les ions piégés refroidis par laser peuvent atteindre une phase cristalline due à la forte répulsion de Coulomb entre les ions. Dans cette phase, les positions relatives entre les ions sont fixées évitant ainsi les collisions et que les ions explorent les inhomogénéités du champ magnétique, ce qui peut être une source de décohérence. Des temps de cohérence très longs des degrés de liberté internes ont été mis en évidence avec des ions uniques. À grand nombre d'ions, le mécanisme de piegeage peut induire un réchauffement du nuage d'ions, ce qui rend plus difficile l'obtention d'un système cristallisé. Durant cette thèse, de grands cristaux de Coulomb contenant plus de  $1 \times 10^6$  ions ont été obtenus, ainsi que la signature de la transparence électromagnétiquement induite. Cette étude a également révélé les limites de ce système qui doivent être étudiées plus en profondeur afin d'obtenir une forte probabilité d'interaction avec des ensembles d'ions froids dans un système permettant de longs temps de cohérence.

Les systèmes d'atomes neutres permettent de fortes probabilités de couplage entre la lumière et la matière, mais en général, des temps de cohérence plus courts. Les mémoires quantiques, l'intrication entre les atomes et la lumière, la magnétométrie de haute précision ont été démontrés dans des expériences basées sur des vapeurs atomiques neutres. Le système utilisé dans cette thèse est conçu pour permettre une grande probabilité de couplage entre la matière et la lumière, en utilisant des impulsions de lumière polarisée, qui permettent de mesurer avec précision et de manière non destructive l'état de spin du système atomique avec un bruit faible. Le bruit de la mesure dans ce système est inférieure au bruit atomique, ce qui pourrait provoquer l'intrication collective des spins atomiques (par l'intermédiaire du spin squeezing induit par la mesure) et des mesures de champ magnétique ultra sensibles. Ce système est étroitement lié à des systèmes conçus pour la création de communication quantique et de mémoires quantiques. Les états atomiques non gaussiens représentent une ressource pour l'informatique quantique et la communication quantique, dans le cas d'expériences de physique atomique, leur détection peut être difficile. Le travail présenté dans cette thèse se concentre sur la détection des états non gaussiens dans

des ensembles atomiques en utilisant les cumulants, et en particulier le bruit associé à la mesure des cumulants.

## Resumen

El estudio de la interacción luz materia con conjuntos atómicos es un área de investigación activa. Este tipo de sistema permite fundamental estudios sobre la medición en el contexto de las variables continuas, en entrelazamiento colectiva y en las simulaciones cuánticas. Este campo de la investigación también es interesante en el contexto de la metrología cuántica, comunicación cuántica y la computación cuántica. En esta tesis dos aspectos complementarios de la interacción luz materia con conjuntos atómicos han sido estudiados con iones atrapados y átomos neutros fríos. El experimento de iones atrapados pretende evaluar la posibilidad de utilizar grandes nubes de iones para la realización de una memoria cuántica con largo tiempo de coherencia. En vez de que el experimento de átomos fríos se centró en el uso de medidas de no demolición cuántica para evaluar estados no gaussianos. Este experimento es parecido a los experimentos de comunicación cuántica que se desarrollan actualmente.

Los iones atrapados enfriados por láser pueden llegar a una fase cristalina debido a la fuerte repulsión de Coulomb entre los iones. En esta fase, las relativas posiciones entre los iones se fijan de manera a evitar las colisiones y los iones que exploran inhomogeneidades del campo magnético que puede ser una fuente de pérdida de coherencia. Con bajo número de iones, largos tiempos de coherencia han sido demostrados. Con iones numerosos, el mecanismo de captura puede inducir un calentamiento de la nube de iones, haciendo así más difícil de obtener el régimen cristalizado. Durante esta tesis, los cristales de Coulomb grandes que contiene más de  $1 \times 10^6$  iones se han obtenidos y la prueba de la transparencia inducida electromagnéticamente en tal sistema ha sido obtenida. Este estudio también reveló las limitaciones de este tipo de sistemas que tienen que ser estudiado más a fondo para obtener una fuerte probabilidad de interacción con conjuntos de iones fríos en un régimen permitiendo largos tiempos de coherencia.

Los sistemas de átomos neutros permiten fuertes probabilidades de acoplamiento luz materia, pero generalmente reduce los tiempos de coherencia. Memorias cuánticas, el entrelazamiento entre átomos y la luz, magnetometría de alta precisión han sido demostrados en experimentos relacionados con vapores atómicos neutros. El sistema utilizado en esta tesis se ha diseñado para permitir que la probabilidad de acoplamiento luz materia sea importante, con pulsos de luz polarizada, lo que permite medir con precisión el estado de espín del sistema atómico sin destrucción y con bajo ruido. La medición del ruido del sistema es más baja que el ruido atómico, lo que podría inducir el entrelazamiento colectivo de los espines atómicos (a través del squeezing de espines inducido por la medición) y mediciones de campo

magnético ultra sensibles. Este sistema está estrechamente relacionado con sistemas diseñados para la creación de comunicación cuántica y memorias cuánticas. Los estados atómicos no gaussianos constituyen un recurso para la computación cuántica y la comunicación cuántica, en el contexto de los experimentos de física atómica, su detección puede ser difícil. El trabajo presentado en esta tesis se centra en la detección de los estados no gaussianos en conjuntos atómicos utilizando cumulants, y en particular el ruido relacionado con la medición de los cumulants.



# Contents

<b>1</b>	<b>Introduction</b>	<b>11</b>
1.1	Context . . . . .	11
1.2	Organization of the manuscript . . . . .	12
<b>I</b>	<b>Towards high light matter coupling in ion Coulomb crystals</b>	<b>15</b>
<b>2</b>	<b>Introduction</b>	<b>17</b>
<b>3</b>	<b>Ion trapping and experimental overview</b>	<b>19</b>
3.1	Ion trapping and cooling . . . . .	19
3.1.1	Ion trapping in linear Paul traps . . . . .	20
3.1.2	Ion clouds at low temperature . . . . .	23
3.1.3	Ion cooling . . . . .	24
3.2	Trap . . . . .	26
3.3	Radio-frequency source . . . . .	26
3.3.1	Resonator . . . . .	26
3.3.2	Micro motion compensation . . . . .	29
3.4	Laser system . . . . .	31
3.5	Violet laser source . . . . .	32
3.5.1	Frequency stabilization . . . . .	33
3.5.2	Intensity fluctuations . . . . .	34
3.6	Infrared lock implementation . . . . .	34
3.6.1	Locking method . . . . .	34
3.6.2	Calibration and performances . . . . .	36
3.6.3	Limitations and possible improvements . . . . .	37
3.7	Frequency and polarization control . . . . .	37
3.7.1	Probe beam control . . . . .	37
3.8	Femtosecond photo-ionization laser . . . . .	40
3.9	Imaging system . . . . .	42
3.10	Magnetic field control . . . . .	43

<b>4 Large coulomb crystals</b>	<b>45</b>
4.1 Trap density measurement . . . . .	45
4.2 Improvements on the loading rate . . . . .	47
4.2.1 Strontium oven characterization . . . . .	47
4.2.2 Photo-ionization characterization . . . . .	48
4.2.3 Final loading rate . . . . .	49
Results and chapter conclusion . . . . .	50
<b>5 Isotopic enrichment</b>	<b>53</b>
5.1 Introduction . . . . .	53
5.2 Ingredients for isotopic enrichment . . . . .	54
5.2.1 Radial separation . . . . .	54
5.2.2 Radiation pressure . . . . .	54
5.3 Simulations . . . . .	56
5.3.1 Position of the problem . . . . .	56
5.3.2 Results . . . . .	57
5.4 Experimental isotope enrichment . . . . .	57
5.4.1 Endcaps electrodes control . . . . .	57
5.5 Results and limitations . . . . .	60
Chapter conclusion . . . . .	61
<b>6 Isotope-shift measurements</b>	<b>63</b>
6.1 Introduction . . . . .	63
6.2 Theoretical model . . . . .	65
6.3 Experimental results and discussion . . . . .	68
6.3.1 Experimental method . . . . .	68
Chapter conclusion . . . . .	71
<b>7 Light-matter interaction with ions</b>	<b>73</b>
7.1 Introduction . . . . .	73
7.2 Theory . . . . .	74
7.2.1 Expected absorption . . . . .	74
7.2.2 Temperature effects . . . . .	75
7.3 Absorption measurement method . . . . .	75
7.3.1 Absorption spectra with linearly polarized probe . . . . .	78
7.3.2 Large spectra and model for longitudinal oscillation . . . . .	79
7.4 EIT in a large coulomb crystal . . . . .	81
7.4.1 Optical pumping . . . . .	81
7.4.2 Electromagnetically Induced Transparency . . . . .	82
7.5 RF heating in large crystals . . . . .	84
7.5.1 Temperature from image analysis . . . . .	86
7.5.2 Absorption versus ion number . . . . .	88
Chapter conclusion . . . . .	89

<b>II Detection of non-Gaussian states in atomic ensembles</b>	<b>91</b>
<b>8 Detection of non-Gaussian states</b>	<b>95</b>
8.1 Introduction . . . . .	95
8.1.1 Non-Gaussian states . . . . .	95
8.1.2 Approach . . . . .	96
8.2 Theory . . . . .	97
8.2.1 Moments, cumulants and estimators . . . . .	97
8.2.2 Measurement noise . . . . .	98
Chapter conclusion . . . . .	99
<b>9 Experimental set-up and measurement method</b>	<b>101</b>
9.1 Experimental system . . . . .	101
9.2 State preparation . . . . .	105
9.3 Data acquisition and normalization . . . . .	108
<b>10 Noise performance of cumulant based approach</b>	<b>109</b>
10.1 Detection, Analysis and Results . . . . .	109
10.2 Optimum estimation of non-Gaussian distributions . . . . .	111
10.3 Conclusion . . . . .	112
<b>11 Conclusion</b>	<b>113</b>
<b>III Conclusion</b>	<b>115</b>
<b>Appendices</b>	<b>121</b>
<b>A Cumulants estimators and variance</b>	<b>121</b>
A.1 Fisher's k-statistics . . . . .	121
A.2 Variance of Fisher's k-statistics estimators . . . . .	124
<b>B Rubidium data</b>	<b>125</b>
B.1 Rubidium spectroscopic data . . . . .	125
<b>C Offset lock for MBR</b>	<b>127</b>
<b>D Various</b>	<b>131</b>
D.1 Branching ratios . . . . .	131
D.2 Lifetime and frequencies of low energy levels of Sr+ . . . . .	132
<b>Bibliography</b>	<b>133</b>



# Chapter 1

## Introduction

### 1.1 Context

The recent theoretical and technological advances allow to control light and atomic systems down to the quantum level. This level of control allows one to propose and implement experiments and devices using quantum properties to outperform their classical counterparts and, from a more fundamental point of view to understand quantum process which were only thought experiments a few years ago. Metrology benefits from quantum engineering both when light and atoms are used as sensors [Wilpers 02, Louchet-Chauvet 10, Gross 10, Schnabel 10], in particular in the context of magnetometry [Budker 07, Shah 10, Kominis 03], time measurements [André 04], and interferometric length measurement [Schnabel 10]. Devices based on the control of quantum properties are predicted to allow solving some computation problem faster than with classical computation and to imagine communication devices that ensure security by the law of physics instead of a computationally hard problem. These perspectives need quantum control of both light, for propagatin quantum information and matter for storing and processing quantum information. In this context, the quantum interface between light and matter [Hammerer 10] is particularly important both for writing from light to matter [Hedges 10, Longdell 05, Zhao 09b, Hosseini 11] and extracting information from matter to light.

The quantum properties of single particles and ensembles can be controlled which leads to two different, non-exclusive approaches. Single particles are simpler systems and their quantum properties are better controlled than ensembles but they can suffer from low interaction levels with the environment. Single photons are hard to detect and are difficult to couple with single atoms (or ions). On the other side, ensembles can provide strong interaction probabilities, but their quantum properties are difficult to control. In this context, the work presented in this thesis has been made following two complementary approaches: improving the light matter interaction probability with large ion ensembles and studying the measurements of non-Gaussian states in atomic ensembles.

Trapped ions are known to exhibit long coherence times and good quantum

control and detectivity. The strong Coulomb repulsion avoids collisions between trapped ions but makes high densities difficult to achieve. Neutral atoms on the other side are known for a stronger interaction probability thanks to higher atomic density but present usually smaller coherence time for the information stored in the internal degrees of freedom. The ion experiment goal is to achieve sufficiently high densities in the perspective of a quantum memory with trapped ions. The neutral atoms experiment takes advantage of the strong interaction to implement low noise quantum non demolition measurements. This system has been used to study the use of a statistical tool: the cumulants to detect non Gaussian states in atomic ensembles. Non Gaussian states are a resource for several quantum information and quantum communication tasks.

This work have been divided over two research groups: the ion trap work at the Ions Piégés et Information Quantique group in Laboratoire Matériaux et phénomènes quantiques at Université Paris Diderot and the neutral atoms experiment at Morgan Mitchell's group in Institut de Ciències Fotòniques(Barcelona).

## 1.2 Organization of the manuscript

The thesis is organized in two main parts:

1. a first part containing the work on ion ensemble and the description of the experimental techniques used on both experiments. This part covers chapter 2 to chapter 7 with the description of the experimental techniques in chapter 3. This part is divided in the following chapters:
  - Chapter 3 describes ion trapping and cooling techniques as well as the experimental set-up
  - In Chapter 4 the work performed to reach large coulomb crystals is described
  - A new, simple method for isotopic enrichment is described in Chapter 5
  - Chapter 6 Describes spectroscopic measurements performed to measure isotopic shifts in strontium, allowing better addressing of the various isotopes in the trap.
  - The measurement of light matter interaction strength as well as the limiting factors are described in Chapter 7
2. a second part describing the work on the detection of non-Gaussian states in atomic ensembles starting page 93. This part is divided in the following chapters:
  - Cumulant theory and its application to atomic non Gaussian states are presented in Chapter 8
  - Chapter 9 covers the experimental setup used and the method for producing test states

- The analysis of the noise performance of cumulants in the context of detection of non Gaussian states in atomic ensembles is presented in Chapter 10



## Part I

Towards high light matter  
coupling in ion Coulomb crystals



# Chapter 2

## Introduction

Trapped ions allowed great advances in metrology and quantum information processing. Indeed they are close to the ideal physical system, as a single ion can be trapped during days in a ultra high vacuum chamber without being significantly disturbed by the trapping potential and the collisions. Such systems have demonstrated very long coherence time of quantum superpositions stored in the internal degrees of freedom ( $> 10$  s for magnetically insensitive states and 1 ms for magnetically sensitive states) of quantum information stored in a single ion [Langer 05, Schmidt-Kaler 03], and two trapped ions have been entangled for more than 20 s [Häffner 05].

Interface between light and ions have also been demonstrated at the single photon-single ion level [Piro 11, Slodička 10] but suffers from the low light matter interaction probability. This interaction probability can be increased by the use of cavities. The collective strong coupling regime have been demonstrated in trapped ions [Herskind 09]. In this regime, the physics of the system is dominated by the interaction between ions mediated via the cavity which enhances the light field strength thus the light matter interaction. This approach which is very promising is technically difficult and, in the perspective of quantum memories suffers from a limited bandwidth due to the presence of the cavity.

Another, complementary approach is to increase the light matter interaction probability by increasing the number of ions while keeping the density reasonable without the help of a cavity. This approach is challenging because of the strong repulsion between ions, and the possibility of sample heating from the trap at large ion numbers. Previous work in the group [Removille 09a] opened the way on enhanced light matter interaction with large ensembles.

In the following, work toward greater light matter interaction with large ion ensembles will be presented. This work allowed for the measurement of significant single pass probe absorption levels ( $\approx 3\%$ ), and the signature of Electromagnetically Induced Transparency in large ion ensembles have been observed. This study allowed to identify current limitations of the system, to measure spectroscopic shifts in Strontium and to develop a new isotopic enrichment method.

This work has been performed in the Ion Piégés et Information Quantique group at Laboratoire Matériaux et Phénomènes Quantiques. The goal of the group is to

study quantum information aspects with trapped ions in two experimental contexts: large ion Coulomb crystals trapped in a 2D Paul trap and the effect of the trap design on ion heat rate in the context of sub millimetric surface traps.

In chapter 3 standard ion trapping techniques will be presented, as well as the experimental apparatus. Work performed allowing to trap million ions in a Coulomb crystal is presented in chapter 4. Isotopic enrichment method is presented in chapter 5. Spectroscopic measurements of Strontium isotopic shifts are described in chapter 6. And finally light matter interaction probability measurements and Electromagnetically Induced Transparency in large ion ensembles are presented in chapter 7.

# Chapter 3

## Ion trapping and experimental overview

In the following chapter we will present the different aspects of ion trapping and cooling and the experimental set-up allowing the formation and manipulation of large coulomb crystals.

### 3.1 Ion trapping and cooling

Ion traps, since their first demonstration in the 1950's have been of great interest for fundamental and applied research. They allow to trap charged particles with very low perturbations for extremely long periods of time, thus making possible some ideal realizations for fundamental research. On the other hand, their mass selectivity allowed the development of an important range of applications in particular in the domain of mass spectrometry.

The electric charge of ions allows for a strong interaction with electric and magnetic fields but Laplace's equation (Equation 3.1) forbids the existence of minima for the electrical potential  $\phi$ , thus preventing the trapping of charged particles with static electric fields.

$$\frac{\partial^2 \phi(x, y, z)}{\partial x^2} + \frac{\partial^2 \phi(x, y, z)}{\partial y^2} + \frac{\partial^2 \phi(x, y, z)}{\partial z^2} = 0 \quad (3.1)$$

Two different solutions were proposed by Wolfgang Paul and Hans Dehmelt for which they have been awarded with the Nobel price in 1989. Hans Dehmelt proposed to use both magnetic fields and electric fields [Dehmelt 68]. The presence of a magnetic field in the trap may constitute an important limitation for many atomic physics experiments.

Wolfgang Paul proposed, in the 1950's, to use specially designed time varying electrical fields in order to create a confining effective pseudo potential. The original Paul trap uses hyperbolic shaped electrodes to generate a purely harmonic pseudo

potential thus creating several constraints on the trap design. An important evolution of the Paul Trap is the linear Paul trap, used in this thesis, which has been invented in 1989 [Prestage 89].

In the following we will review the concepts of ion trapping and cooling in the case of linear Paul traps. The reader interested to other traps and to more complicated cases can refer to the abundant literature available, in particular [Ghosh 95].

### 3.1.1 Ion trapping in linear Paul traps

Ions are confined in a linear Paul trap using both static and radio-frequency electric fields. The radio frequency field is designed to trap in two dimensions (X-Y plane), the trapping in the other dimension is ensured by a static electric field (Z axis).

The 2D confinement is ensured by a time varying quadrupolar potential (Equation 3.2) where  $V_{RF}$  is the amplitude of the radio-frequency field,  $V_{DC}$  is the static potential, and  $R$  is the distance between the trap center and the electrode edge. The shape of this potential at  $t = 0$  is represented on Figure 3.1. This potential is usually generated by four cylindrical electrodes (ideally with an hyperbolic section) organized on a square for which the radius of the electrodes is approximately equal to the distance between the trap center and the closest electrode. Such arrangement is visible on Figure 3.3 page 26.

$$\phi(x, y, t) = (V_{RF}\cos(\omega_{RF}t) - V_{DC}) \frac{x^2 - y^2}{R^2} \quad (3.2)$$

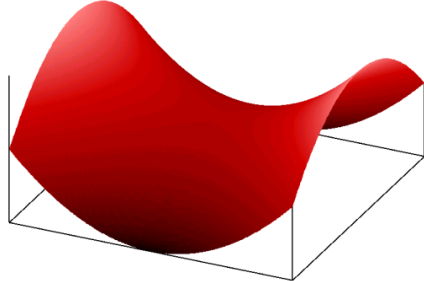


Figure 3.1: Quadrupolar potential created in the Paul trap. This potential can be expressed by Equation 3.2

By carefully choosing  $V_{RF}$ ,  $\omega_{RF}$  and  $V_{DC}$  the particle can have a non diverging (stable) motion in the trap as will be seen in the next paragraph.

**Equations of motion** The trajectory of a particle of mass  $m$  and charge  $Ze$  placed in the potential of Equation 3.2 obeys the following equations of motion :

$$m \frac{\partial^2 x}{\partial t^2} = \frac{Ze(V_{RF}\cos(\omega_{RF}t) - V_{DC})}{r_0^2} x$$

$$m \frac{\partial^2 y}{\partial t^2} = - \frac{Ze(V_{RF}\cos(\omega_{RF}t) - V_{DC})}{r_0^2} y$$

By introducing the following dimensionless parameters :

$$q = \frac{ZeV_{RF}}{mR^2\omega_{RF}^2} \quad a = \frac{ZeV_{DC}}{mR^2\omega_{RF}^2} \quad \tau = \omega_{RF}t \quad (3.3)$$

The equations of motions can be rewritten in the following form :

$$\begin{aligned} \frac{\partial^2 x}{\partial \tau^2} + (a - q\cos(\tau))x &= 0 \\ \frac{\partial^2 y}{\partial \tau^2} - (a - q\cos(\tau))y &= 0 \end{aligned}$$

This is the canonical form of the Mathieu equations, these equations admit non diverging solutions for different ranges of the  $a$  and  $q$  parameters called stability zones. These conditions have been discussed extensively in the literature: [Ghosh 95, Drewsen 00]. There is an infinite number of stability zones, we will consider only the so called first stability region. This stability region corresponds to the simple case where  $a \approx 0$  ( $V_{DC} \approx 0$  V) and  $q \ll 1$ , i.e. the radio frequency field time variation is fast compared to the typical ion motion. This region is schematically represented on Figure 3.2.

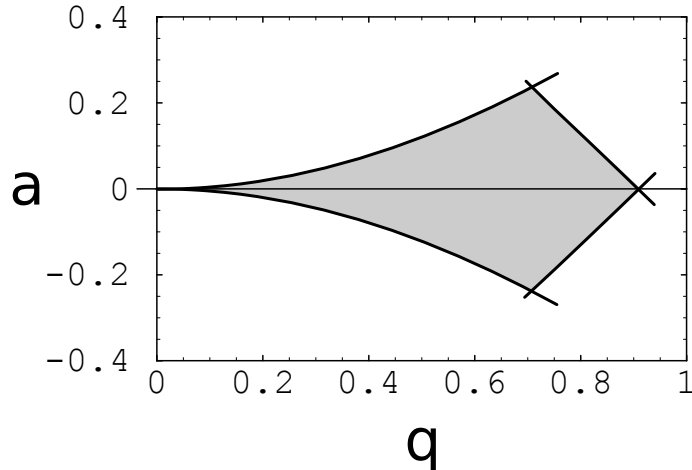


Figure 3.2: First Stability zone, in grey the zones for which the Mathieu equations admit stable solutions.

$a$  and  $q$  are defined in Equation 3.3.

**Low order solutions** The Mathieu equations do not exhibit analytical solutions for the general case, but they can be solved under some approximations. In the following, only the lowest order solutions for the first stability zone will be discussed. Higher order solutions give corrections that are out of the scope of this introduction.

For  $|a| \ll 1$ ,  $|q| \ll 1$  the Mathieu equations admit solutions of the following form:

$$u(t) = u_0 [1 - q\cos(\omega_{RF}t)] \cos(\omega_r t)$$

Where  $\omega_r = \omega_{RF}\sqrt{\frac{q^2}{2} - a}$

(3.4)

Since  $|a| \ll 1$ ,  $|q| \ll 1$ , we have  $\omega_r \ll \omega_{RF}$ . So the ion motion consists in a high amplitude oscillation at low frequency called the secular motion, surimposed to a fast, low amplitude oscillation called micromotion.

By averaging in time the fast motion, the motion of the ion is similar to the motion of a charged particle in an harmonic potential called pseudo-potential which can be expressed the following way:

$$\Phi(r) = \frac{1}{2}m\omega_r^2 r^2$$

In the case  $a = 0$

$$\omega_r = \omega_{RF} \frac{q}{\sqrt{2}} = \frac{ZeV_{RF}}{\sqrt{2mR^2\omega_{RF}}}$$

$$\Phi(r) = \frac{(ZeV_{DC})^2}{4mR^4\omega_{RF}^2} r^2$$

We can notice a dependence of the trapping pseudo potential on the mass of the particle. This dependence is an interesting feature and will be discussed in more detail in chapter 5

**Axial confinement** The axial confinement is ensured by applying a DC voltage to a set of electrodes (usually called endcaps) creating an harmonic potential along the z axis giving the following final potential :

$$\Phi(r, z) = \frac{1}{2}m(\omega_r^2 r^2 + \omega_z^2 z^2)$$

The subsequent radial deconfinement due to the Laplace equation can be taken into account by an effective  $a_z$  which is usually small [Drewsen 00].

**Micro motion amplitude** The micromotion is the source of the so-called Radio Frequency heating. This heating is due to the energy transfer from the trapping field to an ion cloud by the collisions between the ions thus is absent when a single ion is trapped. From Equation 3.4 and with the initial conditions, we can see that the amplitude of the micromotion is independent of the position on the z axis and is proportional to the distance from the trap center. We see here one of the advantages of the Linear Paul Trap : we can trap several ions on the trap axis without micromotion. We notice also that the micromotion amplitude is proportional to the  $q$  stability parameter giving rise to a strong dependency between radio frequency heating and this parameter [Prestage 91].

### 3.1.2 Ion clouds at low temperature

It is possible to trap large numbers of charged particles in a linear Paul trap. When the temperature of the ion cloud is sufficiently low, the ion cloud can be described as a liquid and even as a crystal. The presence of this arrangement is of particular interest for single ion addressing in the context of quantum simulations and quantum information.

**Coulomb crystals and plasma coupling parameter** An ion cloud at low temperature can be studied using the theoretical background of plasma physics. In particular an ion cloud is (generally) a one component plasma. The thermodynamic properties of a one component plasma are fully characterized by a dimensionless parameter  $\Gamma_P$  [Ichimaru 82].

This parameter is the ratio between the mean interaction energy and the thermal energy and can be expressed as follows:

$$\Gamma_P = \frac{(Ze)^2}{4\pi\epsilon_0 a_{ws} k_B T}$$

where  $Z$  is the charge of the ions (usually +1) and  $a_{ws}$  is the Wigner Seitz radius which can be linked to the density  $\rho_0$  :

$$\frac{4}{3}\pi a_{ws}^3 = \frac{1}{\rho_0}$$

In ion clouds a clear phase transition occurs between the gas and the liquid state and the transition between the liquid to the crystalline state is continuous [Blümel 88]. The ion cloud is in a gas phase for  $\Gamma_P < 2$ . The crystallization is considered to be reached for  $\Gamma_P > 170$  in the case of infinite clouds : [Slattery 80] and for higher values of  $\Gamma_P$  in the case of finite clouds. These limits allow for an estimate of the ion cloud temperature given an estimate of the ion density and high resolution imaging of the ion cloud.

**Crystal density** The crystalline state has some interesting properties in particular concerning the density. Considering a crystal at zero temperature. The crystal is at the thermodynamic equilibrium (neglecting edge effect), noting the total potential  $\phi_{tot}$  this gives:

$$\phi_{tot}(r, z) = cst$$

$$\nabla^2 \phi_{tot}(r, z) = 0$$

$$\nabla^2 \frac{\phi_{trap}(r, z)}{Ze} + \nabla^2 \phi_{charge}(r, z) = 0$$

The potential created by the ions  $\phi_{charge}(r, z)$  can be computed using the Poisson's equation :

$$\nabla^2 \phi_{charge}(r, z) = -\frac{Ze\rho_0}{\epsilon_0}$$

Which allows to obtain:

$$\rho_0 = \frac{\epsilon_0 V_{RF}^2}{mr_0^4 \omega_{RF}^2}$$

Where  $m$  is the ion mass,  $r_0$  the distance between the trap center and the electrodes. The density inside the ion crystal is constant and only depends on the mass and the trapping parameters. This important result is valid only for harmonic potentials. The density at the edge of the crystal depends on the temperature and can be characterized by a characteristic length : the Debye length [Dubin 99]. This length is expressed as follows :

$$\lambda_D = \sqrt{\frac{k_B T \epsilon_0}{e^2 \rho_0}}$$

This length can be expressed with the Wigner Sietz radius and the coupling parameter

$$\lambda_D = \frac{a_{ws}}{\sqrt{3\Gamma_P}}$$

For an ion crystal, this length is about 20 times smaller than the Wigner Seitz radius showing that the edge effects can be neglected, and a crystal can be considered as a uniform density medium.

### 3.1.3 Ion cooling

The principles of laser cooling of neutral atoms applies to trapped ions. However, due to the strong confinement from the trap, the coulomb interaction between ions and the radio frequency heating displays some particularities of ion cooling.

The tight confinement offers, for some trap configurations, the possibility of advanced cooling by addressing transitions between quantized vibrational levels. This technique named “resolved sideband cooling” allows for the cooling to the ground vibrational state [Neuhauser 78, Eschner 03]. Singly ionized alkaline earth ions possess a  $\Lambda$  level structure, allowing for the use of electromagnetically induced transparency (EIT) cooling [Morigi 00]. This technique uses the change in the excitation probability spectrum induced by EIT for a more efficient cooling.

As described previously, contrary to neutral atoms, ions trapped in radio frequency trap can experience significant heating due to the time dependent trapping potential. The presence of this heating source changes the optimal parameters for laser cooling. In systems where external heating is negligible, the lowest temperature is reached for low cooling intensity and detuning equal to  $-\Gamma/2$  where  $\Gamma$  is the natural linewidth of the excited state [Stenholm 86]. Due to the presence of heating we need to maintain a significant scattering rate, thus increasing the intensity. At

high intensities, the scattering rate is important but its dependence on the detuning becomes low due to the line broadening, making the process inefficient. In this case, the detuning needs also to be increased to operate on the edge of the broaden line. A compromise has to be found between the high scattering rate and the cooling efficiency.

In a trap containing several ions, thanks to the Coulomb interaction which couples the different degrees of freedom, the ion motion can be cooled in the three spatial directions with only one laser beam. In the single ion case the same is true if the beam has projections along the three axes of the trap.

Ionic systems, thanks to the strong coulomb interaction, offer the possibility of efficient sympathetic cooling. By trapping different species or isotopes in the trap, it can be possible to laser-cool only one of the species without perturbing the internal states of the others. The heat being exchanged by coulomb interaction, this technique allows for the cooling of the whole sample. This technique is of particular interest when direct laser cooling is difficult, for example in molecular ions spectroscopy, cold chemistry, mass spectroscopy, molecular ion cooling etc. or when the heating sources are too important, for example in micro-traps [Deslauriers 06, Dubessy 09].

This technique has proven its effectiveness in several experiments. Ion strings containing about 10 ions can be cooled to less than 10 mK using just one ion as a coolant [Bowe 99]. This approach has been improved for quantum information purposes where ions are shuttled in pair. One laser cooled ion (refrigerant) keeping the qubit ion cooled without affecting the quantum superposition in the internal states [Kielpinski 02, Home 09, Barrett 03, Jost 09]. This technique also allows for the cooling of heavy and complex molecules to  $\approx 0.1$  K [Ostendorf 06] opening the way to high precision spectroscopy of proteins and other complex organic molecules.

**Cooling of  $\text{Sr}^+$**  The level structure of Strontium is detailed in Figure 3.10. We use the  $5S_{1/2} \rightarrow 5P_{1/2}$  transition as the main cooling transition. Given the natural linewidth of this transition  $\Gamma = 2\pi \times 20$  MHz we obtain a Doppler temperature  $T_D = \frac{\hbar\Gamma}{2k_B}$  of  $\approx 0.5$  mK. For a density of  $2 \times 10^{14}$  ions/m<sup>3</sup>, the crystallization temperature is  $\approx 10$  mK and for a sample cooled down to the Doppler temperature we obtain a crystallization parameter  $\Gamma_P \approx 3000$  showing that ions can be crystallized using only Doppler cooling.

To avoid accumulation of the ions in the metastable  $4D_{3/2}$  level, we address the  $4D_{3/2} \rightarrow 5P_{1/2}$  transition with a repumping laser. This  $J \rightarrow J - 1$  transition possesses a single field dark state for all polarizations of the repumping laser. This dark state can be destabilized by modulating the polarization of the repumping laser or by applying a magnetic field [Berkeland 02]. As will be described in the section 3.10, we use this dark state to find the zero of the magnetic field and apply a directing field to destabilize it.

## 3.2 Trap

The trap which has been used during this thesis is a linear Paul trap designed for trapping high volume, high density coulomb crystals. The main dimensions of the trap can be found on Figure 3.3. This trap has been designed to be very symmetric to reduce the need of electric field compensation [Removille 09b].

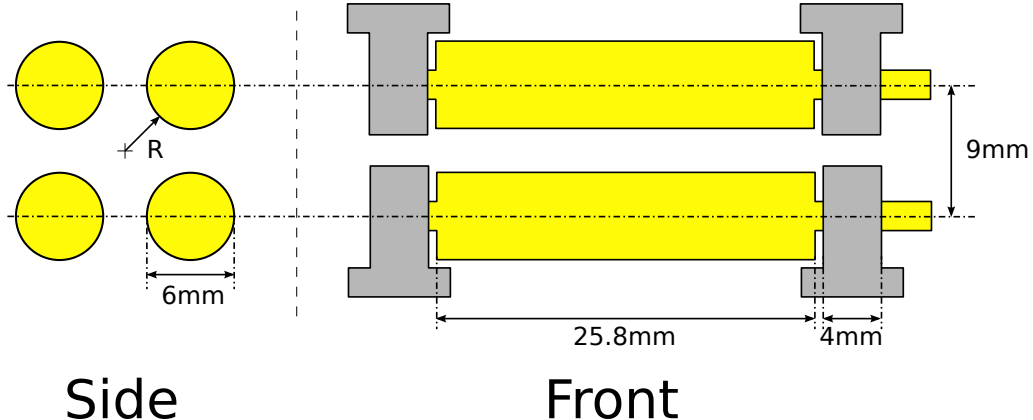


Figure 3.3: Trap dimensions and design. The yellow bar are the RF electrodes, the grey pieces are the endcaps.

Here  $R = 3.36 \text{ mm}$

For better shielding, the trap is held between two horizontal metallic ground plates (not represented)

## 3.3 Radio-frequency source

Reaching high densities in a high volume trap while keeping the radio frequency heating low poses several constraints on the design of the radio frequency source. In particular it is important to operate at a low  $q$  trapping parameter [Prestage 91] thus requiring high voltages at high frequencies and having the possibility to add DC voltages to the trapping electrodes for the micromotion compensation.

### 3.3.1 Resonator

As stated previously, to obtain a large light matter interaction in ion ensembles one of the key parameter is the ion density. Keeping the  $q$  parameter low for low radio frequency heating brings constraints on the choice of the radio frequency voltages and frequencies.

The density in an ion crystal and the  $q$  parameter can be expressed as follows (see section 3.1)

$$n = \epsilon_0 \left( \frac{V_{RF}^2}{mR^4\omega_{RF}^2} + m\omega_z^2 \right)$$

$$q = \frac{ZeV_{RF}}{mR^2\omega_{RF}^2}$$

For a fixed geometry, to increase the density one can increase the radio-frequency voltage  $V_{RF}$  or decrease  $\omega_{RF}$ . Since  $q$  has to be maintained low high  $V_{RF}$  and high  $\omega_{RF}$  are needed.

Since the Paul trap and its connections can be seen electronically as almost pure capacitors, resonant LC circuits are often used to generate high voltages at high frequency by stepping up a standard radiofrequency source. To obtain these voltages, we use a double output resonator made of two air spaced coils wounded as a tore with alternating turns. This allows for a good cross inductance and results in the same resonance frequency for the two outputs and opposite phases allowing to double the effective  $V_{RF}$  with respect to a single resonator. Each secondary output consists in a 22 turns torus coil made with a copper wire of 1.7 mm in diameter. The internal torus diameter is 32 mm and the torus diameter is 15 cm.

The resonance frequency is about 7.5 MHz and the measured step-up gain is 20. This resonator allows for a 50 V amplitude input signal to obtain two signals with amplitude 1000 V making differential RF amplitude of 2000 V corresponding to  $V_{RF} = 1000$  V,  $q = 0.04$  and  $\rho_{expected} \approx 2 \times 10^{14}$  ions /m<sup>3</sup>.

The resonator input signal is generated with a commercial RF amplifier (ar® model KMA1020) which a gain of 50 dB and an output power of more than 25 W @ 10 MHz.

In order to protect the RF amplifier, it is important to match the output impedance of the amplifier to the resonator. In our case, the amplifier tolerates an impedance mismatch of 3:1.

By measuring, for different frequencies, the relative amplitudes and phase of the signals across a divider bridge made with a 50Ω resistor and the couple resonator + trap, the complex impedance of the couple resonator + trap can be measured.

The result of this measurement is depicted on Figure 3.4. From this measurement, the values of the components needed to build an impedance adaptation circuit like the one depicted on Figure 3.5 can be computed using standard simulation tools such as <http://designtools.analog.com/RFIMPD/>.

The addition of this circuit, have shifted the resonance frequency by 10% (6.8 MHz to 7.6 MHz) and the impedance at resonance is now  $Z \approx 60\Omega + i.10\Omega$ , giving an impedance mismatch significantly lower than 3:1 needed for the safe operation of the amplifier.

In order to have access to the resonator output voltage without perturbing its behavior, a single turn coil has been placed near the output wire of the resonator and calibrated. This probe coil allow to measure the output voltage over the full accessible range. The result of this measurement versus the input RF power is depicted on Figure 3.6.

The resonator with the impedance adaptation circuit, allow to reach high voltages at high frequencies, allowing an important confinement while keeping the  $q$

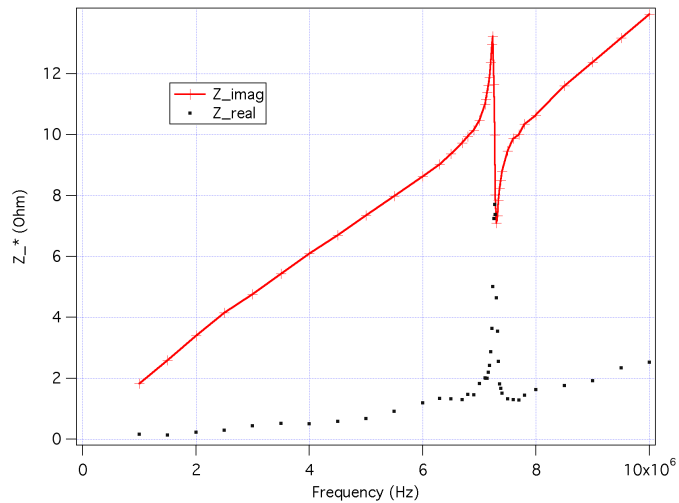


Figure 3.4: Impedance of the resonator without the impedance matching. See main text for details.

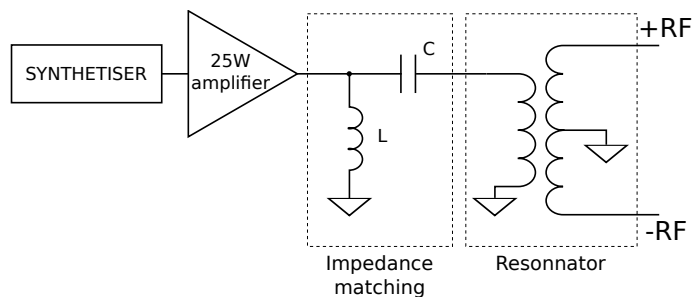


Figure 3.5: Circuit for impedance matching between the amplifier and the resonator. Good impedance matching is obtained for  $C = 600 \text{ pF}$  and  $L = 680 \text{ nH}$

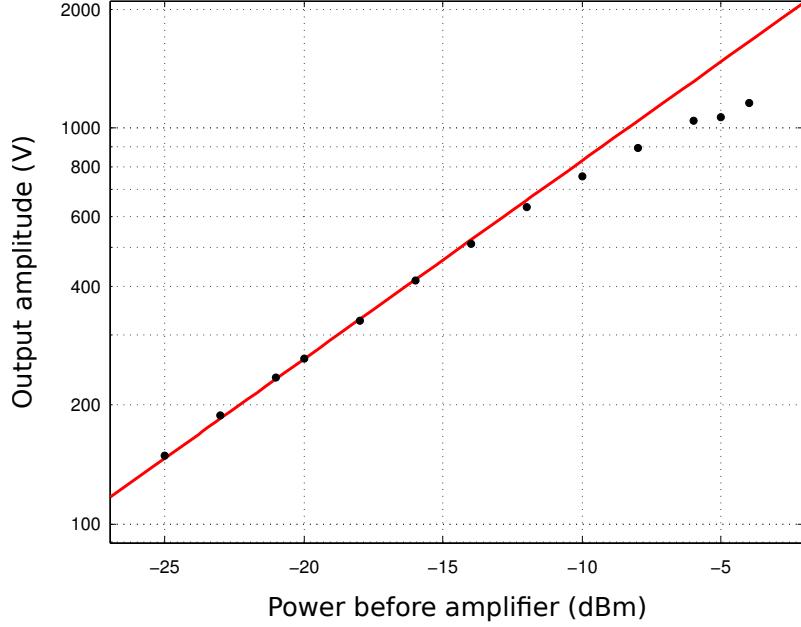


Figure 3.6: RF amplitude on each electrode versus RF power before the RF amplifier. The non linear behavior on the top right corner of the graph is due to the saturation of the amplifier.

The red continuous line is a theoretical fit giving  $V_{RF} = 68.36\sqrt{10^{P_{dBm}/10}}$

parameter low.

### 3.3.2 Micro motion compensation

To reduce the amount of micro motion, the ions must be trapped where at the radio frequency field node. The static electric fields must be compensated at the node of the radio frequency field to allow the trap potential minimum to overlap with the RF node.

Stray electric field may arise from geometrical imperfections, the ion pump, deposited charges on insulating surfaces, etc... To cancel stray fields two methods are widely used. The first one uses supplementary external electrodes. The other method, used in our trap, consists in adding DC offset to the main RF electrodes. The circuits used for this purpose are depicted Figure 3.7 and Figure 3.8.

The tuning of the compensation voltages can be achieved in different ways. The most used technique is based on the measurement of the micro-motion amplitude by single photon correlations [Berkeland 98]. Because the cooling laser is detuned from the transition, variations in speed, have a signature in the absorption probability inducing a correlation between the fluorescence and the radiofrequency field proportional to the micro motion amplitude. This technique is efficient for single ion traps. In the case of coulomb crystals we can use observation of the crystal shape and the isotopes arrangement (see section 5.2 page 54) to adjust the compensation

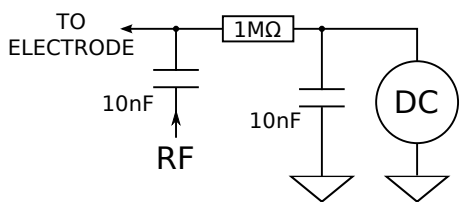


Figure 3.7: Circuit for mixing the RF and the DC voltage. This circuit is present on each RF electrode.

This circuit can be considered as a Bias tee adapted to the high voltage radio frequency. This circuit is placed between the vacuum feedthrough and the resonator box.

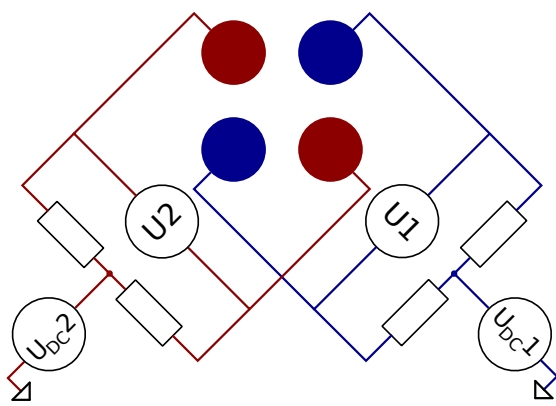


Figure 3.8: Connection of the four DC voltages to each RF electrode. The bias tee circuit is not represented on this figure.

Bars with the same colors are connected to the same RF phase (see the subsection 3.3.1)

This connection is made to decouple the compensation degrees of freedom with respect to the  $U_{DC}$  voltages which affect the  $a$  trapping parameter.

voltages that are, in any case, less crucial than in the ion string case.

In the presence of stray fields, the trap center depends on trap stiffness and therefore on the radio-frequency amplitude. The compensation voltages ( $U_1$  and  $U_2$  on Figure 3.8) can be adjusted by imaging an ion cloud and changing the amplitude of the radio frequency field. The voltages are adjusted in order to reduce the position change of the ion cloud as a consequence of this change. The precision obtained is on the order  $50 \text{ V m}^{-1}$  (which corresponds to a displacement of  $30 \mu\text{m}$  at high RF amplitude).

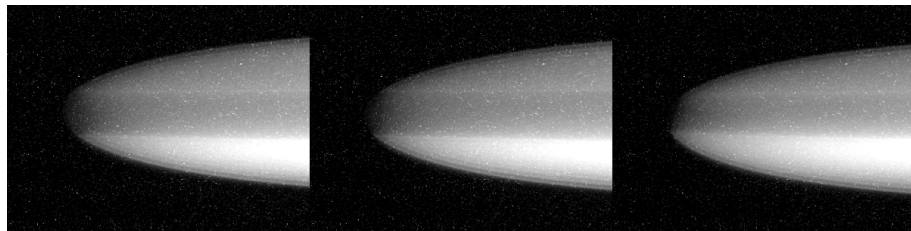


Figure 3.9: Image of the edge of a natural  $\text{Sr}^+$  ion cloud for different compensation voltages. The variation of the relative position between the isotopes is clearly visible.

The presence of multiple isotopes in the trap can also be used for compensating stray fields. The trap stiffness is inversely proportional to the mass, which implies,

for multiple isotopes cloud, a trapping center different for each isotope when stray fields are present. This differences make the ion cloud asymmetric as can be seen on Figure 3.9. This technique is used in parallel with the previous one.

### 3.4 Laser system

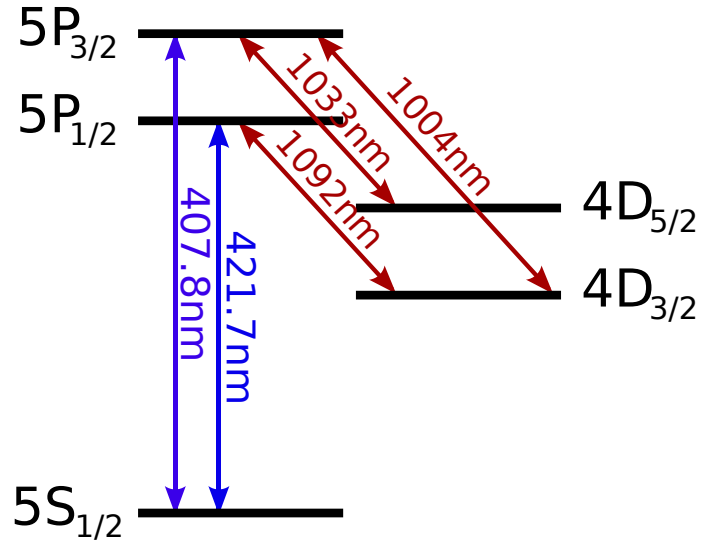


Figure 3.10: Low energy levels of  $\text{Sr}^+$  and the associated dipole allowed transitions. The lifetimes are presented section D.1.

Trapped  $\text{Sr}^+$  ions are Doppler cooled using the 711 THz  ${}^5\text{S}_{1/2} \rightarrow {}^5\text{P}_{1/2}$  transition (Figure 3.10). This transition is driven using laser light generated by a commercial single mode Ti:Sa CW laser (Coherent®MBR-110) frequency-doubled in a single pass geometry. Up to 20 mW are available after the doubling process and the coupling into a single mode, polarization maintaining fiber. Thanks to a near-coincidence with the  ${}^5\text{S}_{1/2} F=2 \rightarrow {}^6\text{P}_{1/2} F'=3$  transition of  ${}^{85}\text{Rb}$  [Madej 98, Sinclair 01] the laser frequency is locked to an atomic reference.

In order to avoid the accumulation of the ions into the metastable  ${}^4\text{D}_{3/2}$  state during the cooling process, a “repumping” laser drives the  ${}^4\text{D}_{3/2} \rightarrow {}^5\text{P}_{1/2}$  transition. The repumping laser is a commercial fiber laser (Koheras Adjustik Y10) with a nominal linewidth of 70 kHz and it is stabilized by a transfer lock technique using a ring cavity and a single mode diode GaN laser (Toptica DL100) locked onto an Rubidium atomic reference.

The different sources and their feedback are schematically represented in Figure 3.11

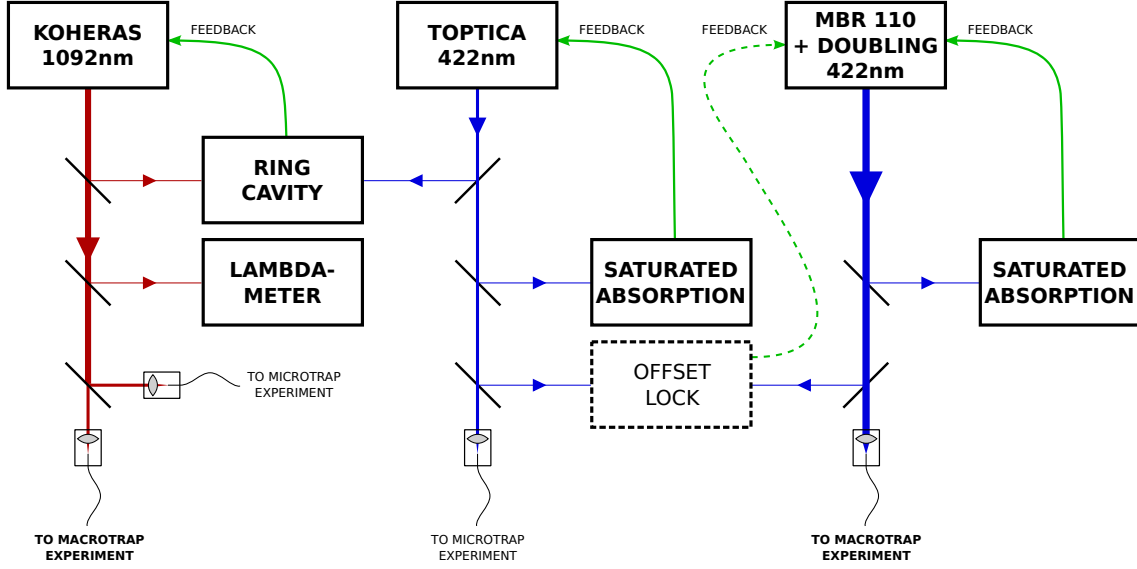


Figure 3.11: Overview of the laser system and feedback

The Toptica DL100 diode is locked onto a Rubidium atomic reference. This laser is then used to lock the ring cavity to which the infrared repumping laser is locked. The MBR cooling laser is either locked on it's atomic reference or, on the Toptica DL100 diode using an offset lock.

### 3.5 Violet laser source

The light needed for ion cooling and manipulation of the 422 nm transition is provided by a frequency-doubled commercial Ti:Sa laser. In the following section, the optical set-up and the stabilization system will be presented.

The optical set-up is schematically represented in Figure 3.12. A Coherent Verdi V-18 delivers pump beam of 18 W @ 532 nm. This beam pumps the MBR-110 Ti:Sa laser which delivers a 3W, single mode beam at 844 nm. The power sent to the crystal is controlled by a couple half-waveplate, polarizing beam splitter. For the alignment of the pump polarization with the crystal axis, a zero order half-waveplate is placed before the doubling crystal. The beam is then focused into a Periodically Poled Potassium Titanyl Phosphate crystal (Raicol) of  $1 \times 2 \times 30$  mm<sup>3</sup>. This crystal is optimized for second harmonic generation of light @ 842 nm and anti reflection coated both at 842 nm and 421 nm.

The doubling efficiency of periodically poled crystal is very sensitive to the temperature (the doubling efficiency is divided by two when the temperature is away of 0.25 K from the optimal temperature). The crystal is maintained to its optimal temperature (64.5 °C) by using an oven from Raicol crystals which has a long term stability of  $\pm 0.05$  °C. The typical output is in the order of 80 mW of violet light for 1.8 W of pump.

Residual polarization fluctuation (less than 1% of rotation) have been noticed after the crystal. In order to ensure proper operation of the polarization maintaining

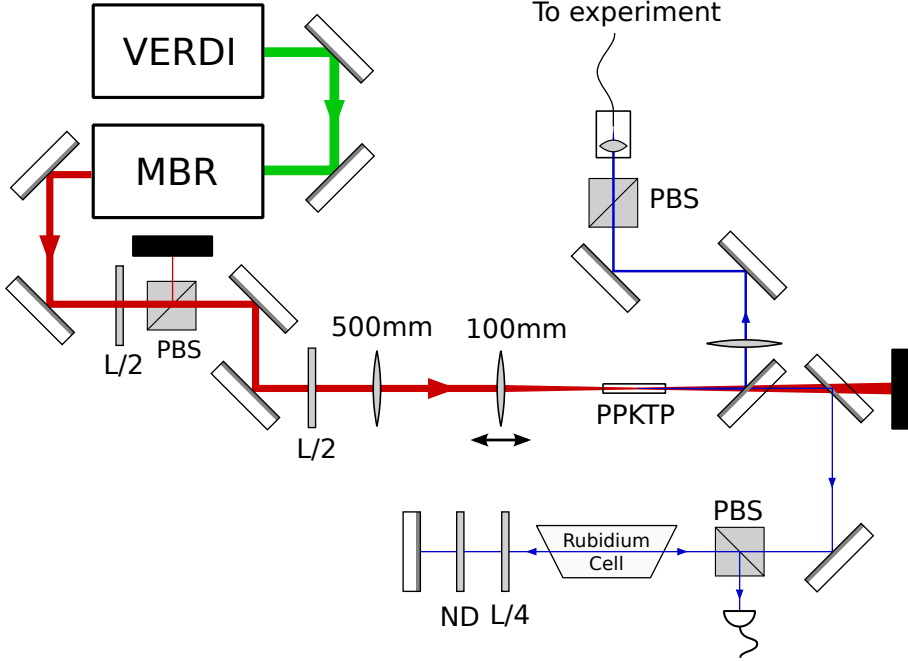


Figure 3.12: Optical set up for the generation and the stabilization of the 422 nm laser source.

fiber, a PBS is placed in front of the input coupler to clean the polarization. This PBS is held in a rotating mount for fine adjustment of the polarization axis to the fast axis of the fiber.

### 3.5.1 Frequency stabilization

Thanks to a quasi coincidence between the  ${}^5\text{S}_{1/2} \rightarrow {}^5\text{P}_{1/2}$  transition of  ${}^{88}\text{Sr}^+$  and the  ${}^5\text{S}_{1/2} (\text{F}=2) \rightarrow {}^6\text{P}_{1/2} (\text{F}'=3)$  transition of  ${}^{85}\text{Rb}$  [Madej 98] the cooling laser can be stabilized using an atomic reference. In order to do that, a rubidium saturated absorption spectroscopy set-up [Schawlow 82] is used. The cell is 3 cm long and contains isotopically pure  ${}^{85}\text{Rb}$ . In order to increase the atomic density, it is maintained at a temperature of 120 °C. In these conditions, we obtain a probe absorption of 80% with narrow features with 10% contrast.

In order to get an error signal from the absorption peaks the dither lock method is used. The first derivative of the absorption signal is obtained with a lock-in amplifier that demodulates a frequency-modulation (amplitude  $\approx 5$  MHz) imposed to the laser. The main difference with the common Pound Drever Hall technique [Drever 83] is the lower bandwidth. The MBR-110 is already modulated at 89.2 kHz for the lock of the cavity thin etalon that ensures single mode operation of the laser. The reference signal is taken on the motherboard of the laser controller and injected into the reference input of the lock-in amplifier (FEMTO LIA-MV-200-H). Since the internal modulation modulates the intensity of the laser by a few percent, an offset is

present on the demodulated signal. This offset is minimized by adjusting the phase of the lock in amplifier and then canceled electronically. This offset does not vary significantly thus does not constitute a source of instability. The offset-subtracted demodulated signal is sent to the frequency scan input of the laser via an analog PID filter.

The laser usually remains locked for about half a day. This is mainly limited by the temperature drifts of the cavity which bring the feedback out of range. At the end of this thesis, this lock has been replaced by an offset lock which is detailed on Appendix C page 127.

### 3.5.2 Intensity fluctuations

Whereas the output intensity of the MBR-110 is quite stable ( 2% fluctuations on a timescale of a few minutes) the doubled 422 nm laser beam exhibit relatively large intensity fluctuations : 10% to 20% on a timescale of a few minutes. The origin of these fluctuations is still unclear, issues in the temperature regulation of the crystal being a probable cause. The sensitivity of the oven temperature probe does not allow to see correlation between the measured temperature and the laser intensity. Pointing instability have been excluded since the signal after the fiber does not exhibit significantly larger fluctuations. Work is in progress to set up a noise eater to eliminate these fluctuations.

## 3.6 Infrared lock implementation

### 3.6.1 Locking method

The frequency of the  $4D_{3/2} \rightarrow 5P_{1/2}$  transition for  $^{88}\text{Sr}^+$  is 274 589.4 GHz. There is no strong atomic coincidence or quasi coincidence at this energy. In the absence of atomic reference, the laser can be locked to hollow cathode lamps, ultra stable cavities or standard cavities via transfer lock. The later strategy has been set up taking advantage of the already stabilized 422 nm sources.

The transfer lock cavity is a 3-mirrors, 1 m long ring cavity made from one piezo controlled spherical mirror ( $f = 1\text{ m}$ ) placed at the back of the cavity and two flat mirrors at the entrance ports. All the mirrors are coated for maximizing the reflection at 422 nm and 1092 nm. The cavity has a finesse of  $\approx 100$  both in the violet and the infrared. The two lasers are counter propagating in the ring cavity, the signals from the two lasers are measured independently via the reflexion from the entrance mirrors as depicted on Figure 3.13.

A typical signal obtained while spanning the cavity back mirror is depicted on Figure 3.14. One can see the main resonances and the smaller peaks corresponding to the higher order spatial modes.

The repumper laser lock needs to compensate for slow frequency drifts of the order of 100 kHz/s. To obtain a good flexibility on the set point we implemented the transfer lock by continuously scanning the cavity and measuring the relative

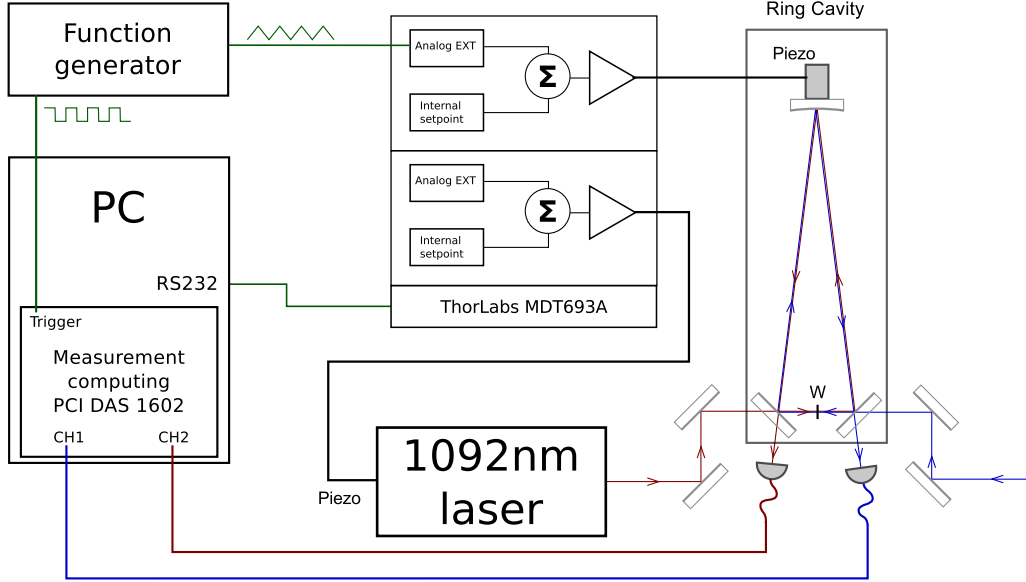


Figure 3.13: IR locking scheme. Transfer lock from the violet laser diode locked onto an atomic reference to the Infrared laser.

positions of the resonance peaks [Seymour-Smith 10, Burke 05]. This method allows for a large capture range and a total flexibility for moving the laser setpoint while keeping its frequency locked. The detailed scheme is depicted on figure 3.13

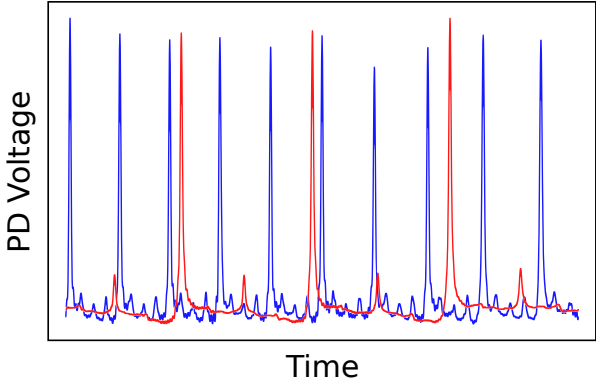


Figure 3.14: Typical traces at the output of the cavity when the lasers are locked and the cavity is spanning. In red the signal from the 1092 nm laser, in blue the signal from the 422 nm laser. The minor peaks corresponds to higher order spatial modes.

A program has been developed for the traces analysis and feedback computation.<sup>1</sup> The program continuously records the traces from the cavity. After a moving average on the traces, it detects all the peaks. From the peak positions it computes the mean time between the violet reference peaks to convert the horizontal unit of the traces from time into fraction of free spectral range allowing to take into account changes in the piezo response. It corrects the cavity drift by measuring the distance between the center of the trace and the closest violet peak. The feedback gain is chosen to

<sup>1</sup>available at <http://github.org/braice/laser-lock>

have the best correction in one step. The infrared laser frequency is corrected by measuring the distance between the violet peak closest to the center and the infrared peak closest to the set-point. When the user requests a change in the frequency of the infrared laser, the laser is moved close to a calculated position (using the calibrated piezo gain of the laser) and the set-point is adjusted, taking into account the folding induced by the cavity FSR. Generally, the laser is able to reach the target position (within 1 MHz) in two steps.

This lock is a pure integral lock with the gain adjusted in order to have the right correction in one iteration. The lock bandwidth is  $\approx 3$  Hz, currently limited by the non linearities of the cavity piezo which would even become larger at higher frequencies. Since the feedback is relatively slow compared to the response time of all the elements in the loop, there are no stability concerns.

### 3.6.2 Calibration and performances

In order to get a good precision on the relative laser frequency after a change in the setpoint, the cavity free spectral range has to be known accurately. To measure it, the cavity has been locked to the violet laser, and the position of the infrared peaks monitored. The frequency of the infrared laser was measured with a lambdameter (Burleigh WA-1100) with a precision of a few 100 MHz while the temperature of the infrared laser is progressively scanned (2 hours from 20 °C to 50 °C). After a full frequency scan we counted the number of FSR the laser has gone through ( $N = 489$ ) and the frequency change ( $\Delta f = 112.08$  GHz), which gives a FSR of 229.2 MHz  $\pm 0.41$  MHz

To evaluate the quality of the lock, the histogram of the nominal frequency of the infrared laser (as measured with the transfer-lock cavity) has been acquired during several hours. The result of this measurement is depicted on Figure 3.15 giving an effective linewidth of 600 kHz.

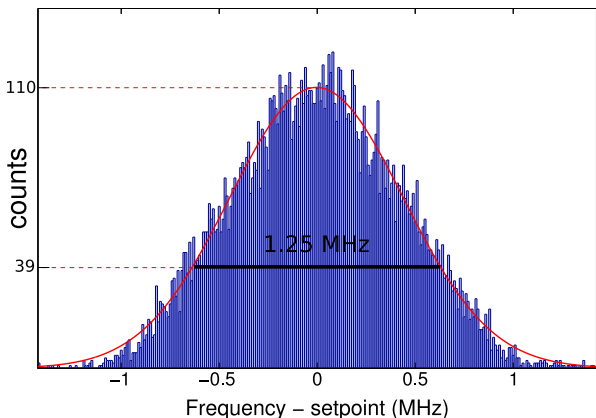


Figure 3.15: Histogram of the error signal on the infrared laser. This error signal is the time difference between the reference cavity peak and the infrared peak closest to the set-point. The error signal is converted in MHz, knowing the time difference between two infrared peaks and the cavity Free Spectral Range.

### 3.6.3 Limitations and possible improvements

This lock is mainly limited by two factors: the non linearity of the cavity piezo response, and its bandwidth. The first problem limits the precision, the error is estimated to be about 1% across the FSR. This situation can be improved by using violet laser peaks as a ruler to estimate the non linearity in real time. The bandwidth is mainly limited by the mass of the back mirror. Scanning this heavy mirror faster increases the non linearity of the scanning (because it becomes sinusoidal). A factor of 10 can be obtained by replacing this mirror by a smaller one. Then the lock would be limited by the acquisition card sampling rate which is currently of  $250 \times 10^3 \text{ s}^{-1}$ . In this case a faster data analysis could be implemented [Seymour-Smith 10].

## 3.7 Frequency and polarization control

As stated previously, natural strontium contains several stable isotopes. The isotope shifts are sufficiently large for independent laser addressing and, for even isotopes, sufficiently close to be addressed using standard accousto optic modulators. A more detailed description of these shifts and their measurement is given in chapter 6. A cooling and a repumping laser beams have been set up for each of the A=88 and A=86 isotopes as described below.

The frequency of the four beams is fine tuned using accousto optic modulators. The polarization of the violet beam addressing the A=86 isotope is controlled via an electro optic phase modulator. An overview of the optical set-up is presented on Figure 3.16.

### 3.7.1 Probe beam control

The A=86 isotope occupies the center of a natural Sr<sup>+</sup> ion crystal (see chapter 4). For this reason, this isotope has been chosen to be the work isotope since its overlap with a focused Gaussian laser beam is optimized. The beam addressing this isotope is used as a cooling, pumping and probe beam. For this reason frequency, intensity and polarization of this laser beam can be adjusted quickly and independently.

**Spatial control** To ensure a maximum interaction between light and the atomic ensemble, the laser beam profile needs to be matched with that of the atomic ensemble. For large multi isotope ion clouds, the atomic sample has a cylindrical shape with a length between 5 mm and 20 mm and a diameter between 50 μm and 1 mm. As soon as the beam is fully contained in the atomic sample the optical depth of the sample does not depend on the diameter. Reducing the size of the probe beam is important for maximizing the interaction for a given number of ions.

As shown on Figure 3.16, the probe beam is focused onto a 100 μm pinhole with a f=30 mm lens and imaged on the ion cloud with a bi-convex, 2", f=500 mm lens in a 2f-2f configuration. This configuration allows for a diffraction limited imaging of the pinhole and spatial mode cleaning.

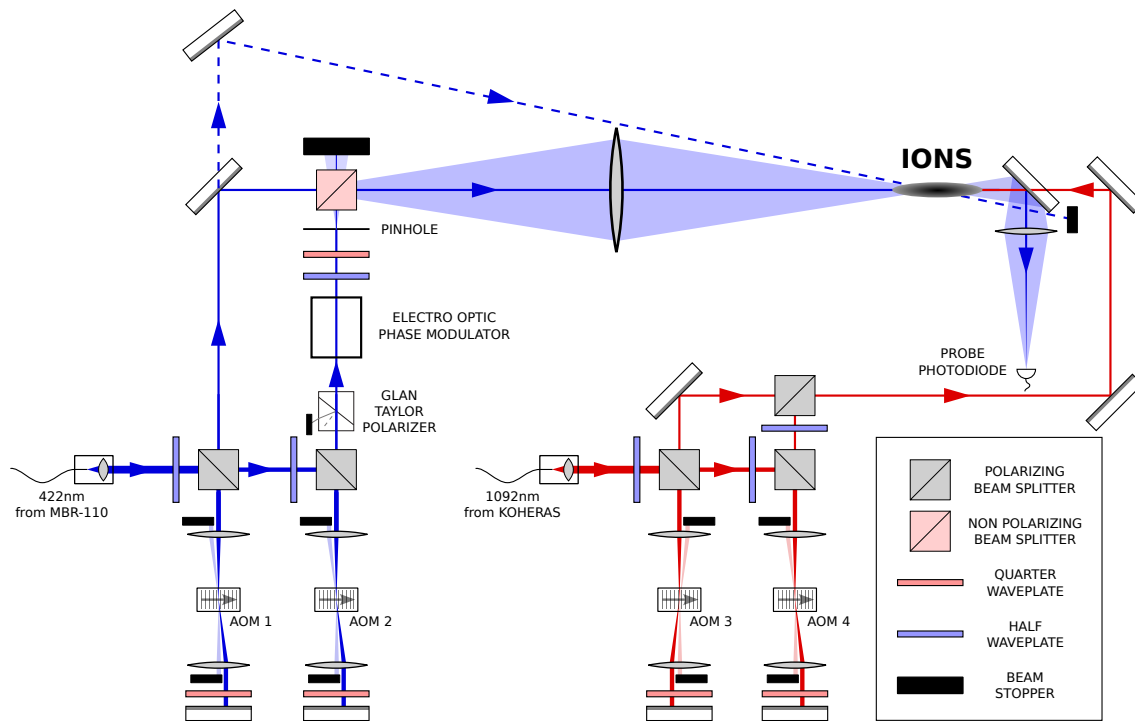


Figure 3.16: Frequency and polarization control of the laser sources.

This set-up allows us to address independently and simultaneously the couples  $A=88,86$  or  $A=86,84$ . The frequency and intensity controlled is ensured by the use of accousto optic modulators. The polarization of the violet beam addressing the  $A=86$  isotope is controlled using a electro optic phase modulator.

In order to check the quality of the final beam, it has been imaged onto a linear Prosilica GC660 CCD camera. A 2D Gaussian fit of the measured intensity gives a beam intensity waist of  $27\text{ }\mu\text{m}$  which corresponds to 90% of the intensity contained in a circle of  $113\text{ }\mu\text{m}$  diameter, in good agreement with the expectations. The Rayleigh length associated to this waist is 5 mm corresponding to the typical half length of the ion cloud.

After the ion trap, the beam is re-imaged with a similar 2f-2f configuration onto the probe photodiode.

**Intensity and frequency control** To simplify the optical set-up, the same beam is used for cooling, preparing and probing the  $A=86$  isotope. The frequency and the intensity changes have to be fast enough in order to properly switch between the different uses of the beam. This switching is achieved by controlling the radio frequency sent to the acousto optic modulator. The radio frequency set-up controlling the signal sent into the probe AOM is sketched on Figure 3.17. This set up is based on standard radio frequency components from Mini-Circuits®(VCO: POS-150, Switch: ZYSWA-2-50DR, Attenuator: ZX73-2500), and allows us to select in 50 ns between two frequencies and two powers. This set-up is mainly used in the experiments described in chapter 7.

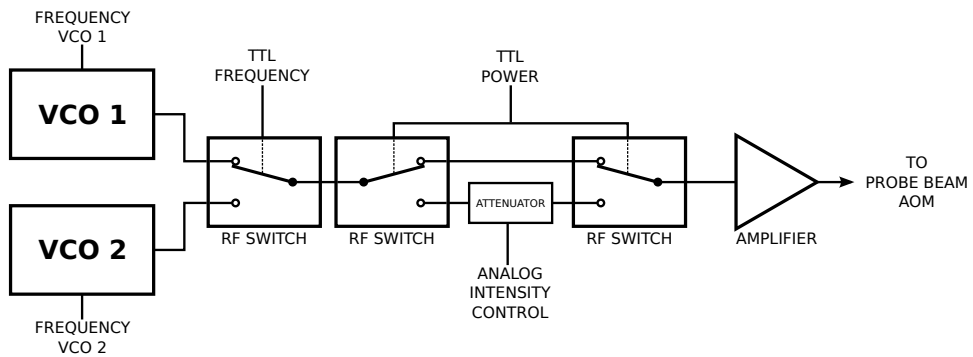


Figure 3.17: Set up for the control of the radio frequency for the probe AOM. This set up allows for a fast switching between two frequencies and two attenuations

**Polarization control** In order to control the populations in the various Zeeman sublevels in the  $5S_{1/2}$  state (Figure 3.18) the polarization of the beam addressing the  $5S_{1/2} \rightarrow 5P_{1/2}$  transition has to be controlled. For optical pumping and probing purposes, the two circular and one linear polarization are needed at different times in an experimental sequence.

The polarization control of the beam is achieved by the use of an electro optic phase modulator (EOM). The polarization before the modulator is cleaned by the use of a Glan Taylor polarizer with a  $1 \times 10^5$  extinction ratio (ThorLabs®GT-10). The electro optic modulator neutral axis is rotated by  $45^\circ$  compared to the input vertical polarization, allowing to transform the input linear polarization into a linear,

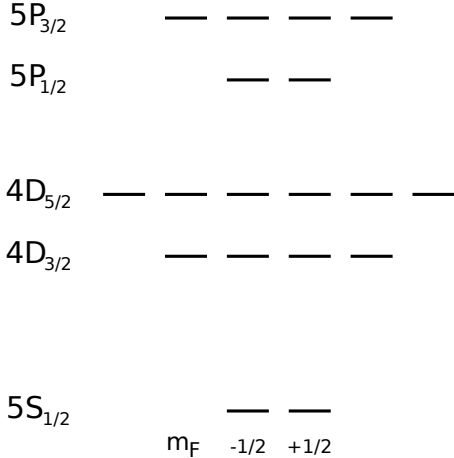


Figure 3.18: Levels of  $\text{Sr}^+$  with the Zeeman sublevels. With a magnetic field along the trap axis we can address the  $^5\text{S}_{1/2}(m_F = +1/2) \rightarrow ^5\text{P}_{1/2}(m_F = -1/2)$  and  $^5\text{S}_{1/2}(m_F = -1/2) \rightarrow ^5\text{P}_{1/2}(m_F = +1/2)$  with the two opposite circular polarizations. This allows for the pumping and probe atoms in the  $^5\text{S}_{1/2}(m_F = -1/2)$  and  $^5\text{S}_{1/2}(m_F = +1/2)$  states

circular left or circular right polarization, depending on the voltage applied to the electrodes. The successful operation of the EOM is checked using another polarizer and a set of zero order waveplates.

The birefringence of the optical elements between the modulator and the ion cloud is compensated by using a zero order half waveplate and a zero order quarter waveplate. These waveplates are adjusted in order to obtain the expected polarization just after the vacuum chamber for the three polarizations needed. We have noticed a few percent polarization mismatch which is probably due to the polarization dependent losses of a non polarizing beam splitter cube (ThorLabs®BS016) present in the optical path.

The electro optic modulator used has a  $\pi$  voltage (the voltage needed to create a  $\pi$  phase difference between the two axis) of about 1000 V at 422 nm. To obtain fast response times, an electronic circuit for switching the high voltage (HV) sent in the EOM has been developed. This circuit, depicted on Figure 3.19 is based on HV field effect transistors driven using fast optocouplers isolating the TTL inputs from the control computer card.

The fast optocouplers possess internal amplifiers and need their own power supplies relative to the output low point. In order to avoid isolation issues, these power supplies are provided by batteries. The lifetime of the batteries is in the order of 200 working hours. This circuit is able to switch between three voltages which are adjusted for delivering the three wanted polarizations. Typical switching time is  $\approx 10 \mu\text{s}$  for rising voltages and  $\approx 100 \mu\text{s}$  for high to low voltage switching. The switching time is mainly limited by the capacitance of the 1 m coaxial cable between the circuit and the EOM.

### 3.8 Femtosecond photo-ionization laser

In the following, the characteristics of the photo ionization laser and its doubling system will be presented.

Neutral strontium atoms are ionised driving a two-photon transition towards

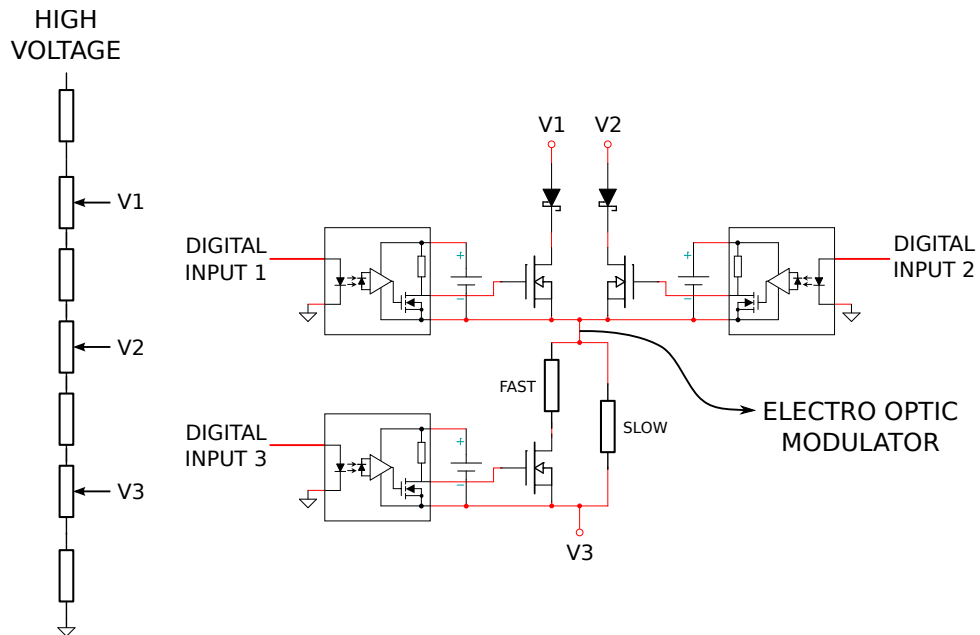


Figure 3.19: Circuit for the fast commutation of the Electro Optic Modulator  
 Each transistor commutes a voltage to the electrode. The bottom transistor is needed for faster switching from high to low voltages. The three voltages are made by a resistor bridge with fine tuning provided by variable resistors. The transistors (STP4N150) are driven using an external TTL signal through opto-isolators (A6N37) which are powered with batteries to avoid isolation issues.  
 The stabilization capacitors between the voltage bridge and the transistors are omitted on this sketch.

a self-ionising level [Removille 09b, Kirilov 09]. The photoionizing laser pulses are issued from a doubled Ti:Sa oscillator (Tsunami, Spectra-Physics) with a central frequency of 695 THz ( $\lambda = 431$  nm) and a pulse duration of  $\approx 150$  fs. The spectral width associated to these ultrafast pulses ( $\approx 10$  THz) makes this loading process insensitive to both Doppler effect and isotope-shift, providing samples with a composition that respects the natural abundances. A summary of the technical characteristics of the laser are reported on Table 3.1

Optical power	1.5 W @ 860 nm
Repetition rate	80 MHz
Pulse Width	$\approx 150$ fs
Bandwidth	$\approx 10$ nm(adjustable)
Beam diameter	2 mm

Table 3.1: Characteristics of the mode locked femtosecond Ti:Sa laser

The 862 nm output beam is focused using an achromatic lens ( $f=30$  mm) onto a 250  $\mu\text{m}$  thick BIBO crystal from CASIX for second harmonic generation. At these power levels, regular damage of the crystal has been noticed, which reduces significantly the doubling efficiency after  $\approx 100$  hours of operation. The crystal damage is localized on the laser focus spot, allowing to move the crystal for recovering normal operation. After the crystal, the blue beam and the pump are separated using dichroic mirrors. This allows us to use the depleted pump to pump another crystal for the other ion trap experiment of the group. After doubling, 500 mW of blue power is obtained, which corresponds to a 33% conversion efficiency. This blue beam is expanded to a diameter of 1 cm then focused into the trap using a  $f=300$  mm lens.

The loading performances of this laser are detailed in chapter 4.

### 3.9 Imaging system

Trapped ions offer an excellent detectivity. The depth of the trap ( $\approx 20$ eV) allowing for the collection of the fluorescence from a strong cycling transition without losses. Moreover, in the context of this thesis large ion ensemble are used, thus providing a large signal (as can be seen on Figure 4.7) reducing the constraints on the imaging system. The ion cloud is imaged from one side and from above. The side imaging system consists in a Coolsnap EZ CCD camera (Roper Scientific™) and a standard  $f=85$  mm photo lens. The lens is attached to the camera using a homemade extension tube. The camera pixels are 6.45  $\mu\text{m}$  large and the magnification of this imaging system is 1:2.

The imaging system above the cloud is similar to the side one and consists in a Prosilica GC1600 camera with 4.4  $\mu\text{m}$  pixels and a  $f=58$  mm photo lens. The magnification of this system is 1:3.

A software has been developed for the control of the top camera and is available at : <http://github.com/braice/Camera-interface>

High resolution images in this manuscript were taken with a modified side imaging system. For the high resolution images, the imaging system consisted in two camera objectives and a Prosilica GC1020 camera. The first objective is a Canon EF Macro-lens 100 mm f/2.8 placed just outside the viewport ( $\approx 30$  cm away from the trap). With this distance, we obtain an image with a magnification of about 1:1 approximately 10 cm after the back ring of the lens. This virtual image is magnified using a standard 50mm camera objective used in the reverse direction. The camera sensor is placed  $\approx 15$  cm after the front lens of the second objective. The position of the second objective is adjusted to obtain the focus on the camera sensor. The whole system allows to obtain a magnification of  $\approx 2:1$ .

## 3.10 Magnetic field control

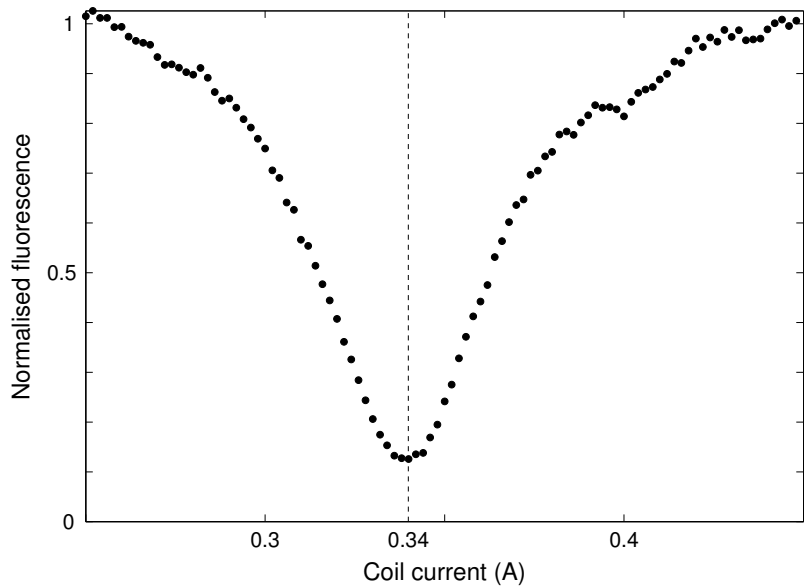


Figure 3.20: Typical fluorescence versus current in the Z coil with X and Y fields set to 0.

In all the experiments in this thesis we are working with a magnetic field along the trap axis (Z) that defines a quantization axis that coincides with the propagation axis of the probe. The experiments performed are sensitive to the magnetic field direction but, to the first order, not to the magnetic field inhomogeneities. The control of the magnetic field in the trap is achieved by the use of 3 set of coils outside the vacuum chamber. In order to null the field at the center of the trap, we use the presence of a one photon dark state on the repumping transition [Berkeland 02]. For  $B = 0$  the ions are trapped in a dark state, superposition of the four Zeeman sublevel of the  $4D_{3/2}$  state, for any polarization of the repumper. By measuring the fluorescence versus the current on each coil, we are able to find the zero of the magnetic field.

To ensure that we are in the zero of the magnetic field and not being in another dark state, we vary the polarization of the repumping laser with a set of waveplates. A typical fluorescence measurement as a function of  $B$  is depicted on Figure 3.20 showing a clear minimum for  $I_Z = 0.34\text{ A}$ . The residual fluorescence is due to magnetic field gradients (on a  $\approx 5\text{ mm}$  long cloud) and imperfect compensation on the other axis. In the extinction point, the fluorescence does not reappear by changing the repumper polarization. The field generated by the Z coil is estimated to be  $\approx 2\text{ G/A}$ , then the sensitivity of this method is  $\approx 2\text{ mG}$  deduced from the uncertainty on Figure 3.20.

# Chapter 4

## Large coulomb crystals

One important goal of this work is to achieve strong light-matter coupling with well controlled system. Reaching high optical density with trapped ions is particularly challenging but essential for developing a ion based quantum light-matter interface.

Due to the strong repulsive interaction between ions, achieving a significant optical thickness in an atomic sample of cold trapped ions is a challenge. For example, in the case of  $\text{Sr}^+$ , for a cloud of  $2\text{ cm} \times 200\text{ }\mu\text{m} \times 200\text{ }\mu\text{m}$ , in order to reach a single pass absorption of 50%, a crystal of a few  $10^7$  ions is needed<sup>1</sup>.

Wigner ion crystals of more than  $5 \times 10^5$  ions have been demonstrated in Penning traps which are not affected by radio-frequency heating [Itano 98, Mitchell 98]. In linear Paul traps coulomb crystals of 10 000 ions which exhibit a 3D arrangement were demonstrated [Mortensen 06] and crystals with more than  $10^5$  ions were demonstrated [Drewsen 98].

There are several factors which can limit the maximum number of ions in a Paul trap : Trap volume, density, collisional heating, radio frequency heating and the ratio between loading rate and lifetime.

### 4.1 Trap density measurement

As seen in section 3.1, the key parameter which controls the ion density is the trap stiffness. This stiffness can be computed theoretically from the trap voltage and the geometrical characteristics of the trap. These calculations can suffer from the various geometrical imperfections of the trap and give only access to a rough order of magnitude of the cloud density.

By applying a sinusoidal excitation on the trap compensation electrodes (parallel to the main electrodes) we can excite the ion cloud when the excitation frequency is resonant with one of the main trap frequencies (“tickling” excitation). This excitation can be detected by a change in the fluorescence of the ion cloud. If the cooling laser is significantly red detuned ( $\approx 5\Gamma$ ), when the ion cloud is excited the Doppler effect will induce a fluorescence increase.

---

<sup>1</sup>The model for estimating single pass absorption is detailed in chapter 7

By repeating this analysis for different radio frequency powers, we are able to deduce the dependence of the radial frequencies with the trap RF voltage. The axial frequency has been measured to be  $\approx 20$  kHz with an endcap voltage of 50 V. The tickle measurements results are depicted on Figure 4.1. This measurement has been performed on a natural strontium crystal, a comparison with an enriched crystals shows that the measured frequency is dominated by the A= 88 isotope. The uncertainty on the measurement is  $\pm 5\%$ .

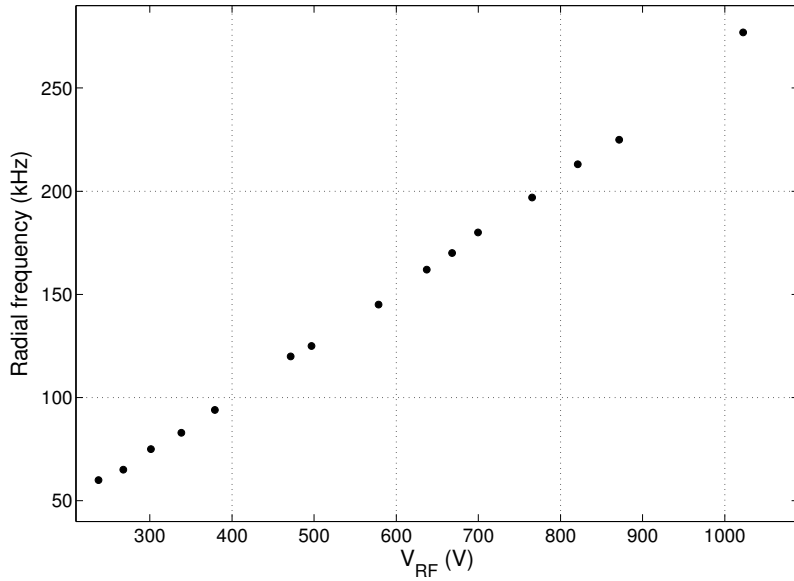


Figure 4.1: Radial frequency versus  $V_{RF}$ .

From these measurements the density can be computed using the following expression (see section 3.1 page 23) :

$$n = \frac{m\epsilon_0}{e^2}(\omega_x^2 + \omega_y^2 + \omega_z^2)$$

The results are depicted on Figure 4.2.

Using the expressions derived in section 3.1 we can check the consistency of this measurement with the expected densities and frequencies obtained from the measurement of the RF voltage (Figure 3.6 page 29). For  $P = -10$  dBm we have a peak to peak voltage on each bar of 750 V, this corresponds to a radiofrequency amplitude of  $V_{RF} = 750$  V. This gives a radial frequency of  $\omega_x = \omega_y = \frac{q}{\sqrt{2}}\omega_{RF} = 2\pi \cdot 168$  kHz, this is 20% lower than the measured value. This corresponds to a theoretical density of  $n = 2\frac{m\epsilon_0}{e^2}\omega_R^2 = 1.1 \times 10^{14} \text{ m}^{-3}$ , this is 40% lower than the one measured :  $1.5 \times 10^{14} \text{ m}^{-3}$ .

The new resonator allowed us to reach high densities about  $n = 3 \times 10^{14} \text{ m}^{-3}$  while keeping a q factor low in a high volume trap.

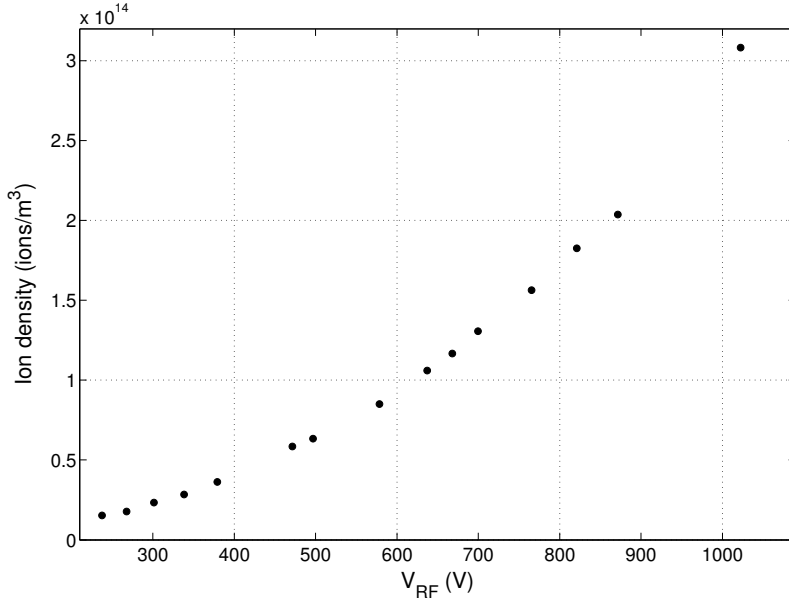


Figure 4.2: Ion density versus  $V_{RF}$ . The density is calculated from measurement of the radial frequencies made by “tickle” with a radial frequency of 20 kHz.

## 4.2 Improvements on the loading rate

In the experimental setup formerly developed in the group, the typical loading rate was about 100 ions/s [Removille 09b] which means that more than 12 hours were needed to load a cloud containing five million ions. Higher loading rates of 3000 ions/s have been obtained by the group of M. Drewsen [Herskind 08].

The loading rate can be improved in two ways : increasing the neutral flux and increasing the ionization probability.

A too high flux of neutral atoms can increase the chamber pressure and, more importantly, if metal gets deposited on the trap electrodes, it can induce anomalous heating of the ions [DeVoe 02]. The key parameter increase significantly the loading rate is the photo-ionization probability.

In the following, the strontium oven characterization will be described as well as the results on the photo-ionization rate.

### 4.2.1 Strontium oven characterization

The oven is made from a tungsten wire of 100  $\mu\text{m}$  diameter and 10 cm long wounded in a spiral in which a strontium dendrite sits (Sigma Aldrich 99.9% pure). This wire is held in a metallic housing with an aperture of 3 mm to collimate the atomic beam. The top of the oven housing is visible on the bottom right of Figure 4.7.

The oven has been characterized by loading an empty trap 10 s and measuring the final fluorescence for different oven currents. The results are depicted on Figure 4.3.

The exponential fit of the experimental data gives a characteristic current of

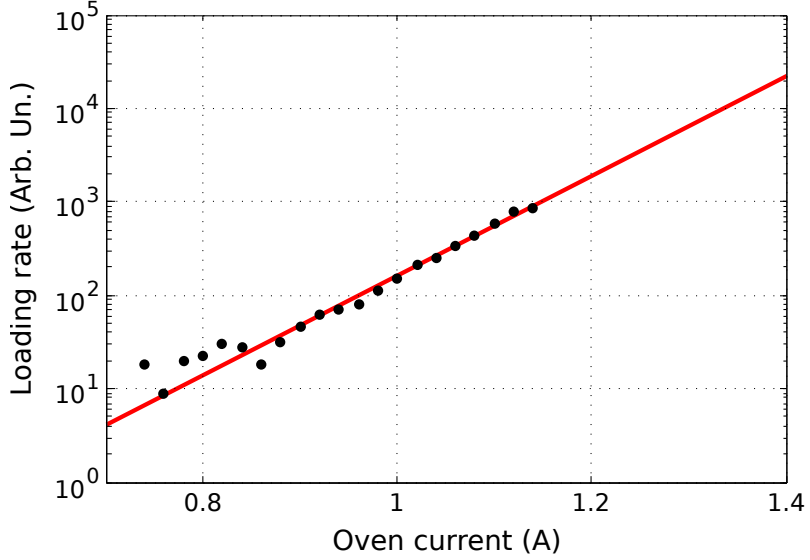


Figure 4.3: Loading rate versus oven current.

Since the real loading rate depends on the photo-ionization laser the vertical axis is in arbitrary units.

The red line is an exponential fit of the data. The loading rate increases by a factor two for each 0.055 A current step.

55 mA. This current is the current needed to double the loading rate. This exponential model reproduces well the behavior in the range of current used.

#### 4.2.2 Photo-ionization characterization

When increasing the photo-ionization power, it is important to verify that the loading rate scales quadratically with the laser intensity as expected for such a 2-photon process. The experimental technique is similar to the one used for characterizing the strontium oven. The results are depicted on Figure 4.4.

The dependency of the loading rate versus the photo ionization laser focus position has also been studied. The position of the focus strongly influences the time to get an ion crystal. When the focus is far from the trap center, the ions are created with a significant potential energy. This energy has to be removed from the system by the laser-cooling. Since in ion traps the cooling efficiency strongly depends on the temperature, the time needed to reach the crystalline phase is significantly increased. Once a crystal of a few thousands ions is in the trap, this crystal act as a cold bath for newly created ions such keeping the cooling efficiency high. In this way, even if the ions are created far from the center, they are kept in the trap and cooled rapidly, explaining the low influence on the loading rate of the distance between the focus of the photo-ionization laser and the trap center.

Let us remark that this study on photo ionization allowed for discovery of a new phenomenon which leads to the production of  $\text{Sr}^{2+}$  ions by removing an electron to

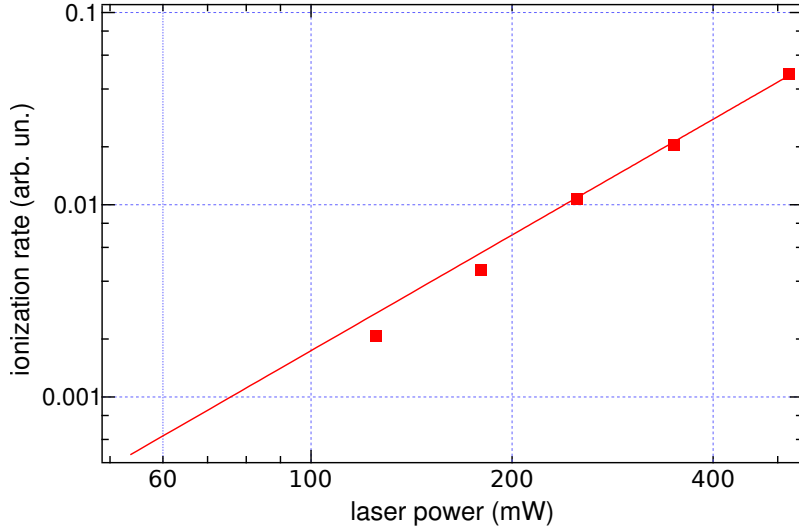


Figure 4.4: Loading rate versus photo-ionization power. This curve have been obtained by measuring the loading time to obtain a given cloud size (containing a few  $1e3$  ions) versus the photo-ionization laser power. The oven current have been chosen to obtain a loading time of 20 s at  $P = 520$  mW  
We see the good dependency in  $I^2$  and no saturation effect.

the  $\text{Sr}^+$  ions with the help of a three plus one photon process.<sup>2</sup>

The possible issue represented by the production of  $\text{Sr}^{2+}$  ions is avoided by displacing the focus of the photo ionization laser away from the trap center by  $\approx 2$  mm. This distance is sufficient to avoid the production of  $\text{Sr}^{2+}$  ions from a crystallized sample but not from a melted sample. Therefore, our strategy consists in two steps. First we create a small Coulomb crystal by loading during some seconds and waiting until the whole sample crystallizes. Then we resume the loading that now add ions directly to the crystal.

### 4.2.3 Final loading rate

With an oven at 1.35 A and 500 mW of photo-ionization laser power we obtain a loading rate of 1100 ions per second. This allows to load million of ions in about one hour.

This loading rate whereas being clearly improved, is still lower from what we could expect from theory. This improvement of the loading rate is an important step for studying large ion ensembles. Even if the lifetime of ions in the trap is very long, it is limited by chemical reactions and laser locks. When a laser goes out of lock, the cooling disappear and the ion cloud leaves the crystalline state. For ion clouds containing several millions of ions, we are not able to recover them due to the radio frequency heating being significantly larger in the liquid and gas state than in

---

<sup>2</sup>Paper in preparation

the crystalline state [Ryjkov 05].

In order to improve the loading rate, the oven could be improved by having a better thermalization and collimation allowing an higher working temperature.

Other schemes are also developed. The loading rate can be greatly increased by first trapping and cooling the neutral vapor using a standard neutral atom trap then photo-ionize the cloud to load an ion trap [Cetina 07]. This scheme has not been used with strontium but people already demonstrated successful trapping and cooling of neutral Strontium [Katori 99].

## Results and chapter conclusion

As illustrated on Figure 4.5 we have demonstrated successful loading and cooling of ion coulomb crystals containing more than three million ions with a density of  $3 \times 10^{14}$  ions/m<sup>3</sup>.

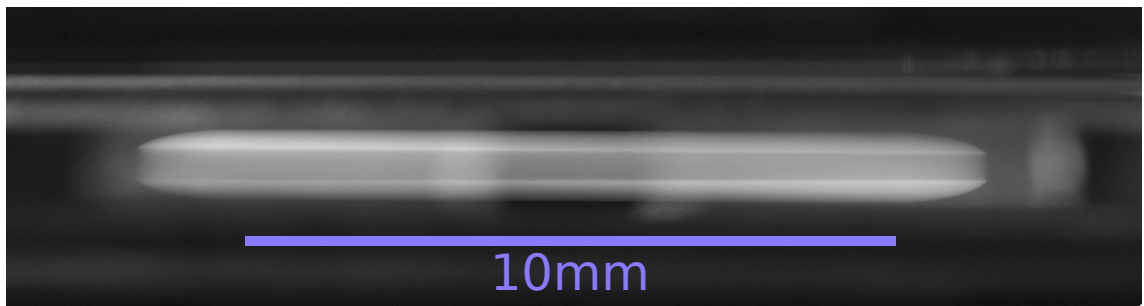


Figure 4.5: Top picture of a crystal containing  $2.8 \times 10^6$  ions. The non elliptical shape is due to the anharmonicity of the axial confinement potential. The dark region inside is due to the isotopes A=86 and A=87 which are not shined on this picture.

Cloud density  $3.1 \times 10^{14}$  m<sup>-3</sup>, diameter 1080 μm length 13.2 mm. Quasi perfect cylinder.  $V = 1.2 \times 10^{-8}$  m<sup>3</sup>

At these densities, in our linear Paul trap the crystal melts when its radius becomes larger than a millimeter. For example, the crystal depicted on Figure 4.5 melted when the number of ions reached 5.5 millions. The influence of all the parameters on the radio frequency heating have not been studied in detail, so it is not possible to conclude if this limitation is due to the imperfections of our trap, to the choice of the trapping parameters or if its a more general limit.

In order to verify the crystalline nature of the ion cloud, high resolution pictures have been taken, by increasing the magnification of the imaging system. Figure 4.6 displays such a picture of a cloud containing about a million ion at a density of  $2 \times 10^{14}$  ions /m<sup>3</sup>.

We can clearly see ion layers which proves, at least a 2D arrangement. 3D arrangement cannot be seen, possibly because the temperature is too high [Mortensen 06].

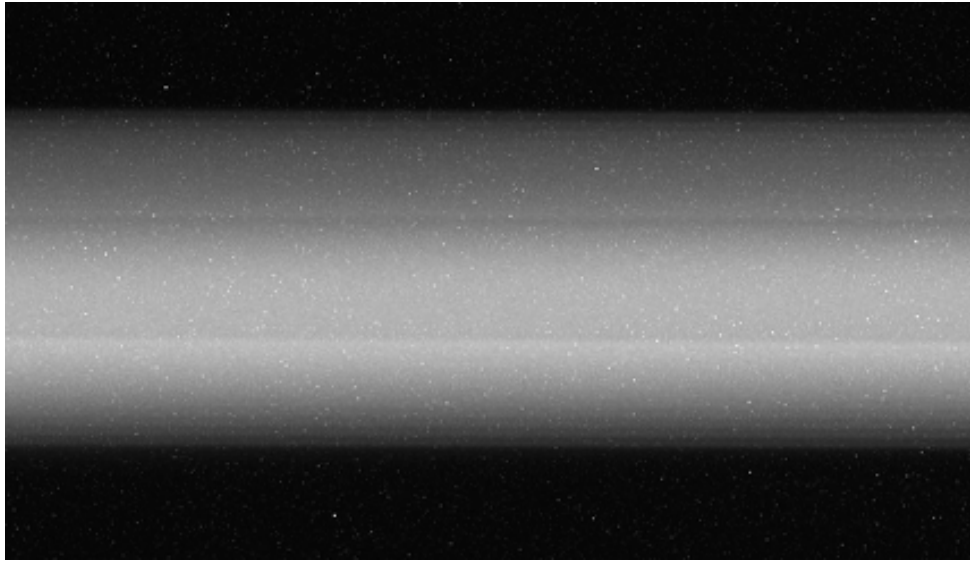


Figure 4.6: High resolution picture of a big cloud with a density of  $2 \times 10^{14}$  ions /m<sup>3</sup>.

We can see the layers proving the crystalline state of this ion cloud.

From these images, it is difficult to determine the value of the coupling parameter (defined in section 3.1).

Let us remark that these crystals are visible to naked eye. A picture obtained with a commercial photo-camera is shown on page 52, Figure 4.7.

These crystals contain more than one order of magnitude more ions than previously reported [Hornekær 02]. This regime is unexplored both theoretically and experimentally, making this system of particular interest for the study of radio frequency heating, heat transport in ordered system and more generally studies of large cold organized samples with long-range interaction.

This number of ions combined with the possibility of sympathetic cooling [Bowe 99] opens the way to quantum information experiments in a novel regime, different with respect to the collective strong coupling regime which has been recently achieved [Herskind 09].

Experiments demonstrating EIT and significant absorption with this system have been carried out during this thesis and are detailed in chapter 7.

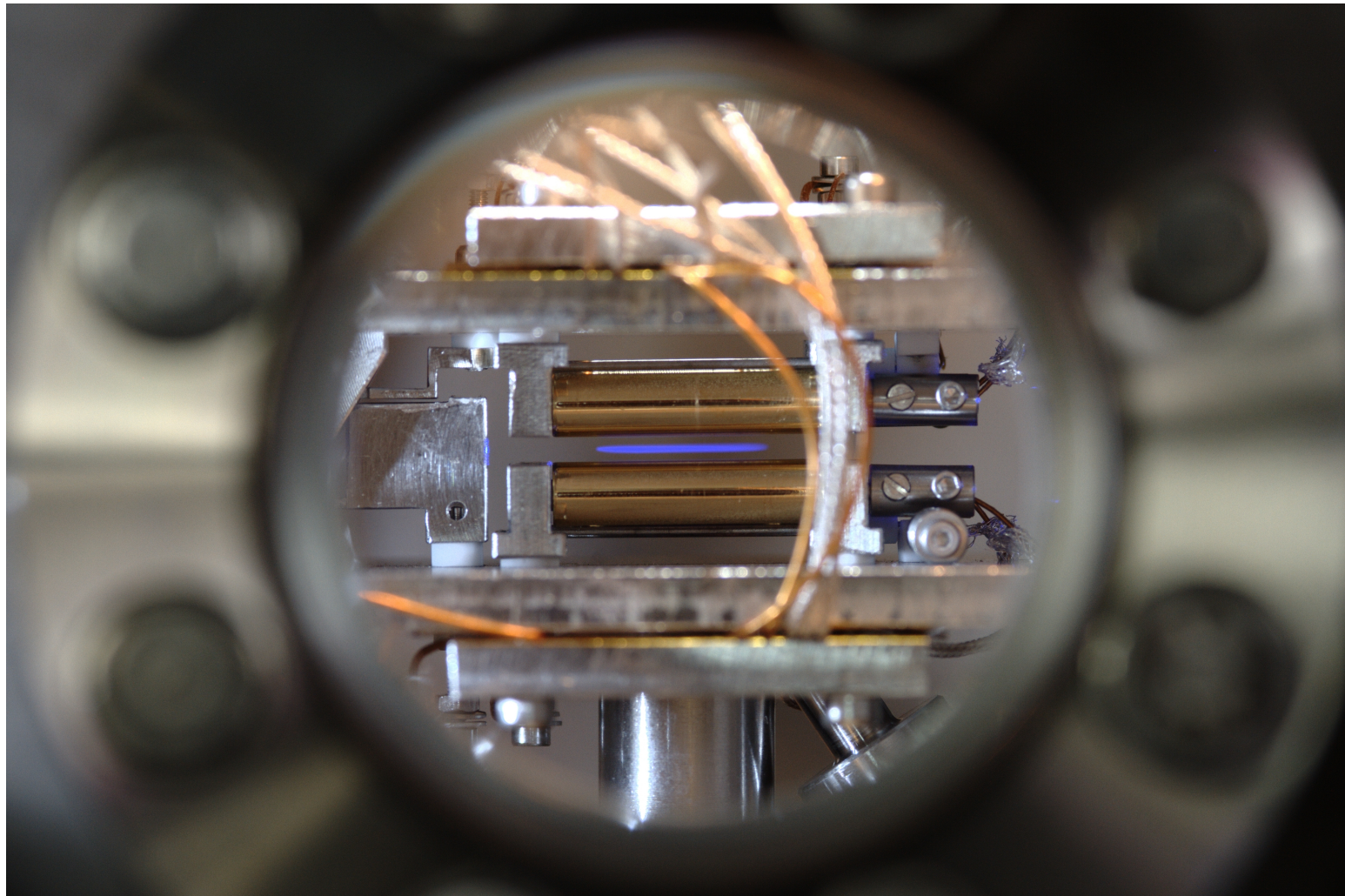


Figure 4.7: Picture of the trap containing a few million ions.

From inside to outside. Blue/violet is the fluorescence from the strontium cloud. The gold bars are the RF electrodes. On the side of the electrodes we can see the endcaps. On the bottom we can see the e- gun (not used in this work) and the strontium oven. Around is the vacuum view-port.

This picture was taken using a Canon EOS 7D + Canon EF 200mm f/2.8 L. The exposure time was 3 s at 400 ISO, f/5.6

# Chapter 5

## Isotopic enrichment

### 5.1 Introduction and goal of the method

In this chapter I will present an experimental technique that can be applied to improve and characterize sympathetic cooling in the case of multi-isotope Coulomb crystals. As explained in the introduction, sympathetic cooling is one of the most important resources of laser-cooled ions. It can be performed with different atomic species, or with different isotopes of the same atom if the isotopic shift is sufficiently large to allow independent laser addressing. In the latter situation the control of the isotopic ratio is important for an efficient cooling process. In the case of strontium, the natural abundances for the isotopes 88, 87, 86 and 84 are respectively 82.58%, 7.0%, 9.86% and 0.56%. In the context of this thesis, we are interested in using the A=86 or A=87 isotopes as an active atomic medium, while using the A=88 as a coolant. An efficient isotopic enrichment would allow us to remove the unwanted isotopes and to control the proportion of the “refrigerator”. For example, if one wants to use the A=87 isotope as a working isotope, its proportion is relatively low and it can be necessary to enrich the sample, removing the A=86 and decreasing the amount of A=88 in order to reach a properly balanced ratio between the coolant specie and the active medium.

The isotopic control can be obtained using enriched sources [Benhelm 08] which are expensive and difficult to obtain. Another solution is to perform the enrichment by taking advantage of the trapping set-up. Several methods reaching this purpose were demonstrated. In particular several groups reported successful enrichment by adjusting the photo-ionization parameters in a way that increases the isotopic selectivity [Lucas 04, Mortensen 04, Tanaka 07]. This method has the advantage to only load the wanted isotopes in the trap, does not induce heating but suffers from a lack of selectivity in certain cases. The other major strategies for isotopic enrichment are based on selective heating and cooling, either by laser, non linear resonances or tickle [Alheit 96, Hasegawa 00, Toyoda 01]. All these methods induce heating of the whole ion sample which is a major limitation for large coulomb crystals and were only demonstrated for small ion crystals.

Here we demonstrate an isotopic enrichment method based on radiation pressure

and control of the axial confinement allowing for the control of the ratio between the coolant and the isotopes of interest. Our method being very selective, it allows to prepare pure samples of rare isotopes making experiment on rare isotopes more flexible. Moreover it can be combined with isotopic enrichment methods based on the photoionization selectivity. In the following we will first describe the ingredients of the method: spatial segregation, and radiation pressure, then describe a simulation tool which we have used to study the feasibility of this method and finally we will describe the experiment and the results obtained.

## 5.2 Ingredients for isotopic enrichment

### 5.2.1 Radial separation

Ion traps mass selectivity has been widely used, in particular in mass spectrometers. By tuning the trap parameters it is possible to have small stability regions thus reaching great mass selectivity. This is the most used property of quadrupolar ion traps. As described in chapter 3 we are operating the trap in the first stability region, such that all the strontium isotopes are stable.

In a radio-frequency trap, after averaging out the “fast” micromotion component, the stiffness depends on the mass. In particular the trapping force is stronger for lighter ions, according to the expression

$$\omega_R = \frac{1}{m} \frac{eV_{RF}}{\sqrt{2}R^2\omega_{RF}}$$

At a distance  $r$  from the trap axis, the potential energy of an ion scales then as  $r^2/m$  so the energetic cost of an ion away from the center for increasing mass decreases. This effect is almost invisible on hot samples (for which the kinetic energy is much greater than the interaction energy:  $\Gamma \ll 1$ ), but when the ions are crystallized, the potential energy term dominates and the mass effect becomes visible. This phenomenon induces a radial segregation clearly visible in Figure 4.5.

This effect tends to organize the cloud in axial concentric shells containing ion of different masses with clearly defined edges. This leads to a first method of isotopic enrichment: by lowering the radio frequency field amplitude the heavy ions are removed from the trap by leading them to collide with the electrodes. This method is mostly effective for large ion clouds.

In order to be able to enrich successfully we will combine this effect with the radiation pressure induced by the cooling lasers.

### 5.2.2 Radiation pressure

When atoms interact with a laser beam they undergo a force due to the momentum transfer between the photons and the atoms. It is studied since a few decades

[Ashkin 70] and can be expressed as follow :

$$F = \frac{\hbar}{\lambda} \frac{1}{\tau_N} f$$

Where  $\tau_N$  is the lifetime of the excited state (7 ns for  $\text{Sr}^+ 5P_{1/2}$  state) and  $f$  is the proportion of atoms in the excited state.

Calculating analytically the ion arrangement in a crystal, taking in account the mass dependency and the radiation pressure is analytically difficult (or impossible). The ion arrangement which minimize the potential energy can be calculated numerically up to a few million ions. This kind of calculation can give an insight on the ion arrangements for various trapping parameters thus allowing to study the feasibility of the isotopic enrichment method. A simulation tool has been developed and will be described in section 5.3.

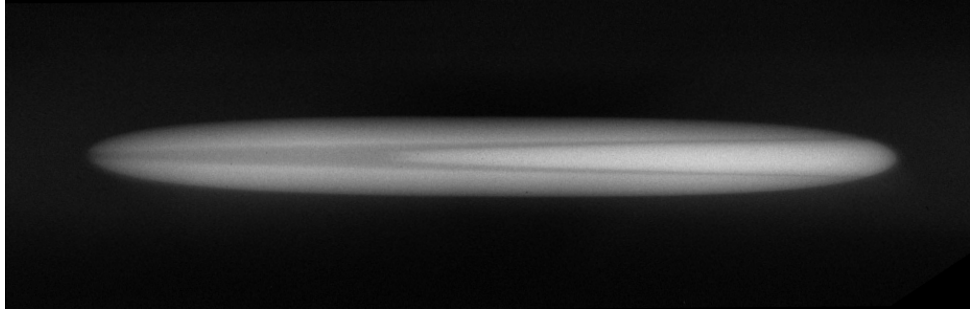


Figure 5.1: Natural strontium ion cloud (density  $\approx 1 \times 10^{14}$  ions  $\text{m}^{-3}$ ,  $\approx 5$  mm long) with counter-propagating cooling lasers (similar intensities and detunings  $\approx -2\Gamma$ ) for the  $A=88$  and  $A=86$  isotopes. We clearly see a reorganization of the ions which is the result of the competition between radiation pressure and the axial confinement. The dark zone in the middle are the  $A=87$  and  $A=84$  ions which are not addressed by the cooling lasers. In the tail of the bright  $A=86$  ions we see a small dark region which corresponds to the 0.56% of  $A=84$  ions.

Experimentally, radial segregation effects are strong as it can be seen on figure 5.1. The ions reorganize themselves in a triangular shape because of the competition between the radiation pressure which would bring all the ions of the pushed isotope on one side and the mass dependent radial confinement which tends to keep the cloud in an axial shell structure. In other words, if we push the lighter ions on one side, some of them will increase their distance to the trap axis. However, this process has an energy cost because they take place of heavier ions that are less confined.

This axial segregation is the basis of the proposed enrichment method. The precise shape of the Coulomb crystal induced by such a segregation of the different isotopes depends on the radial confinement and on the amount of radiation pressure. Let us mention that the shape of the axial potential (that is not harmonic in our trap) also influences the final shape of the crystal. To study the possibility for this axial segregation it is possible to perform simulations described in the next section.

## 5.3 Simulations

### 5.3.1 Position of the problem

The goal of this simulations is to find the ion arrangement which minimizes the potential energy, taking into account the radiation pressure, the trap confinement (radial and axial) including the mass dependence and the Coulomb interaction between the ions.

The simulation is based on minimization using gradient descent algorithm. For a given ion arrangement, the corresponding energy is computed together with its gradient (derivative of the energy versus the ion coordinates). Then it is possible to follow the gradient to reduce the overall energy. This method is extensively used and benefits from an abundant literature.

The total energy contains several terms with different algorithmic complexities. The potential energy term originating from radiation pressure and trap confinement only depends on the ion position, so it has a linear  $O(N)$  complexity. On the other hand, the Coulomb interaction energy is the sum of the interaction energy of each ion with all the others so this calculation has a quadratic complexity  $O(N^2)$ . For large ion numbers  $N \approx 10^6$  this calculation becomes too expensive in computation time to be performed on a normal desktop computer (several days of computation would be needed).

In ion systems the screening is an important effect and the details of the local arrangement of the ions distant from the ion of interest doesn't change significantly its potential energy. This allows us to perform an approximation consisting in computing the interactions exactly for the nearest neighbors but considering an average potential for distant ions that are grouped. This procedure needs to sort the ion positions at each iteration to define hierarchically the groups of ions. The overall complexity is dominated by the complexity  $O(N \ln(N))$  of this sorting operation: the calculation becomes accessible for a standard computer. Romain Dubessy, former member of the group has a strong expertise in this kind of algorithms, in particular for simulating the ion motion in a Paul trap in the presence of laser cooling. His experience strongly contributed to the writing of the current simulation program.<sup>1</sup>

The gradient descent method, in the case we are interested in, suffers from two issues which need to be addressed.

A first issue is a particular version of the local energy minimum problem. A light ion can remain at the edge of the cloud even if it's energetically better for it to be closer to the center. This ion on the edge is a local minimum for the system, because having it in the center gives a lower total energy but in order to move it to the center an energy barrier must be overpassed. Several methods are used to avoid local minima in gradient descent algorithms such as simulated annealing. In the particular case of ion cloud arrangements it is possible to use a simpler method to overcome this issue. By adding an iteration to the gradient descent which checks if making a permutation between two ions of different masses can improve the situation, we

---

<sup>1</sup>The program is available at : <http://github.org/braice/FindMinimum>

solved this problem in an efficient way without increasing the complexity.

The second issue is the choice of the gradient descent algorithm. The naive approach consists in multiplying the gradient by a constant to compute the new positions :  $\vec{P}_{N+1} = \vec{P}_N + \alpha \vec{G}$  where  $\alpha$  is a constant,  $\vec{P}_N$  the position vector at iteration  $N$  and  $\vec{G}$  is the gradient. This approach can lead to slow convergence and/or oscillations around the minimum. Several approaches can be used to overcome this problem, most of the methods being based on a dynamic  $\alpha$  depending on higher order energy derivatives and previous  $\alpha$  values. In our case we obtained satisfying results by adopting a simpler approach consisting in increasing or decreasing  $\alpha$  at each step choosing the value which provide the largest decrease on the final energy as a new value. This approach leads to two phases. A first phase from the initial condition to an almost crystallized clouds during which the ions need to be moved significantly and  $\alpha$  increases. When the ion cloud approaches the crystalline state, important ion displacements do not decrease the energy of the system anymore and  $\alpha$  decreases, allowing for the final adjustment of the ion positions.

### 5.3.2 Results

A typical result of a simulation is depicted on Figure 5.2. This simulation is in excellent qualitative agreement with the experimental observations.

This simulation tool allowed us to understand the subtle aspects of simultaneous segregation by mass and radiation pressure in a radio frequency trap. Moreover it demonstrated the feasibility of isotope enrichment (see next section) and could be used in the future to optimize this process for different traps and parameters.

## 5.4 Experimental isotope enrichment

The use of radiation pressure allows us to perform an efficient axial separation of the ion isotopes. In order to perform the enrichment it is necessary to control the axial confinement potential to selectively eject ions from the trap.

### 5.4.1 Endcaps electrodes control

By adjusting the voltages applied to the endcap electrodes, it is possible to lower progressively the axial trapping potential allowing the ions at the cloud edge to leave the trap. The simulated pseudo potential for two different endcap voltages set is shown on Figure 5.3. The potential due to each electrode of the trap has been calculated with the software *Simion* ®<sup>2</sup>.

As can be seen on the simulation of the pseudo potential on the trap axis (Figure 5.4), the potential is still confining even with the endcap electrode voltage set to 0 V. This is due to the way the radio frequency field lines close at the end of the radio frequency electrodes.

---

<sup>2</sup><http://simion.com>

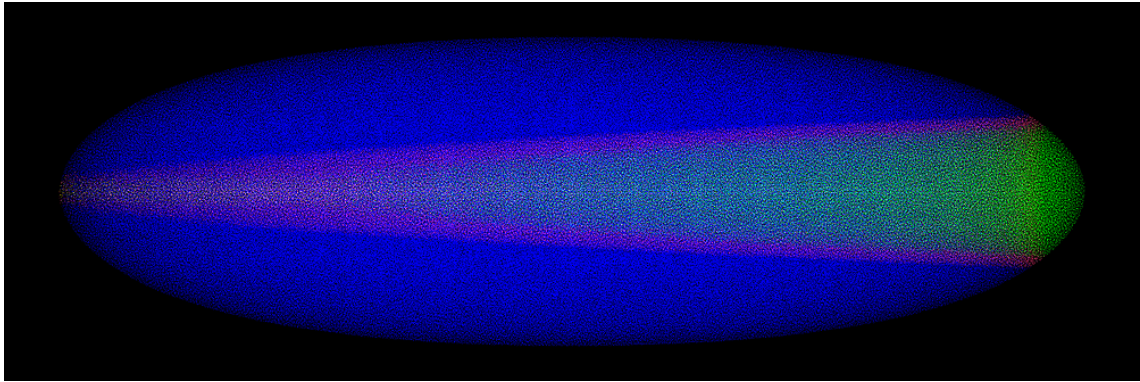


Figure 5.2: Simulated image of a multi-isotope Coulomb crystal containing  $10^6$   $\text{Sr}^+$  ions with a natural abundance probability. The image is obtained by simple projection of the ion position without any attempt of simulating the depth of field of the imaging system.

The calculated ion positions minimize the potential energy taking into account the different masses, the radiation pressure and the trapping potential (harmonic).

The  $^{88}\text{Sr}^+$  ions are in blue, the  $^{86}\text{Sr}^+$  in green, the  $^{87}\text{Sr}^+$  in purple and the  $^{84}\text{Sr}^+$  in white.

The  $^{86}\text{Sr}^+$  ( $^{88}\text{Sr}^+$ ) ions are pushed to the right (left) via radiation pressure.

This simulation have been performed with the following parameters: For  $^{88}\text{Sr}^+$   $\omega_r = 263 \text{ kHz}$

For all isotopes  $\omega_z = 35 \text{ kHz}$

Laser detuning equal to the natural linewidth and with a saturation parameter  $s = 0.17$

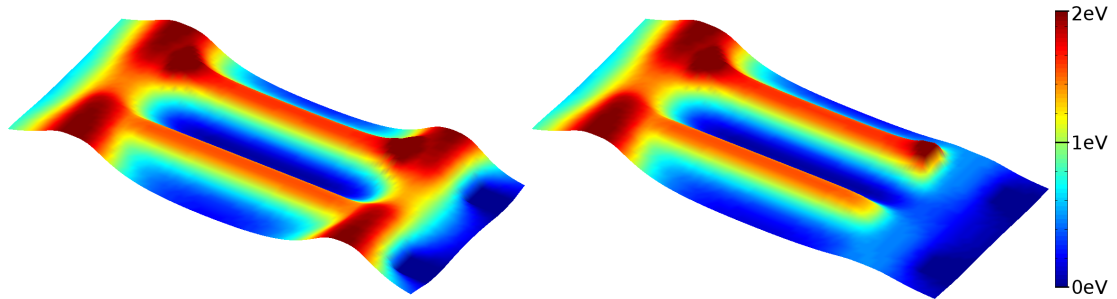


Figure 5.3: Trapping potential for two endcaps configurations commonly used for isotopic enrichment.

On the left part : normal trapping

On the right part : one of the endcap is lowered to allow escaping of one strontium isotope

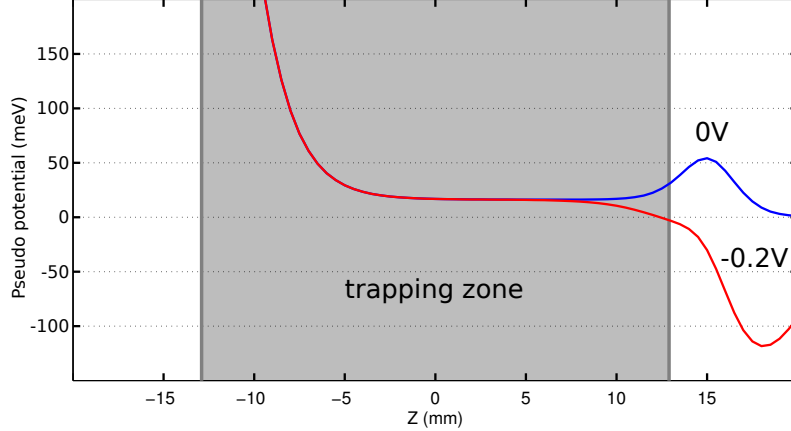


Figure 5.4: Pseudo Potential on the trap axis for two endcaps configurations. This pseudo potential includes contributions of the Radio Frequency field (1000 V symmetric) and the endcaps. The left endcap is set to 1 V. The grey zone corresponds to the length of the Radio Frequency electrodes. The blue curve is obtained with the right endcap set to 0 V. We see that in this case, the ions can still be trapped. The endcap voltage has to be set to a slightly negative voltage in order to open the trap along the z axis. For example  $-0.2\text{ V}$  represented by the red curve.

Because of this phenomenon it is necessary to apply slightly negative voltages to the endcap electrodes to perform selective ejection. The electronic circuit depicted on Figure 5.5 has been used to generate such voltages controlled with a sufficient precision ( $\approx 10\text{ mV}$ ).

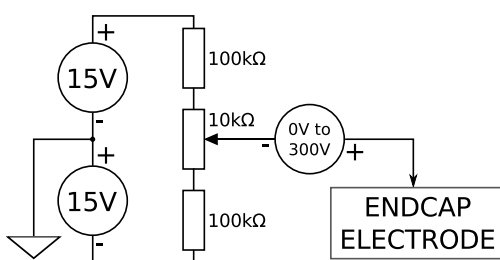


Figure 5.5: Circuit used for the fine control of the endcap voltage. The potentiometer allows us to add a voltage between  $-1.5\text{ V}$  and  $1.5\text{ V}$  to the main power supply. This voltage allows for a fine tuning of the axial confinement potential when the main PSU is set to 0V. It is put on the low side of the main PSU for safety reasons. Two of these circuits are implemented on the experiment.

For enriching an ion sample, the propagation directions of the lasers are adjusted in order to push the isotopes to be removed towards the controlled endcap and push in the opposite direction the enriched isotope. The radio frequency amplitude and the laser detuning are then adjusted to optimize the axial segregation of the isotopes at the cloud edge. The endcap high voltage source is then lowered before adjusting progressively the endcap voltage down to the “escape point” at which the unwanted

isotope gradually leaves the trap (characteristic procedure time of a few seconds).

## 5.5 Results and limitations

This method allows for a great selectivity and flexibility. From a naturally loaded cloud containing 0.56% of the A=84 isotope we are able to make a cloud containing almost 100% of A=84 ions. During the enrichment process, less than 20% of the A=84 ions contained in the original cloud are lost. To prepare this cloud, first all the A=88 ions of the original cloud are removed. Then the lasers are set to push towards the same direction the A=86 and A=84 ions, in order to remove the A=87 ions. Finally the A=86 ions are pushed towards the other direction and removed. A similar sequence allowed us to realize a balanced sample ideally suitable to perform simultaneous spectroscopy of the A=86 and A=84 ions as described in the chapter 6.

One of the main interests of this enrichment method consists in the optimization and control of sympathetic cooling in large ( $\approx 10^6$ ) ion clouds. For example it is possible to remove the “dark” or useless isotopes not addressed by the laser system and tune the proportions between the isotopes of interest. A typical example with the A=86 and A=84 isotopes is visible on Figure 5.6. As an example of usefulness of the method, we report in Table 5.1 the estimated achieved purity of the samples obtained in two cases: for a target of a pure  $^{84}\text{Sr}^+$  crystal and in the case of a 50% crystal of  $^{88}\text{Sr}^+$  and  $^{86}\text{Sr}^+$ .

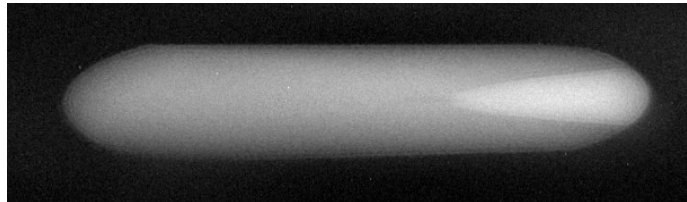


Figure 5.6: Enriched strontium cloud with A=84 ions pushed to the right, and A=86 ions to the left.

There is a few  $10^3$  A=84 ions and about  $10^5$  A=86 ions in this cloud. We can distinguish a few  $\text{Sr}^{2+}$  ions in the middle of the cloud, and a dark shell of A=87 and A=88 ions around the cloud which causes a small indent on the upper left edge.

This enrichment scheme is based on the possibility to bring ions to be removed to the edge of the trap using radiation pressure. This implies natural limitations: Lighter ions can be removed more easily than heavier ions. In their case the effect of radiation pressure is combined with the radial organization of the cloud as can be seen on Figure 5.2. This enrichment method is also more difficult to perform for tight traps for which the effect of radial arrangement becomes dominant over the radiation pressure. Typically in our trap, the enrichment became difficult for radial

Mass number	Natural strontium	Remaining ratio after enrichment	Remaining ratio after enrichment
88	82.58 %	$\approx 1\%$	$\approx 50\%$
87	7.0 %	$\approx 1\%$	$\approx 2\%$
86	9.86 %	$\approx 1\%$	$\approx 50\%$
84	0.56 %	$> 95\%$	0%

Table 5.1: Results example for work on rare isotopes and sympathetic cooling control. These results have been obtained with clouds containing a few  $1 \times 10^4$  ions. Typical unwanted losses for the kept isotopes are between 10% and 20%.

frequencies of  $\omega_R \approx 200$  kHz when the cloud contained more than a few  $1 \times 10^5$  ions. We also expect that the shape of the axial potential, flat bottom and very stiff edges (see Figure 5.3 and Figure 5.4) makes this method more difficult.

## Chapter conclusion

This isotopic enrichment method that we have developed provides a flexible way to enrich ion clouds with a very high selectivity without heating the ion sample. This scheme allowed us to control sympathetic cooling and to work with rare isotopes. Moreover this scheme can be combined with selective photo ionization, in order to increase the selectivity and providing a very efficient way to work with rare isotopes such as  $^{43}\text{Ca}$  (0.135%) which is of interest for quantum information experiments [Lucas 04].



# Chapter 6

## Isotope-shift measurements

### 6.1 Introduction

Ion traps, and in particular Paul traps, are an ideal tool for high resolution spectroscopy. Ion traps provide the possibility to perform measurements on a quasi ideal system. A single trapped ion can be almost perfectly decoupled from the environment, it experiences less than one collision per second (in a typical  $1 \times 10^{-10}$  mbar vacuum chamber) and the static electric and magnetic fields can be controlled. Since the trapping mechanism does not rely on the internal energy levels, its influence is extremely low and can be compensated with a very good precision [Margolis 04].

Ion traps, compared to neutral atom traps, are very tight and deep. This brings several interesting properties for spectroscopy applications. First the trapping lifetime is extremely long, reaching in some cases several days. This long trapping lifetime allows for measurements to be limited only by the lifetime of the probed levels. The motional energy levels can be sufficiently spaced for the use of very efficient cooling mechanisms such as sideband cooling [Heinzen 90]. This opens the possibility to cool down an ion to its vibrational ground state [Monroe 95], thus eliminating Doppler uncertainties. Finally the depth of the ion traps allows to perform repeated fluorescence measurement thus providing a great detectivity.

These properties allows clocks based on single trapped ions to surpass primary Cs fountain microwave standards, and reach unprecedented levels of precision (e.g. Aluminum, Mercury, Strontium and Ytterbium) [Rosenband 08, Margolis 04, Schneider 05], techniques proposed to reach precisions of  $10^{-19}$  with trapped ions [Campbell 12].

Finally the strong coulomb interaction between ions and the possibility to put different species or isotopes in the same trap open new possibilities in the context of spectroscopy with trapped ions. Among them, quantum logic spectroscopy has been demonstrated recently [Chou 10]. Quantum logic spectroscopy uses the quantum motional state as a bus to map the internal state of one ion onto the state of another. This mapping allows for the readout of the state of a "difficult-to-measure" ion (which does not possesses a strong cycling transition or a shelving state) by the readout of its neighbor.

As mentioned in the previous chapter, strontium possesses several natural isotopes that constitute a useful resource for sympathetic cooling. For that purpose it is important to know the frequency isotopic shifts of the transitions used for laser-cooling. The detailed level structure is reported in section D.2 page 132.

Moreover this kind of measurements helps to improve the understanding of the nuclear structure and may feed the models predicting the values of the atomic transitions. In the case of strontium II ions most of the isotope shifts are not well known. Isotope shift measurements on the  $^5S_{1/2} \rightarrow ^5P_{1/2}$  transition have been obtained for the first time in the 50's using hollow cathode spectroscopy and grating spectrometers : [Hughes 57]. Taking the A=88 isotope as a reference, the measured shift was  $\Delta\nu_{88,86} = -165 \pm 30$  MHz and  $\Delta\nu_{88,84} = -330 \pm 60$  MHz. More precise measurements were performed in the 80's using fast beam laser spectroscopy : [Silverans 88] [Buchinger 90] [Borghs 83]. The measured shift was  $\Delta\nu_{88,86} = -167(13)$  MHz and  $\Delta\nu_{88,84} = -361(25)$  MHz. Measurement with the same precision have also been done on the A=87 isotope which possess an hyperfine structure : [Sunaoshi 93].

The data available regarding the isotope shift on the metastable levels are more recent due to the weakness of this transition and has been obtained with trapped ions. The  $^5S_{1/2} \rightarrow ^4D_{5/2}$  is of particular interest for clocks. A precise measurement of the isotope shift between the isotopes A=88 and A=86 has been performed [Lybarger 11]. An isotope shift of  $\Delta\nu_{88,86} = 570.281(4)$  MHz has been measured. To our knowledge, there are no reported isotope shift measurements on the  $^4D_{3/2}$  level.

With laser induced fluorescence spectroscopy, we have measured with megahertz precision the absolute frequency of the  $^5S_{1/2} \rightarrow ^5P_{1/2}$  transition for the A=88, A=86 and A=84 isotopes and the isotopic shift on the  $^4D_{3/2} \rightarrow ^5P_{1/2}$  transition for the A=88, A=86 and A=84 couples. The results are presented on Figure 6.5.

In this work the isotope shifts have been obtained by studying the fluorescence spectra obtained by scanning the repumping laser frequency at fixed cooling laser frequency. These spectra contain the information on the  $^4D_{3/2} \rightarrow ^5P_{1/2}$  transition frequency. Such a 3-level scheme leads to the existence of a 2-photon dark-state involving the cooling and the repumping laser [Berkeland 02]. This dark state allows us to measure the difference in energy between the cooling laser and the  $^4D_{3/2} \rightarrow ^5P_{1/2}$  transition. Since the cooling laser is locked on a well known transition of  $^{85}\text{Rb}$  [Shiner 07] we also obtain the energy of this transition. In order to extract this information from experimental spectra, we fitted the data to a 3-levels, 2-lasers model. This model is detailed in section 6.2. In order to reduce the effect of laser frequency drifts, the measurements have been performed simultaneously on isotope pairs by using a sample containing  $10^3$  to  $10^4$  ions of each isotope.

This chapter is organized as follows: the model will first be presented. Then the experimental parameters used will be discussed. Finally the spectra are presented with their analysis.

## 6.2 Theoretical model

In a 3-level system, the shape and the apparent central frequency of the spectra depend on the laser intensities and detunings. The position of the maxima is shifted by the light shifts and the shape can be affected by power broadening. In order to take this phenomenon into account, to choose the optimal experimental parameters and to get maximum information from the spectra, a model has been developed.

To make the analysis relatively simple while being able to describe the observed spectra we model our system by a collection of independent 3 levels atoms which are interacting with two lasers for which the polarization is not taken in account [Gray 78].

Due to the presence of the two field dark state, the measured spectra can present a dip. The position of the dip mainly depends on the lasers relative detuning. Its contrast is reduced by any phenomenon which can reduce the coherence between the  $^5S_{1/2}$  and  $^4D_{3/2}$  levels such as laser linewidth, temperature, collisions ... We model all these effects by a phenomenological decoherence term between the  $^5S_{1/2}$  and  $^4D_{3/2}$  levels. This term models small broadenings of the dip.

The model gives the population in the excited level (proportional to the fluorescence) as a function of the following parameters also summarized in Figure 6.1 :

- $\Omega_b$  : The Rabi frequency of the violet laser
- $\Omega_r$  : The Rabi frequency of the infrared laser
- $\delta_b$  : The detuning of the violet laser from the resonance
- $\delta_r$  : The detuning of the infrared laser from the resonance
- $\gamma_{31}$  : The decoherence rate between the ground state and the metastable state

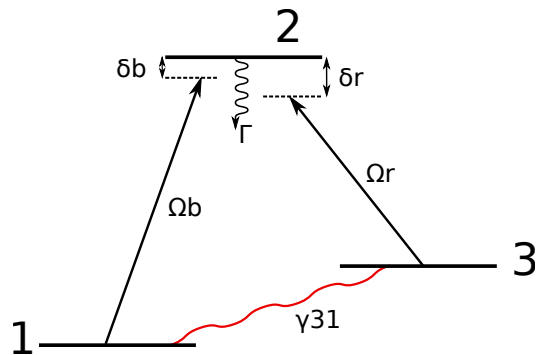


Figure 6.1: The different free parameters of the model and the levels involved. In the case of  $Sr^+$  the levels are 1:  $^5S_{1/2}$ , 2:  $^5P_{1/2}$ , 3:  $^4D_{3/2}$

There are also two fixed parameters: the lifetime of the excited level  $\Gamma$  and the branching ratio from the excited state to the metastable level  $\epsilon$  (for strontium, see section D.2).

Using the following notation :

$$\sigma_{ab} = |a\rangle \langle b|$$

We start from the following Hamiltonian :

$$\frac{H}{\hbar} = E_2 \sigma_{22} + E_3 \sigma_{33} + \Omega_b \cos(\omega_b t) (\sigma_{12} + \sigma_{21}) + \Omega_r \cos(\omega_r t) (\sigma_{32} + \sigma_{23})$$

We go in the rotating frame with the following transformations :

$$\begin{aligned} \sigma_{11} &\rightarrow \sigma_{11} \\ \sigma_{22} &\rightarrow \sigma_{22} \\ \sigma_{33} &\rightarrow \sigma_{33} \\ \sigma_{21} &\rightarrow \sigma_{21} e^{i \frac{E_2}{\hbar} t} \\ \sigma_{13} &\rightarrow \sigma_{13} e^{i(\delta_b - \delta_r)t} e^{i \frac{E_3}{\hbar} t} \\ \sigma_{23} &\rightarrow \sigma_{23} e^{i \frac{E_2 - E_3}{\hbar} t} \end{aligned}$$

We add the decoherence term and the decay from the excited level, taking in account the branching ratio to the metastable state.

And, by adding the equation  $\sigma_{11} + \sigma_{22} + \sigma_{33} = 1$  we obtain an equation matrix which corresponds to the following equation :

$$MSol - Source = 0$$

$$M = \begin{pmatrix} i\Gamma & 0 & \frac{\Omega_b}{2} & -\frac{\Omega_b}{2} & 0 & 0 & \frac{\Omega_r}{2} & -\frac{\Omega_r}{2} \\ -i\Gamma\epsilon & 0 & 0 & 0 & 0 & 0 & -\frac{\Omega_r}{2} & \frac{\Omega_r}{2} \\ \Omega_b & \frac{\Omega_b}{2} & \frac{i\Gamma}{2} - \delta_b & 0 & -\frac{\Omega_r}{2} & 0 & 0 & 0 \\ -\Omega_b & -\frac{\Omega_b}{2} & 0 & \frac{i\Gamma}{2} + \delta_b & 0 & \frac{\Omega_r}{2} & 0 & 0 \\ 0 & 0 & -\frac{\Omega_r}{2} & 0 & i\gamma_{31} - \delta_b + \delta_r & 0 & 0 & \frac{\Omega_b}{2} \\ 0 & 0 & 0 & \frac{\Omega_r}{2} & 0 & i\gamma_{31} + \delta_b - \delta_r & -\frac{\Omega_b}{2} & 0 \\ \frac{\Omega_r}{2} & -\frac{\Omega_r}{2} & 0 & 0 & 0 & -\frac{\Omega_b}{2} & \frac{i\Gamma}{2} - \delta_r & 0 \\ -\frac{\Omega_r}{2} & \frac{\Omega_r}{2} & 0 & 0 & \frac{\Omega_b}{2} & 0 & 0 & \frac{i\Gamma}{2} + \delta_r \end{pmatrix}$$

With the following source term<sup>1</sup>:

$$Source = \begin{pmatrix} 0 \\ 0 \\ \Omega_b/2 \\ -\Omega_b/2 \\ 0 \\ 0 \\ 0 \\ 0 \end{pmatrix}$$

---

<sup>1</sup>Which contains terms only due to the violet laser because this source term is due to the removal of  $\sigma_{11}$  from M

The solution is then obtained by analytically inverting the matrix and multiplying it by the source term.

This model allows us to compute a spectrum that depends on the free parameters. A typical example is shown in Figure 6.2

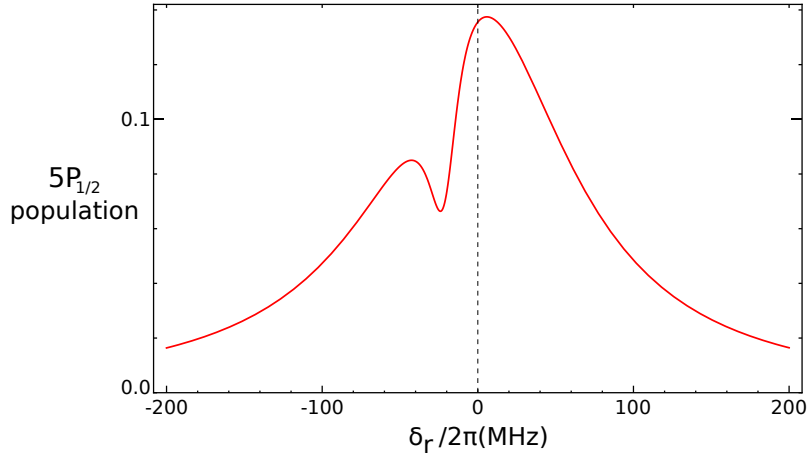


Figure 6.2: Excited state population versus infrared detuning for the following parameters (typical from the experiment):  $\Omega_b = 20 \text{ MHz}$ ,  $\Omega_r = 15 \text{ MHz}$ ,  $\delta_b = -22 \text{ MHz} = -\Gamma$ ,  $\gamma_{31} = 4 \text{ MHz}$   
One can see on the left the two colors dark state which contrast is driven by the  $\gamma_{31}$  decoherence term.

This model is used to guide the choice of the experimental parameters. We have decided to set the Rabi frequencies of both lasers between  $\Gamma$  and  $\Gamma/2$ . A Rabi frequency too important induces a significant amount of power broadening and light shifts. On the contrary if the Rabi frequency is too low, the signal becomes weaker and the signal to noise ratio becomes problematic. Moreover to compensate for radio-frequency heating it is needed to keep a sufficient cooling power.

The other important parameter is the detuning of the violet laser. The dip is stronger when the blue laser is close to resonance but it induces cooling issues for two reasons. First the cooling become less efficient when the cooling laser is too close to the resonance (this issue is discussed in detail in chapter 7), secondly, if the dip is strongly pronounced, effects of EIT cooling [Morigi 00] becomes important. This cooling becomes heating on the other side of the dip. When this effect is low it can affect the shape of the dip, and if it becomes important can melt the coulomb crystal. Finally the compromise chosen is to have a blue laser detuned between  $-2\Gamma$  and  $-3\Gamma$ .

## 6.3 Experimental results and discussion

### 6.3.1 Experimental method

As explained in chapter 5, we can trap the different isotopes of strontium and enrich the ion crystal. The following spectra have been recorded with samples containing equal proportions of the isotopes we want to study. In this way the fluorescence signals from the two isotopes are comparable and the whole sample can be cooled by any of the two isotopes. As we will see this latter property is important. In order to have a significant signal without experiencing significant heating, the samples contain between  $10^3$  and  $10^4$  ions.

The value of the isotopic shifts obtained in the literature are sufficiently precise to set up two beams on the violet cooling laser. The two beams on the infrared repumping laser were adjusted by preliminary isotope shift measurements. Regarding the repumping beams, the acousto optic modulators are tuned in order to have the two beams matching the isotopic shift on the  ${}^4D_{3/2} \rightarrow {}^5P_{1/2}$  transition which is about  $570 - 170 = 400$  MHz.

The spectra are obtained by scanning the frequency of the infrared laser. This scan affects the frequency of the repumping beams for the two isotopes at the same time, thus allowing a direct measurement (knowing their fixed frequency difference imposed by acousto-optic modulators) of the isotopic shift. In order to avoid any crosstalk in the fluorescence measurements for the two isotopes, only one repumper beam among the two is on while measuring the signal. The experimental sequence is detailed on Figure 6.3. This sequence is repeated for each frequency of the main beam.

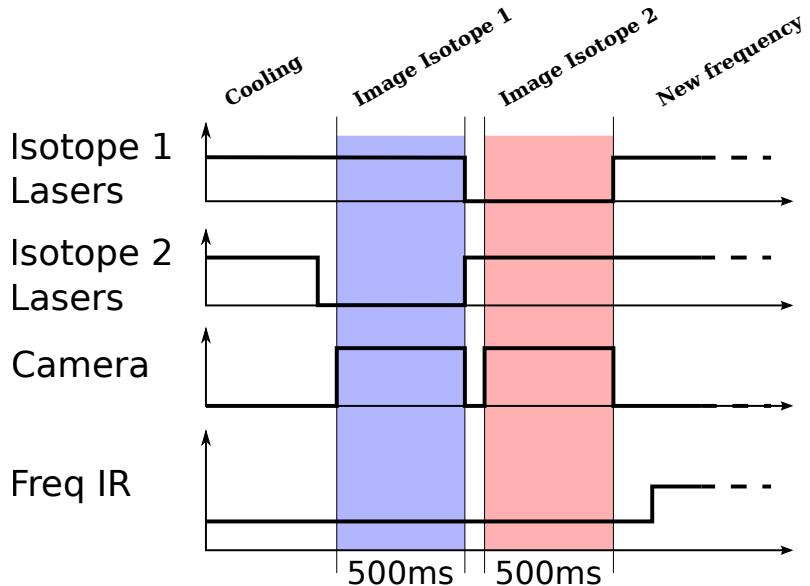


Figure 6.3: Experimental sequence for one point of the spectrum

The fluorescence is collected using a linear response CCD camera (Prosilica model GC1600). In order to reduce the noise due to the scattering of the cooling beam, spatial filtering is used by integrating the signal on a portion of the image.

In order to decrease the number of free parameters the background (coming from the scattering of the cooling laser in the vacuum chamber) is subtracted. The background is recorded just before loading the trap.

The absence of crosstalk is verified by changing significantly the frequency difference between the two repumper beams in order to increase the frequency difference between the maxima of the two spectra. This kind of spectra is visible on the top right corner of Figure 6.4.

Typical spectra for the two isotope couples studied are depicted on Figure 6.4. The three level model described earlier is in good agreement with the experimental data.

When these experiments were performed, technical issues limited the accessible detunings for the cooling lasers on the A=84 isotope and limited the quality of the isotope enrichment. This two issues made the measurement on the A=84 isotope less precise, and the spectra are broader.

The spectra were repeated several times to obtain an evaluation of the statistical error, the results are reported on Table 6.1. The  $\Delta_B$  are relative to the  ${}^5S_{1/2}$  F=2  $\rightarrow$   ${}^6P_{1/2}$  F'=3 transition of  ${}^{85}\text{Rb}$ . The absolute frequency of this transition is 710 962 401 328(40)kHz [Shiner 07]. In order to compute the values of the  $\Delta_B$ , the frequency of the VCO feeding the Accousto Optic Modulator was measured with 50 kHz precision using a spectrum analyser.

Couple A=88,A=86			
$\Delta_B(88)$	$\Delta_B(86)$	$\Delta_{IR}$	spectrum
436.7008	264.8950	398.7891	
437.3348	266.1449	399.5667	
435.9771	265.3589	399.2230	
436.1472	268.0479	400.8431	
436.0026	264.5497	399.7247	
434.1389	271.7871	400.9393	
435.7449	263.5314	399.1390	
437.5951	268.3563	399.3632	a
434.9064	266.5908	399.4741	
436.8074	264.9691	398.7207	
436.7547	265.5945	398.6579	
435.5296	266.3691	400.2444	b

Couple A=86,A=84			
$\Delta_B(86)$	$\Delta_B(84)$	$\Delta_{IR}$	spectrum
264.3423	58.0927	421.3869	c
265.6874	58.5675	421.9029	d
265.0628	58.5790	422.6675	
265.1498	56.2134	424.3034	
264.7437	60.6524	425.1999	
266.2451	58.1086	421.5711	
266.5515	57.9556	422.1257	

Table 6.1: Raw results for the spectra obtained. The analysis of these raw results is depicted on Figure 6.5

The computation of the mean and the standard deviation of these measurements is reported on Figure 6.5.

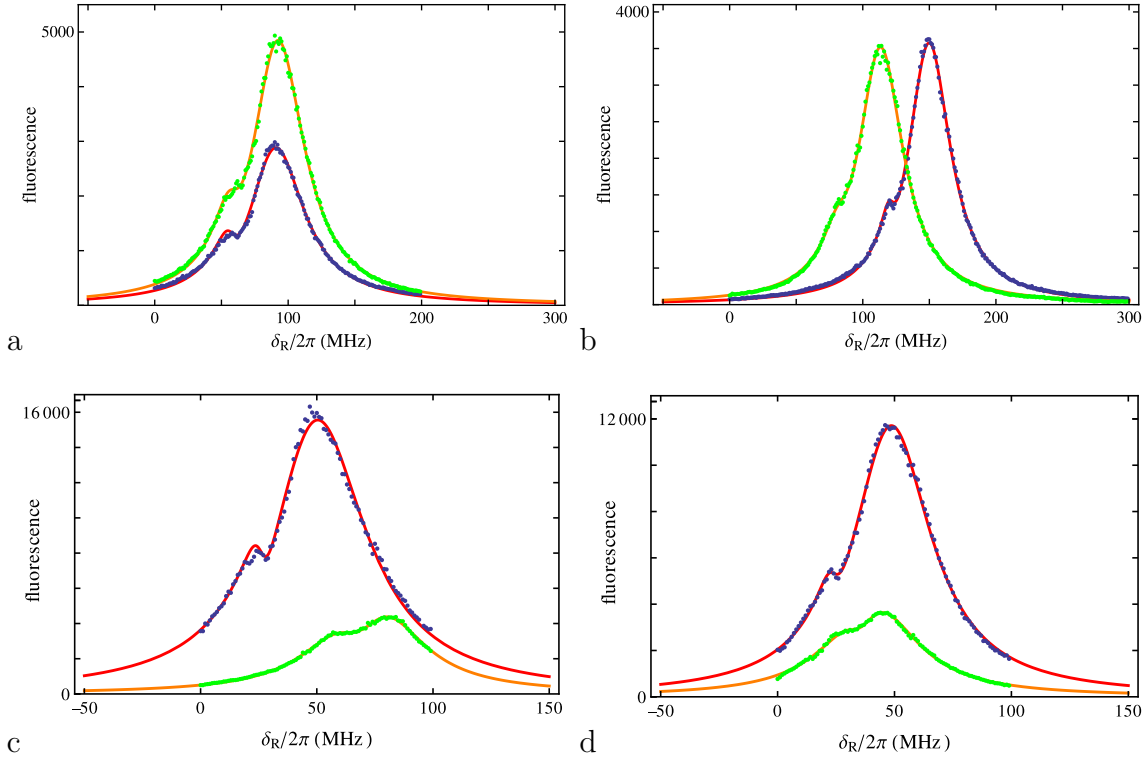


Figure 6.4: Typical experimental fluorescence spectra obtained. Green points : data from the heaviest isotope, Blue points : data from the lightest isotope with their respective fits. Fluorescence intensity differences between isotopes are due to unbalances in the crystal composition and to slight differences in laser intensities.

Top spectra : Spectra on the couple A=88, A=86

The top right spectra was performed to check the absence of crosstalk between the spectra for the two isotopes. The frequency difference between the two repumper beams was adjusted to be significantly different from the isotopic shift thus moving the spectra apart.

Bottom spectra : Spectra on the couple A=86, A=84

For technical reasons (see chapter 5), it was not possible to detune significantly to the red the cooling beam on the A=84. The dip is closer to the resonance. The broadening of the dip is probably due to the high temperature in the crystal.

From the fits we extract the following quantities :  $\Omega_b$ ,  $\Omega_r$ ,  $\delta_b$  and  $\gamma_{31}$  for each isotope, and the difference between the two  $\delta_r$ . These data allows to compute the isotopic shifts on the  $^5P_{1/2} \rightarrow ^4D_{3/2}$  transition and given the detuning of the cooling laser to the locking reference, the absolute frequency of the  $^5S_{1/2} \rightarrow ^5P_{1/2}$  transition. The fit values are reported on Table 6.1.

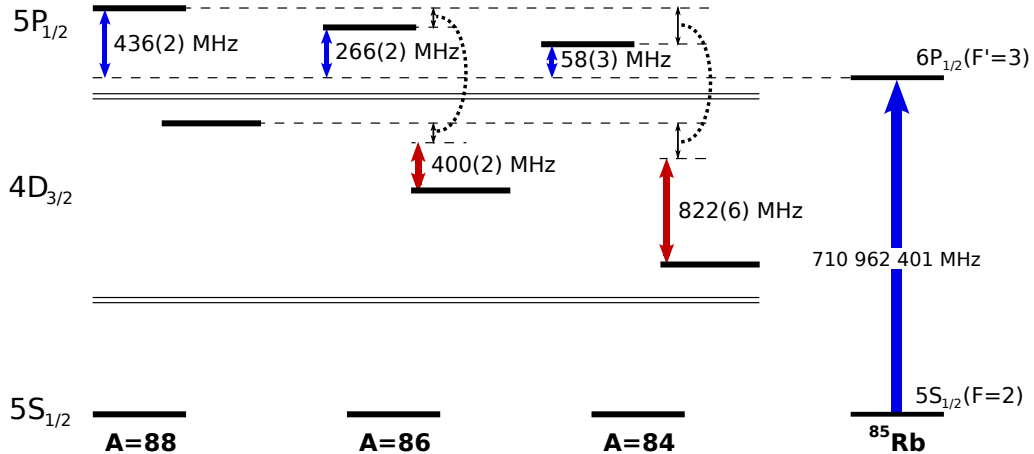


Figure 6.5: Graphical Summary of the isotope shifts measured in the experiment.

The value obtained for the isotopic shift on the  $^5\text{S}_{1/2} \rightarrow ^5\text{P}_{1/2}$  transition were checked with another experiment. Fluorescence spectra were recorded by changing the frequency of the cooling laser while keeping the repumping laser sufficiently detuned to avoid the two photon dark state. This kind of spectra is relatively difficult since the cooling efficiency (or even heating) depends on the detuning of the violet laser. To reduce this problem, the measured isotope may be kept cold via sympathetic cooling of the other isotope. The signal is the difference between an image for which all the lasers are on and an image with the repumper of the probed isotope is off. Nevertheless we were not able to suppress completely the heating problem so these spectra are less precise than the infrared ones. The data obtained are consistent with the data from the infrared spectra. The corresponding spectra are depicted on Figure 6.6.

The intensity of the lasers were monitored during the experiments and the long term fluctuations of the laser's intensities are in good agreement with corresponding fluctuations in the values of the Rabi frequencies extracted from the fit.

## Chapter conclusion

The flexibility given by the isotopic enrichment and the intrinsic properties of cold ion samples allowed us to measure the absolute frequency of the  $^5\text{S}_{1/2} \rightarrow ^5\text{P}_{1/2}$  transition and the isotope shift on the  $^5\text{P}_{1/2} \rightarrow ^4\text{D}_{3/2}$  transition on all the even stable isotopes of singly ionized strontium.

It is possible to improve significantly the precision on the isotope shift of the  $^4\text{D}_{3/2}$  level by addressing directly the  $^5\text{S}_{1/2} \rightarrow ^4\text{D}_{3/2}$  transition.

The precision obtained is one order of magnitude below the linewidth of the transition involved. This measurement opens the way to a better control of isotopic enrichment, sympathetic cooling, and in a general manner to a better control of strontium ion ensembles.

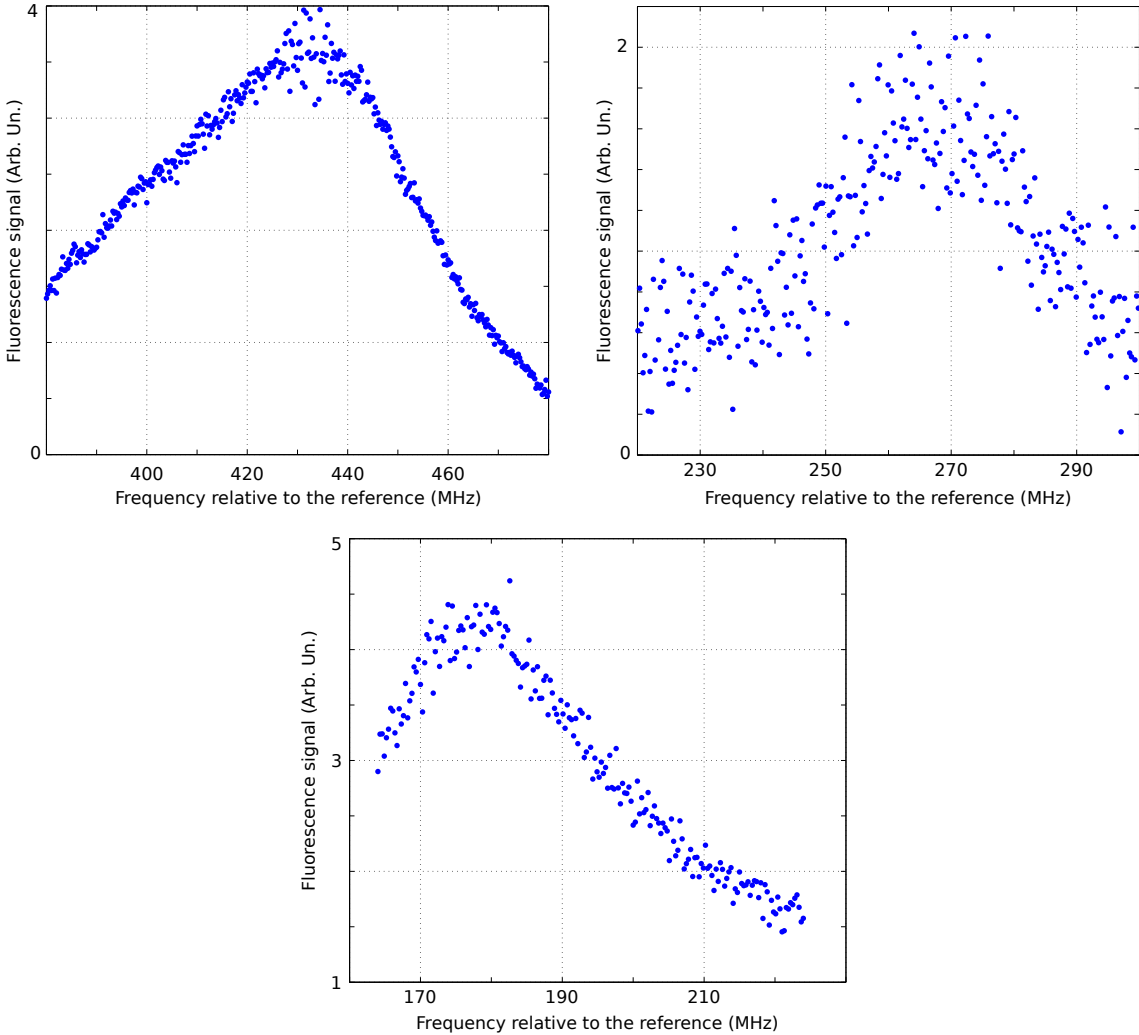


Figure 6.6: Fluorescence spectra versus the frequency of the cooling laser for the  $A=88,86,84$  isotopes in the sympathetic cooling regime

Top left :  $A=88$ . Reference :  $^5S_{1/2} F=2 \rightarrow ^6P_{1/2} F'=3$  transition of  $^{85}\text{Rb}$ . Measured detuning: 430 MHz.

Top right :  $A=86$ . Reference :  $^5S_{1/2} F=2 \rightarrow ^6P_{1/2} F'=3$  transition of  $^{85}\text{Rb}$ . Measured detuning: 265 MHz.

Bottom :  $A=84$ . Reference :  $^5S_{1/2} F=2 \rightarrow ^6P_{1/2} F'=2$  transition of  $^{85}\text{Rb}$  (117.36 MHz lower than the other transition). Measured detuning to the  $^5S_{1/2} F=2 \rightarrow ^6P_{1/2} F'=3$  transition of  $^{85}\text{Rb}$ : 62.6 MHz.

The detunings were measured with a Lorentzian fit of the data, points over 450 MHz were excluded for the  $A=88$  isotope.

# Chapter 7

## Light-matter interaction with a large Coulomb crystal

### 7.1 Introduction

Trapped ions combine several advantages for quantum information processing. They exhibit for example long coherence times [Schmidt-Kaler 03], efficient cooling techniques, interaction between neighboring ions via the bus mode. Unfortunately the achievable optical depths in ion samples are relatively weak due to the usually small ion-number. Several approaches that can increase the light-matter interaction probability are considered in trapped ion ensembles.

The first one consists in the use of high numerical aperture lenses that increases the field concentration at the ion. This approach has shown very promising results allowing for the coupling between single photons and single ions at the quantum level [Piro 11] and the observation of Electromagnetically induced transparency (EIT) on a single ion [Slodička 10]. A similar approach has been used for single atoms trapped in a dipole trap [Tey 08]. This approach is limited by several factors. First, the numerical aperture of the lens cannot be increased indefinitely. Secondly, the lens being generally made of an insulating material, its presence close to the ion can disturb the trap. Finally since the light impinges with a large spread of angles with respect to the quantization axis, the incoming photons are not fully polarized, thus preventing accurate state control and readout.

A second approach, consists in the use of parabolic or spherical mirrors for collecting and focusing the light. Since the mirrors can be metallic, their influence on the ion trap can be taken into account. The use of a mirror allows larger numerical apertures than lenses. New traps are designed with this application in mind [Maiwald 09] and spherical mirrors have been used to reach a collection efficiency up to 25% [Shu 10, Shu 11]. By improving the design it is expected to reach coupling efficiencies of nearly 100% [Sondermann 07]. Unfortunately, complex spatial polarization patterns are needed to reach such high couplings.

Finally cavities can be used to enhance the field at the ion position and increase the interaction between the ion and the light. This approach has been im-

plemented with single ions [Mundt 02, Kreuter 04, Leibrandt 09] and with ion ensembles [Herskind 09]. The ensemble experiments allowed for the realization of the so called collective strong coupling regime, where the losses occurs at a significantly lower rate than the coherent collective interactions mediated by the cavity light field. Optical switching and EIT have also been observed in such system [Albert 11]. The presence of a high finesse cavity around the atomic sample strongly modifies the physics of the system giving rise to a class of new phenomena.

In the perspective of a quantum memory it would be interesting to avoid the use of a cavity, since a high finesse cavity reduces the bandwidth and makes difficult the storage of several spatial modes. The approach used in the ion trap experiment to reach a high light matter interaction probability is similar to the one used with neutral atoms. It consists in trapping an elongated atomic sample to increase the on axis optical depth. This approach should allow to manipulate the collective degrees of freedom of the atomic ensemble and to use them for storing quantum states. The use of trapped ions for this purpose is challenging due to the strong coulomb repulsion. As seen in the previous chapters, experimental efforts have been done to overcome the usual limits of ion traps. In the following the experiments performed for measuring the light matter coupling in a single pass geometry and the problems and limitations of such a strategy will be presented.

## 7.2 Theory

### 7.2.1 Expected absorption

Our system presents several characteristics allowing for a simple calculation of the single pass absorption. The ion density is constant in a Coulomb crystal and the beam waist being relatively large, we can consider a collimated beam for the calculation of the expected absorption, and neglect in first approximation the wave optics aspects of the propagation. For a beam smaller than the ion cloud diameter, the intensity at a distance  $z$  ( $0$  being the edge of the ion cloud) is given by:

$$I(z) = I(0) \cdot \exp(-\sigma \rho_0 z)$$

Where  $\sigma = \frac{\lambda^2}{2\pi}$  is the absorption cross section [Hilborn 82] and  $\rho_0$  is the atomic density.

As described in section 3.1, for the highest radio frequency amplitude used, with the radial frequency measurement we can estimate the ion density to be  $\rho_0 = 3.1 \times 10^{14} \text{ m}^{-3}$ . For the  ${}^5\text{S}_{1/2} \rightarrow {}^5\text{P}_{1/2}$  transition,  $\sigma = 2.8 \times 10^{-14} \text{ m}^2$ . For a typical cloud length of  $l_{cloud} = 10 \text{ mm}$ , we obtain an expected absorption of:

$$A = 1 - e^{-\sigma \rho_0 l_{cloud}} = 8.3\%$$

This model assumes that all the light beam interacts with a two-level atom ensemble. This assumption is valid only when the atoms are prepared into a bright state of the probe polarization. In the case of a linearly polarized probe interacting

with atoms in the ground state of a  $1/2 \rightarrow 1/2$  transition, the probe polarization can be decomposed into two circular polarization states with equal intensities, each of which interacts with half of the population, i.e. an effective atomic density  $\rho_0/2$ . The expected intensity is then  $I'(z) = \sqrt{I(z)}$ . In the case of a low absorption this corresponds to a reduction by a factor two.

### 7.2.2 Temperature effects

The temperature of the sample can be a limitation for the absorption and the coherence time of the ion ensemble.

**Doppler broadening** For a thermal cloud, the Doppler broadening can be modeled by convoluting the line shape with a Gaussian distribution for which the width depends on the temperature. For a temperature  $T$ , the full width at half maximum can be expressed the following way:

$$\Delta f = \sqrt{\frac{8k_b T \ln(2)}{mc^2}} f_0$$

Where  $f_0$  is the transition frequency and  $m$  the ion mass. The relationship between the temperature and the Doppler broadening, in the case of Strontium ions for the  $5S_{1/2} \rightarrow 5P_{1/2}$  transition is represented on the left panel of Figure 7.1.

**Plasma coupling parameter** In order to evaluate the actual temperature regime, it is interesting to estimate the crystallization parameter  $\Gamma_P$  described in subsection 3.1.2 page 23 for different temperatures thus different Doppler broadenings of the transition. This parameter is given by:

$$\Gamma_P = \frac{1}{a_w} \frac{e^2}{4\pi\epsilon_0} \frac{1}{k_b T} \quad (7.1)$$

The variation of  $\Gamma_P$  as a function of the broadenings was computed for the highest density reached in our trap is represented on Figure 7.1. We notice that in the liquid regime  $2 < \Gamma_P < 170$  we can observe significant broadening of the transitions. It have to be remembered that the crystallization bounds on  $\Gamma_P$  was computed for infinite crystals [Slattery 80] and have to be taken with care. In the crystallized regime, this broadening becomes negligible with respect to the natural linewidth of 21.5 MHz.

## 7.3 Absorption measurement method

Absorption spectra have been acquired on the  $5S_{1/2} \rightarrow 5P_{1/2}$  transition. These spectra allows for the measurement of the optical depth of the sample. Depending on the laser parameters (light shift), these spectra may carry useful information allowing us to estimate the temperature range of the sample. In order to ensure a maximal

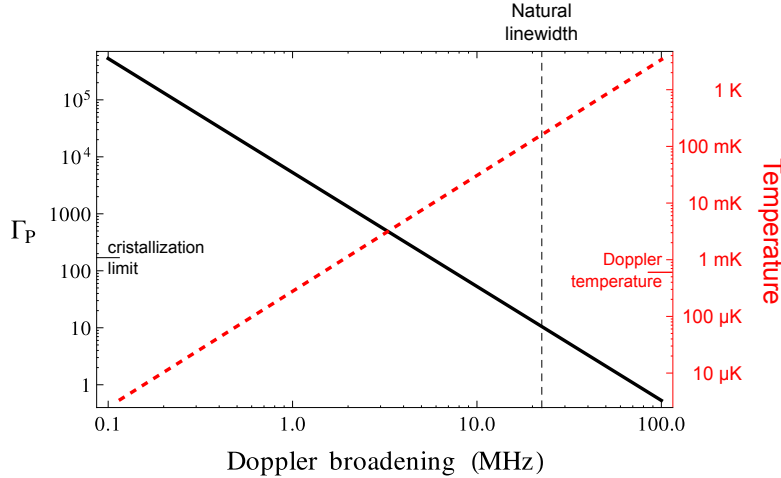


Figure 7.1: (black continuous)  $\Gamma_P$  versus Doppler broadening. The horizontal line corresponds to the limit of crystallization.  
 (red dashed) Temperature versus Doppler broadening.

coupling between the probe beam and the atoms, the probe beam profile has been shaped as described in section 3.7.1 page 37. The alignment of the probe beam is performed by observing the fluorescence signal due to a weak beam propagating in a long ion cloud, the line that separates two different isotopes being used as a reference. This alignment is performed using images taken both from the top and from the side. The experiments described below are performed in the presence of sympathetic cooling from the  $A=88$  isotope, with its cooling laser detuned by  $-2\Gamma$ .

In order to maintain a good precision while reducing the contribution of multiple noise sources, several techniques have been used. Among all the possible noise sources, two of them have a significant contribution to the measured signal: the electronic noise from the photodiode and the light intensity noise.

The first one is reduced by using a low noise operational amplifier for the photodiode transimpedance amplifier. Then, by repeating the measurement sequence a hundred times and averaging the signal, this noise can be reduced down to acceptable levels<sup>1</sup> The light intensity noise can be problematic because of its intensity and its timescale. The typical absorption signal expected is in the order of a few percent whereas the laser intensity can change by more than 10% from shot to shot due to thermal effects in the doubling crystal. In order to reduce significantly the effect of this noise, a background and a signal measurement are performed in a time scale faster than the laser intensity fluctuations. First the atomic population is pumped into a dark state and the probe intensity is measured. Then the ions are transferred quickly into a bright state, affecting the probe intensity. The probe intensity difference is then proportional to the absorption. By using this technique the

<sup>1</sup>photodiode gain:  $1.6 \times 10^5$  V/W, typical signal measured  $\approx 1$  V, RMS noise after averaging  $\approx 5$  mV

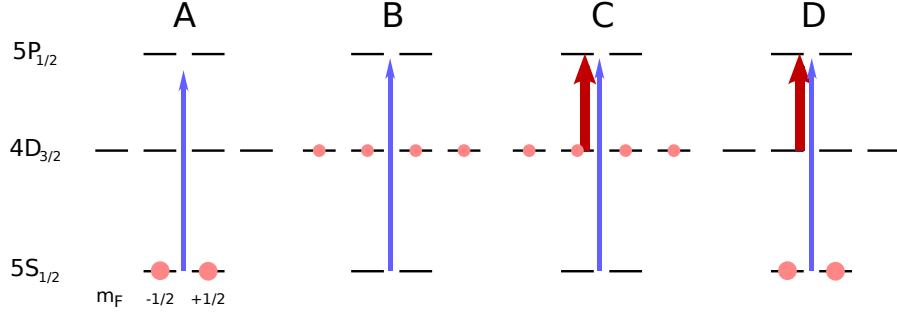


Figure 7.2: Experimental sequence used to prepare and probe the atomic system. During the whole sequence the probe beam is kept at low power and vertically polarized, the cooling beam for the  $A=88$  isotope is kept on.

A: The atoms are pumped into the metastable level. B: The repumpers are switched off during 1 ms, then the probe beam frequency is adjusted. C: The repumper is switched back on. The population is quickly pumped into the ground level with a characteristic time  $< 10 \mu\text{s}$ . D: In steady state we can measure the decrease of the probe power due to the atoms in the ground level.

laser intensity noise affects the signal, in first approximation, proportionally to the measured absorption contrary to other simpler approaches where the laser intensity noise translates directly in the measured signal.

The experimental sequence used for measuring the absorption with linear polarization is depicted on Figure 7.2.

The measured signal can be superimposed with significant electronic ripple synchronized with the experimental sequence. The exact origin of these fluctuations is not fully understood<sup>2</sup> but a background signal can be subtracted from the main signal to get rid of these fluctuations. This background signal is acquired by executing an identical sequence and blocking the repumper of the  $A=86$  isotope with a mechanical shutter. Typical signals obtained using this technique and the above-mentioned experimental sequence are displayed on the top panel of Figure 7.3.

On the bottom panel of Figure 7.3 is represented the averaged signal  $V_m(t)$  used for the data analysis which is obtained in the following way:

$$V_m(t) = \langle V_{p1}(t) - V_{p2}(t) \rangle_{20 \text{ samples}}$$

Where  $V_{p1}(t)$  (resp.  $V_{p2}(t)$ ) represents the photodiode signal when the repumper is not blocked (resp. blocked) and  $\langle \dots \rangle_{n \text{ samples}}$  represents a moving average over  $n$  samples.

The absorption signal is then evaluated using the amplitude of the signal step:

$$Abs(f) = \frac{\langle V_m(t) \rangle_{t \in [10 \mu\text{s}, 40 \mu\text{s}]} - \langle V_m(t) \rangle_{t \in [-30 \mu\text{s}, 0 \mu\text{s}]}}{\langle V_{p1}(t) \rangle_{t \in [-30 \mu\text{s}, 0 \mu\text{s}]}}$$

---

<sup>2</sup>One possible source is ground loops involving the high-voltage of the EOM

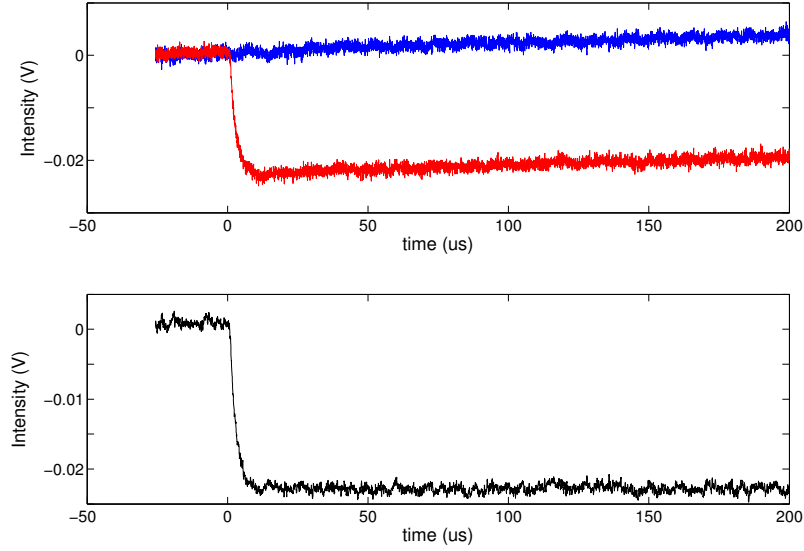


Figure 7.3: Typical absorption signal obtained at a given probe detuning (offset subtracted). Top: Photodiode signals. Blue (top):  $V_{p1}(t)$ , red (bottom)  $V_{p2}(t)$ . Bottom: difference signal used for analysis (see text for details).

This procedure allows us to obtain a quantitative estimation of the optical depth with a good signal to noise ratio.

### 7.3.1 Absorption spectra with linearly polarized probe

A spectrum obtained with this technique is represented on Figure 7.4. This spectrum is obtained with an ion density of  $2 \times 10^{14} \text{ m}^{-3}$  in a cloud containing more than 1 million of ions<sup>3</sup>. The horizontal axis is normalized in units of the natural linewidth of the excited level. The resonant absorption is 1.6%. The simple model described earlier predicts an absorption of 2.8 in these conditions.

The measured spectra are significantly broader than the natural linewidth. This excess width is a possible explanation for the lower absorption observed. Reducing the intensity of the probe (by a factor 2) and of the repumper (by a factor 10) did not allow to measure significant changes in the width of the spectra, combined with the fact that the probe intensity is well below the saturation intensity ( $\approx 1\% I_{sat}$ ), power broadening is not a good candidate to explain the width of the observed spectra. The best candidate is then a thermal broadening. The red line on Figure 7.4 is a fit of the measured spectra by a Voigt profile giving a full width at half maximum for the convoluted Gaussian of 45 MHz ( $2.1\Gamma$ ). It would correspond to a temperature of 0.5 K. Assuming a broadening only due to temperature, we can compute the corresponding plasma coupling parameter  $\Gamma_P$  (Equation 7.1) with the ion density. We obtain  $\Gamma_P \approx 3$ , this is compatible with a sample which is between the liquid and the crystalline state.

---

<sup>3</sup>counting all the isotopes

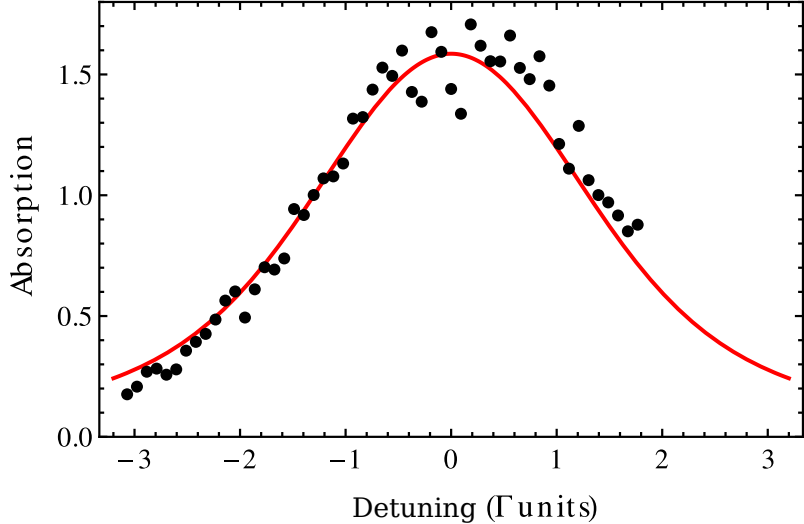


Figure 7.4: Spectrum obtained with a linear probe and a cloud density of  $2 \times 10^{14} \text{ m}^{-3}$ . Black dots: experimental data. Red continuous line: fit with a Voigt profile.

### 7.3.2 Large spectra and model for longitudinal oscillation

The shape of the absorption spectra depends on the experimental conditions, in particular the axis of the sympathetic cooling laser. When the cooling laser is along the trap axis or when sympathetic cooling is not used during the probing phase, the shape of the spectra is modified. This modification can be interpreted as a longitudinal motion of the ion cloud. However, the mechanism explaining this motion and why it is not efficiently laser cooled is not understood yet.

The spectrum represented on Figure 7.5 has been recorded with the axis of the sympathetic cooling beam aligned along the trap axis.

This spectral shape could be interpreted as the result of a collective harmonic oscillation of the ions along the trap axis. For a harmonic motion the velocity probability distribution can be evaluated

$$P_v(v) = \frac{1}{v_{MAX}\pi\sqrt{1-v^2/v_{MAX}^2}}$$

This probability distribution is plotted on Figure 7.6

By convolving this probability distribution with a Voigt distribution we compute the expected spectra. This model can be used to fit the experimental data. The result is the black dashed line of Figure 7.5 from which we obtain  $v_{MAX} = 12 \text{ m s}^{-1}$  which corresponds to an amplitude of motion of  $\approx 90 \mu\text{m}$  for a trap longitudinal frequency of 20 kHz, and a Gaussian FWHM of 16 MHz. Such an effect have been observed with single Barium ions in a hot regime [Schubert 89].

This model does not take into account the anharmonicities of the axial trapping potential. As shown in Figure 5.4 page 59 the axial trapping potential is “flat” at

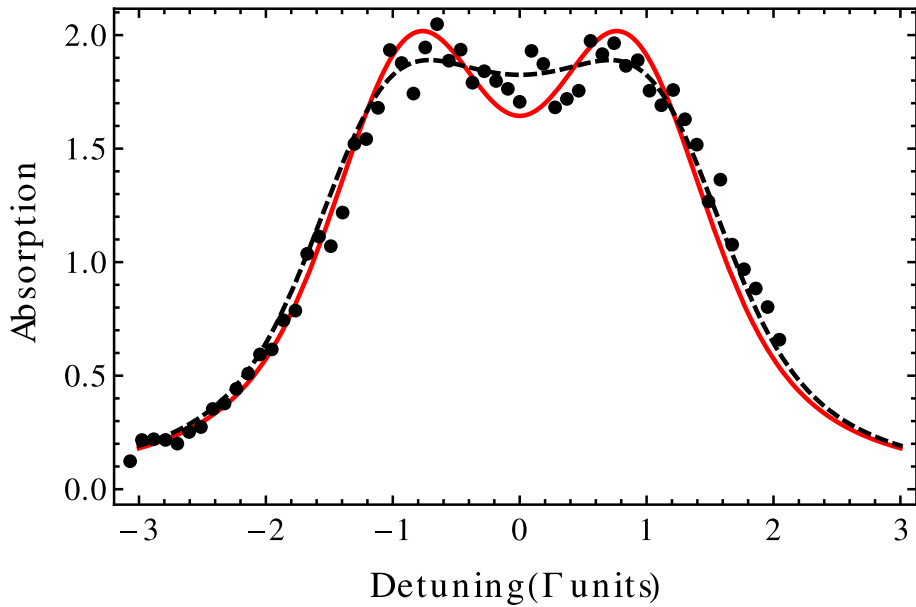


Figure 7.5: Absorption spectra obtained with the laser cooling on axis. The shape of the spectra could be explained by a harmonic oscillation along the trap axis. Black dashed line: harmonic motion fit. Red continuous line: two speed motion fit (see text for details).

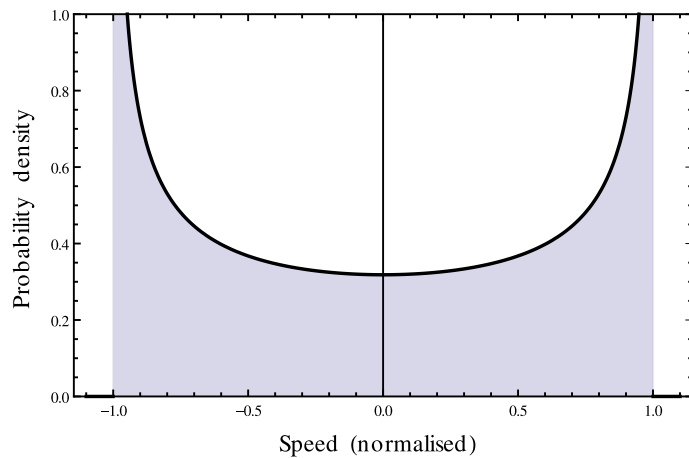


Figure 7.6: Velocity probability density for an harmonic motion. The maximum speed is normalized to 1.

the bottom and very steep at the edges. The velocity probability distribution of a particle in this kind of potential mostly consists in two peaks at speeds  $+v$  and  $-v$ . If we approximate the longitudinal motion by two opposite speed classes plus some thermal broadening, we can model the measured spectrum with a sum of two shifted Voigt profiles. Fitting the data with this simplified model, the red continuous line of Figure 7.5 is obtained. The fit results are a velocity  $v_{MAX} = 7.6 \text{ m s}^{-1}$  and a full width at half maximum for the convoluted Gaussian of 20 MHz ( $0.9\Gamma$ ,  $T \approx 0.1K$ ).

The real motion is probably an intermediate between these two models. These models despite their simplicity give a good interpretation of the shape of the observed spectra even if the underlying mechanism giving rise to this motion is not yet understood.

## 7.4 Evidence for EIT in ion cloud and spectra with circular polarization

The goal of this experiment is to evaluate the possibility of using large ion ensembles for quantum information tasks, in particular quantum memories. In this perspective, several questions need to be addressed, in particular the possibilities of control of the collective atomic state and the level of coupling between light and matter that can be reached. Optical pumping and single pass probe absorption experiments have been performed. Significant absorption levels have been measured, and preliminary data on electromagnetically induced transparency have been obtained. The data show an EIT signature in an large coulomb crystal. But all the features contained in these data are not yet fully understood.

### 7.4.1 Optical pumping

As presented in section 3.7.1 page 39, the polarization of the probe beam is controlled by an electro optic phase modulator (EOM) and a set of waveplates. The quality of the polarization and the calibration of the electro optic modulator can be verified by measuring the fluorescence signal versus the voltage applied to the electro optic modulator. With a magnetic field and the light propagation direction aligned along the trap axis. We expect a fluorescence extinction due to optical pumping when the probe polarization is circular and a fluorescence maximum for a linear polarization. The measurement (performed with a guiding field along the cloud axis of 0.3 G) and a fit with a rate equation model is presented on Figure 7.7. An extinction of more than 90% is observed. The extinction can be limited by several factors, in our case two factors are suspected to contribute significantly: imperfect magnetic field direction and improper light polarization.

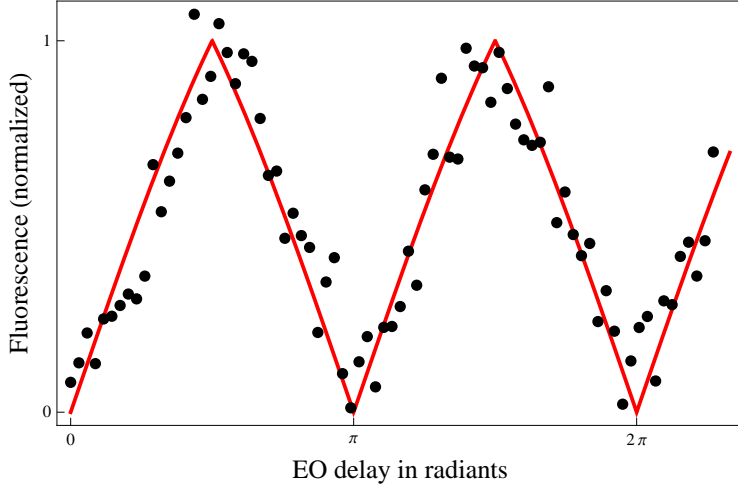


Figure 7.7: Fluorescence of an ion cloud versus electro optic voltage. Data are obtained the cooling laser detuned by  $-3\Gamma$  and with an intensity significantly lower than the saturation intensity. Red line: model from rate equations. The measured  $\Pi$  voltage is  $V_\pi = 859$  V

### 7.4.2 Electromagnetically Induced Transparency

The experimental sequence used for this experiment is presented on Figure 7.8: the ions are first prepared in one of the ground state Zeeman sublevels by a circularly polarized pump beam, then probed with an opposite polarization. This technique allows us to study the transmission of the probe both in the presence and in the absence of a repumper during the phase "D" of Figure 7.8. In this latter case the spectrum of the transient response is expected to display a simple two-level atom ensemble lineshape.

A typical transient absorption signal obtained with the experimental sequence of Figure 7.8 is presented on Figure 7.9 (b): we notice two absorption peaks that are washed out by the optical pumping in a characteristic time of 20  $\mu$ s. The height of the peaks is measured the following way:

$$Abs(f) = \frac{\langle V_m(t) \rangle_{t \in [200 \text{ us}, 220 \text{ us}]} - \min(V_m(t))_{t \in [220 \text{ us}, 240 \text{ us}]}}{\langle V_{p1}(t) \rangle_{t \in [200 \text{ us}, 220 \text{ us}]}}$$

On Figure 7.10, absorption spectra obtained in various configurations are presented. The shape of the spectrum without repumper could be explained by a combination of thermal effects and longitudinal oscillation as previously discussed in subsection 7.3.2 page 79.

A decrease of the absorption is observed around  $-20$  MHz when the repumping laser is switched on during the probing phase (large arrow on Figure 7.10). This dip can be interpreted as a manifestation of EIT in a large ion cloud. Here the repumper laser plays the role of the control laser and the violet laser is the signal. This interpretation is also consistent with the fact that the frequency at which this

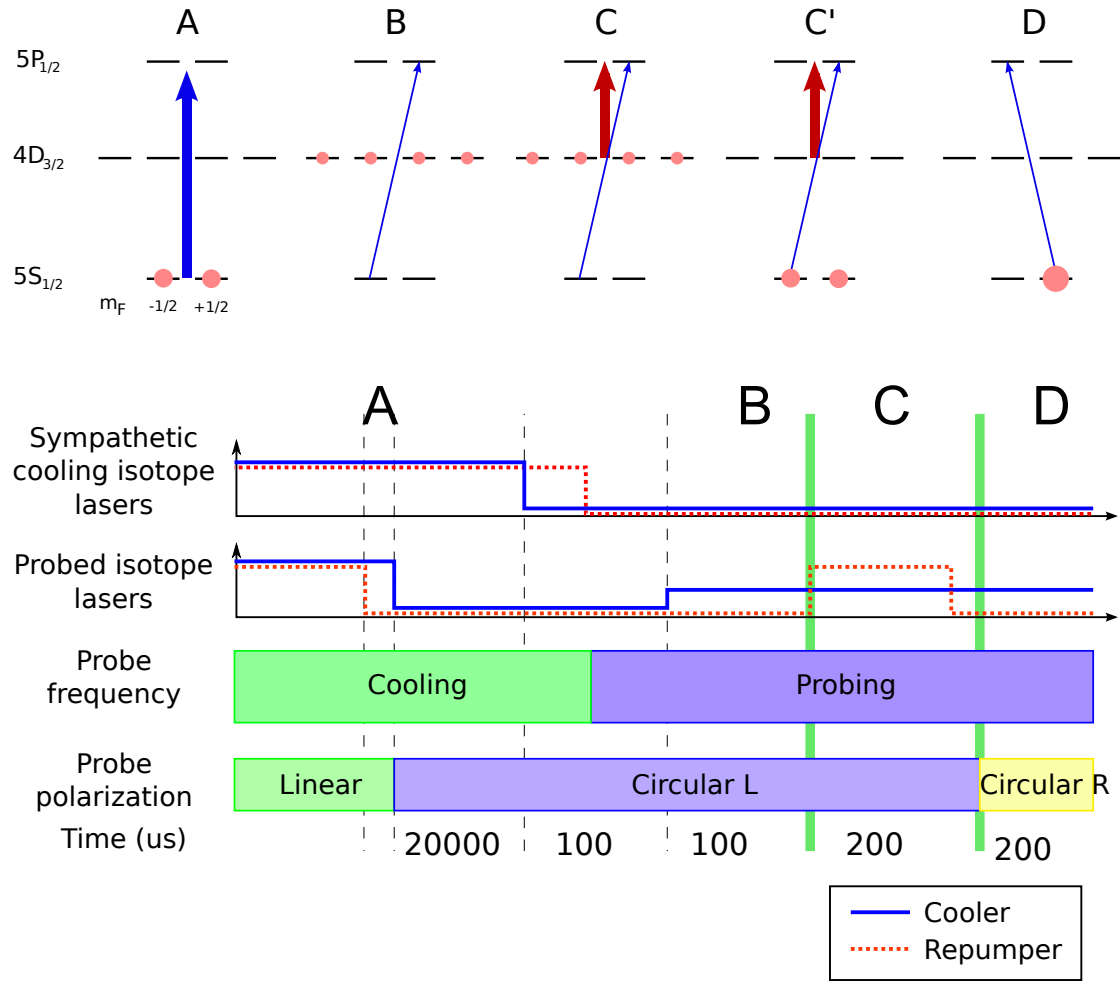


Figure 7.8: Experimental sequence used to prepare and probe the atomic system. A: The atoms are pumped to the metastable level. B: The repumper is switched off, then the probe beam frequency, polarization and power are adjusted, letting time for the photodiode transient to relax (millisecond timescale). C: The repumper is switched back on. The population is quickly (in less than 1  $\mu$ s) pumped into the ground level. Immediately after (C'), we observe a decrease of the probe power due to the atoms sent back to the  $m_F = -1/2$  ground sublevel, then the probe progressively pump the atoms into the  $m_F = +1/2$  ground sublevel. D: The polarization of the probe is switched to measure the absorption from the atoms in the  $m_F = +1/2$  sublevel. The repumper can be switched on or off during this phase in order to isolate the specific features due to the 3-level scheme.

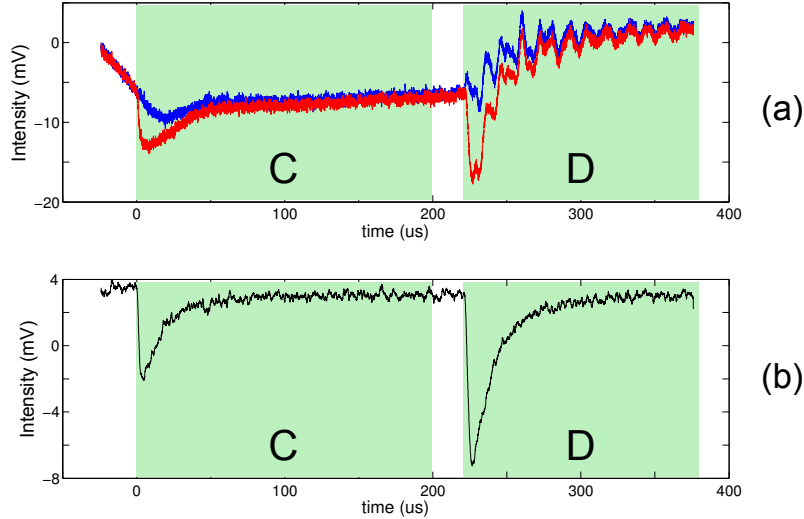


Figure 7.9: (a) Typical raw data signal for the transient absorption experiment described in Figure 7.8. Blue (top):  $V_{p1}(t)$ , red (bottom)  $V_{p2}(t)$  (the conventions are the same previously introduced in Figure 7.3. (b) processed signal used for analysis (see text for details). The phases A and B are performed before  $T=0$ . Phase C starts at  $T=0$ . Phase E starts at  $T=225\ \mu s$ .

dip occurs is related to the frequency detuning of the repumper (control) beam, as can be noticed on Figure 7.10. Let us notice the presence of other dips (marked with small arrows on Figure 7.10) in the spectra which needs further investigations to be completely understood. They could be linked with a special velocity distribution of the ions, however we lack information to confirm or infirm this hypothesis, in particular measurements of the ion temperature and their residual motion.

## 7.5 Preliminary experiments on RF heating in large samples

The amount of light-matter coupling is probably limited by some residual motion of the ions. In order to explore this hypothesis, a preliminary study of the influence of the cooling parameters on the observed absorption has been performed. However, no simple trend for significant improvement of the coupling has been found. A quantitative and detailed study needs to be performed, in particular with a quantitative measurement of the sample temperature. In order to understand if the source of broadening is the radio frequency heating, we have performed other preliminary experiments for studying radio frequency heating in large coulomb crystals. The ion crystal used for the experiments having a radial size comparable with the trap characteristic dimensions, radiofrequency heating can indeed play an important role in the observed temperature.

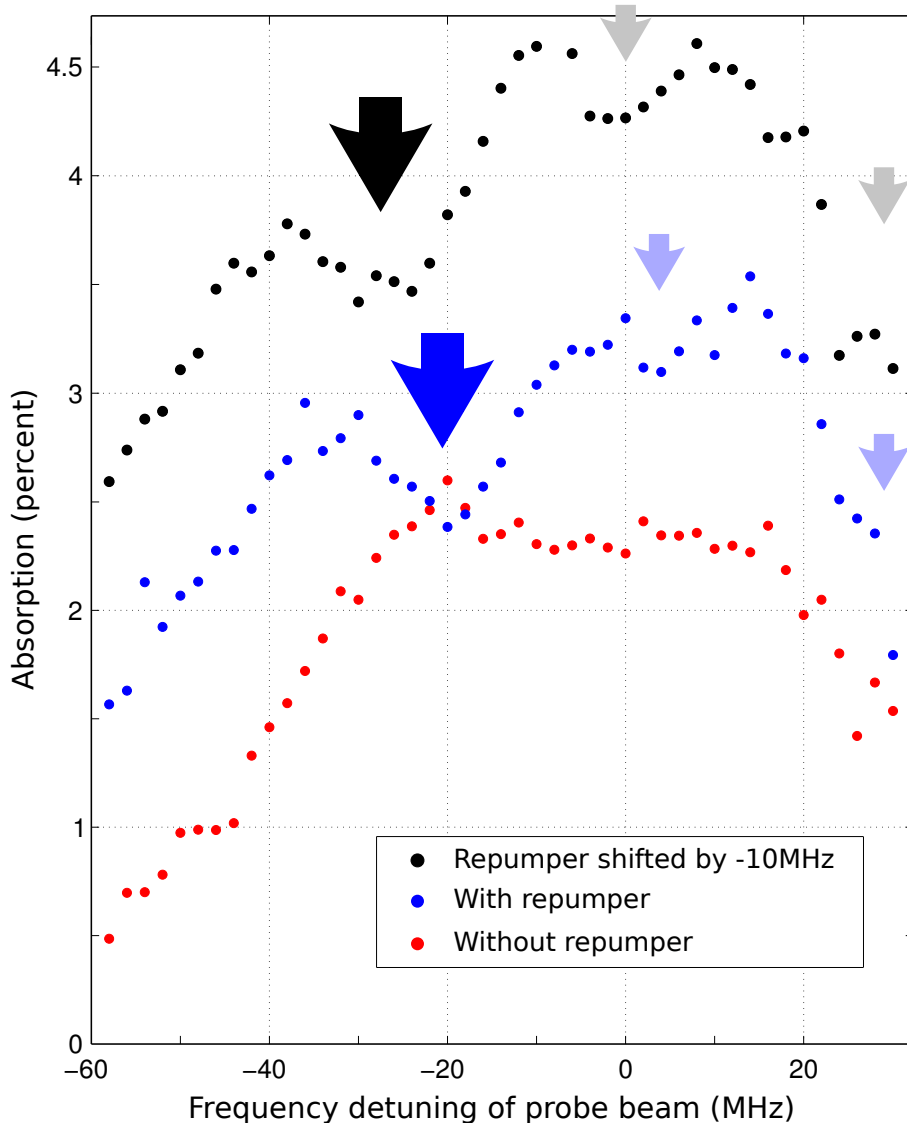


Figure 7.10: Signature of Electromagnetically Induced Transparency in a large Coulomb crystal. Experiment performed with a guiding magnetic field of  $\approx 3\text{ G}$ . Red, bottom : spectrum without repumper during the probing phase. Blue, middle : spectrum obtained in the presence of a repumper (Curve shifted by 1% for clarity). Black,top : spectrum obtained in the presence of a repumper being shifted by  $-10\text{ MHz}$  with respect to previous scan (Curve shifted by 2% for clarity). The dips induced by the repumper are marked with arrows.

### 7.5.1 Temperature from image analysis

The temperature of an ion cloud can be estimated with high resolution image. However, in order to obtain quantitative information, a method is to compare images with many-body simulations[Ostendorf 06]. Given the number of ions in our trap, this kind of simulations is computationally extensive. The following study is based on a qualitative observation of the contrast between ion layers at the edge of the ion cloud using high resolution images. This study allowed to observe the influence of several cooling parameters, unfortunately no significant improvement could be obtained.

In order to have some clues about the temperature of the ion cloud, high resolution images of the ion crystal have been taken. A picture of a cloud containing  $\approx 0.5 \times 10^6$  ions with an estimated density of  $2 \times 10^{14} \text{ m}^{-3}$  is represented on Figure 7.11.

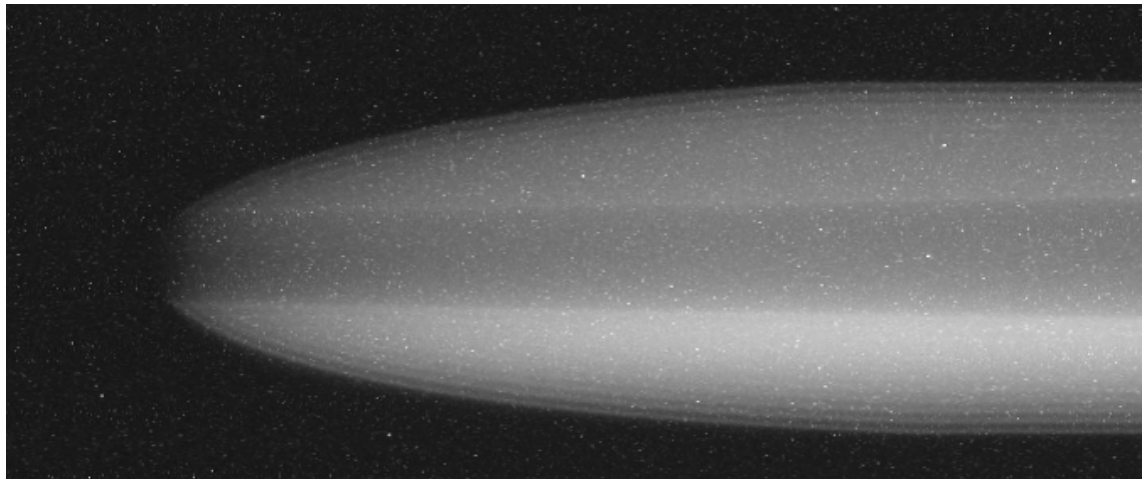


Figure 7.11: High resolution image of a cloud containing  $\approx 0.5 \times 10^6$  ions. The cooling laser on the  $A=88$  isotope is detuned by  $-2\Gamma$ . 2D ion arrangement is visible on the edge of the ion cloud. See text for details.

A 3D order cannot be distinguished whereas a clear 2D radial order exists. This phenomenon has been observed in [Drewsen 98] and indicates that the cloud is between the liquid and crystalline state. Given the result of Figure 7.1 page 76, this observation, even though not precise is consistent with the observed broadening.

The effect on the temperature of the number of ions has been observed by imaging clouds containing two millions and half a million ions at a density of  $3.1 \times 10^{14} \text{ m}^{-3}$ . On Figure 7.12 the images obtained are represented. We notice a clear blurring of the crystalline layers for the highest ion number even at the edges of the sample. This supports the hypothesis of an increased temperature for larger ion numbers.

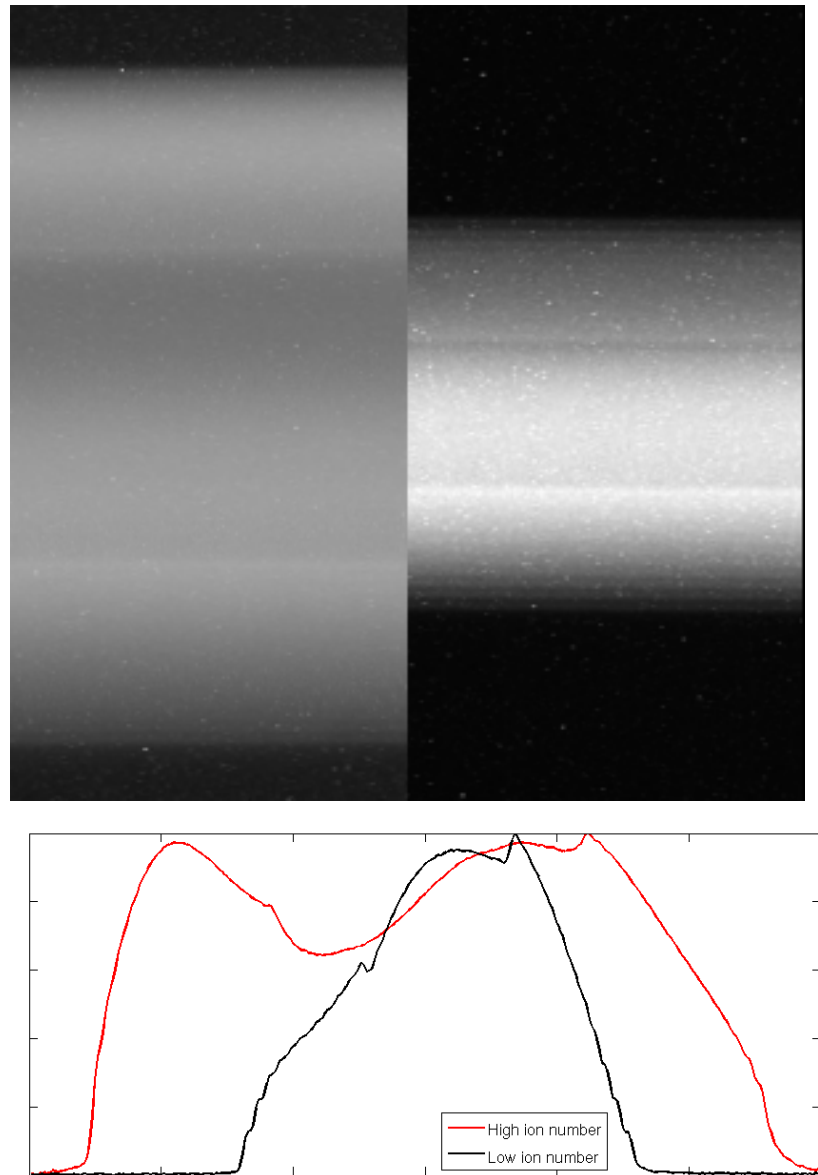


Figure 7.12: Top: Images for different ion number at a density  $3.1 \times 10^{14} \text{ m}^{-3}$ . Cooling laser on the  $A=88$  isotope detuned by  $-2\Gamma$ .  
Left: cloud containing  $2.2 \times 10^6$  ions. Right: cloud containing  $0.5 \times 10^6$  ions  
Bottom: radial intensity cut

### 7.5.2 Absorption versus ion number

The effect of the radiofrequency heating has also been measured on the on-resonance absorption. Starting with an empty trap, the absorption have been measured every minute during the continuous loading with a linearly polarized probe on resonance with the technique described in section 7.3 page 75. The result of the measurement is depicted on Figure 7.13.

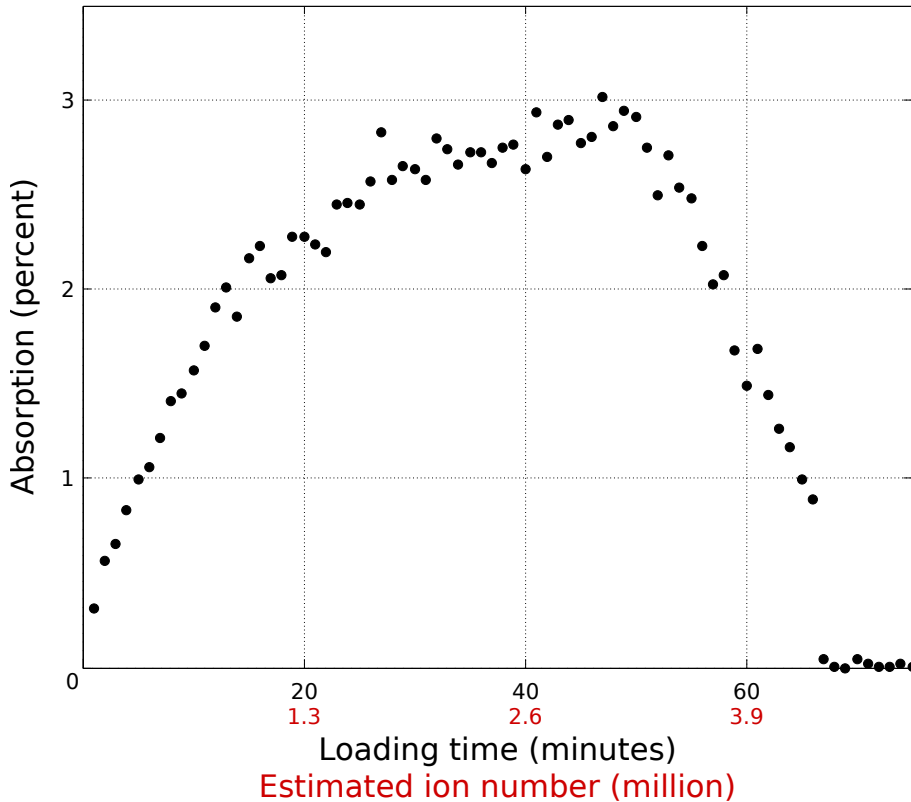


Figure 7.13: Absorption on resonance versus the ion-number in the trap (ion number estimated with the loading rate). Four phases can be identified: A first phase where the ion cloud is radially smaller than the beam cross-section and the absorption increases significantly with the number of ions. A second phase where the cloud has a size comparable to the beam cross section where the absorption increases slowly due to the increasing ion cloud length (and a possible slight misalignment of the probe). A third phase, where the absorption drops significantly, which can be understood as an increase of cloud temperature from radio-frequency heating that affects the peripheral ions. Then more drastic absorption drop is noticed, the observation of the cloud images show a simultaneous loss of the "dense" phase. This phenomenon can be interpreted by an insufficient cooling to keep the dense phase cold enough.

This experiment confirms the importance of the radio frequency heating in the regime of very large coulomb crystals ( $N > 1 \times 10^6$ ). This radiofrequency heating

can be due to different factors such as an improper trap working point ( $a$  and  $q$  trapping parameters), an imperfect compensation of the stray fields, some geometrical imperfections that become critical in this trapping regime.

For large clouds, the effect of the stray field compensation is expected to be relatively small, the displacement of the ion cloud during the compensation procedure being significantly smaller than its size. Therefore the effect of the excess radiofrequency heating from imperfect compensation should be significantly lower than the total radiofrequency heating experienced by the ion cloud.

Radiofrequency heating has not yet been studied in such large coulomb crystals. As in the case of smaller crystals, the trapping regime, in particular the  $q$  parameter, are expected to play an important role. The  $q$  parameter can be lowered by using lighter ions, reducing the distance between the electrodes and increasing the radiofrequency amplitude. In order to keep the ion density constant the RF frequency has to be increased by the same amount as the reduction of the  $q$  parameter. A decrease of the  $q$  factor by a factor of 4 by reducing the trap size by a factor of two, will lead to a RF frequency of 30 MHz which is a difficult but achievable goal.

## Chapter conclusion

We have measured an unprecedented level of coupling between light and a coulomb crystal in free space (up to 3% with linear probe polarization) and observed EIT in a large Coulomb crystal.

The light-matter coupling is probably currently limited by some residual motional effects and by the temperature of the sample. Temperature measurement, associated with a study of the dependence of the heating rate versus the trapping parameters would allow for a better understanding of these phenomena and could allow for an improvement of the trap design. Several factors could affect the sample temperature, in particular the  $q$  parameter, the stray fields, the trap defects and the isotopic proportion are expected to play an important role. The reason why a longitudinal oscillation would not be efficiently damped by laser and sympathetic cooling still has to be understood.

The transition between the different even isotopes of  $\text{Sr}^+$  are too close to completely neglect the off-resonance excitation of the “dark” isotope by the cooling laser. This phenomenon can be reduced by using a spatial filter or by using a the  $A=87$  isotope, the hyperfine structure of which provides GHz of level splitting. In this perspective, more direct and more precise temperature measurements will be useful. These measurements can be based on the spectroscopy of the narrow  $5S_{1/2} \rightarrow 4D_{3/2}$  transition or narrow Raman transitions. Combined with imaging and electron shelving, these methods could allow to obtain spatial information about the sample temperature.

Another perspective to improve the coupling is to use the  $4D_{3/2} \rightarrow 5P_{1/2}$  (or  $4D_{3/2} \rightarrow 5P_{3/2}$ ) transition as a storage transition. This transition has a frequency of 274 589.4 GHz. Due to the difference in wavelength with the  $5S_{1/2} \rightarrow 5P_{1/2}$ , the interaction cross section is larger by a factor 6.7. Moreover, for technical reasons,

it is significantly easier to produce and carry non classical states with near infrared wavelengths compared to blue-violet wavelength. Let us remark however that, a  $3/2 \rightarrow 1/2$  (or  $3/2 \rightarrow 3/2$ ) transition is more complicated than a  $1/2 \rightarrow 1/2$ . This approach will be also limited by the finite lifetime of the  $4D_{3/2}$  level (395 ms).

Finally, light-matter coupling can be enhanced by the use of a low finesse cavity allowing for high signal bandwidth and significant optical depth. But, in the perspective of quantum memory experiments, the sympathetic cooling has to be improved and heat sources have to be understood and reduced.

## **Part II**

# **Detection of non-Gaussian states in atomic ensembles**



## Research context

This part of the thesis has been done in the group of Morgan W. Mitchell at the Institute of Photonic Sciences (ICFO - Castelldefels (Barcelona) - Spain). The Institut de Ciències Fotòniques (ICFO) is an independent, non-profit, permanent research center established by the Generalitat de Catalunya (Government of Catalonia, Spain), Ministry of Economy and Knowledge, and by the Universitat Politècnica de Catalunya.

The group is aimed on the experimental quantum manipulation of light and atomic ensembles, in particular the study of quantum metrology i.e. how a quantum state can improve the ultimate precision of a measurements. This research is performed on two experiments: a quantum light experiment, and a cold atom experiment.

The non-classical light experiments are designed to produce non classical states of light for the interaction with atomic ensembles of rubidium. The state are produced with optical parametric oscillators, filtered by an "interaction free" atomic filter [Cerè 09], and depending on the experimental conditions, produces polarization NOON states [Wolfgramm 10b] of photon pairs or polarization squeezed light [Wolfgramm 10a]. A NOON state is a maximally entangled state, resource for quantum information and quantum metrology measurements. Heralded single ( $g^2 = 0.04 \pm 0.012$ ) photons are also produced [Wolfgramm 11] resonant with atomic transitions, with a linewidth (7 MHz) fitted to the atomic transition lifetime. These photons are a direct resource for quantum information and quantum networking experiments. In a different experimental regime, polarization squeezed light is produced, allowing to beat the standard quantum limit (thus improving precision) in magnetometry experiments.

The other experiment, with which this work has been done, is designed to manipulate and measure the collective spin state of a cold (25  $\mu\text{K}$ )  $^{87}\text{Rb}$  atomic ensemble. The atomic state is measured using Quantum non-demolition measurements (QND), via the Faraday rotation induced by the atoms on light pulses spatially matched with the atomic ensemble. This technique is commonly used for generation and measurement of non-classical states in atomic spin ensembles [Appel 09a, Koschorreck 10a] and nano-mechanical oscillators [Hertzberg 10]. The measurement noise is significantly lower than the atomic shot noise [Koschorreck 10b] and the state demolition is sufficiently low to obtain measurement induced spin squeezing [Koschorreck 10c]. This spin squeezed state is a "macroscopically" entangled state, interesting on a fundamental level, and also a resource for quantum magnetometry. For a QND measurement, the a compromise have to be found between the signal and the state demolition, the light intensity levels and detunings are chosen to provide linear, non destructive measurements. But this setup allowed to explore another regime of the light matter interaction. The light detunings can be chosen to emphasize the non linear interaction, still having access to the very sensitive linear measurement. This regime allowed to demonstrate that non linear measurements have a better signal to noise scaling than linear measurements called super Heisenberg scaling

[Napolitano 11].

This experimental apparatus, have been used in the context of this thesis, for measuring non Gaussian atomic states [Dubost 12]. In particular study the noise properties of an approached based on the use of cumulants which are statistical tools well adapted to the measure of non gaussianity of a distribution. In the following chapters, the theory, the measurement method and the results will be presented.

# Chapter 8

## Detection of non-Gaussian states in atomic ensembles

### 8.1 Introduction

#### 8.1.1 Non-Gaussian states

Non-Gaussian states, for which the Wigner distribution differs from a Gaussian distribution, are an essential requirement for universal quantum computation [Ralph 03, Lloyd 99] and several quantum communication tasks with continuous variables, including improving the fidelity of quantum teleportation [Dell'Anno 07] and entanglement distillation [Eisert 02, Giedke 02].

The state obtained after the subtraction of a photon from a squeezed vacuum or a Fock state is very similar to a superposition of small coherent states (so-called Schrödinger Kitten) having many interesting properties. It can be used as a resource for several quantum information protocols and is a perfect candidate state for the study of decoherence. This kind of state has been produced experimentally by several groups using conditional preparation [Neergaard-Nielsen 06, Ourjoumtsev 06, Ourjoumtsev 07, Wakui 07, Takahashi 08]. The non-Gaussian character of a single photon state have also been verified [Ježek 11].

In atomic systems, proposals are being actively pursued. These proposals are based on large spin squeezing associated with a QND measurement [Massar 03], cavities and conditionnal preparation using homodyne detection [Nielsen 09], storage of optical non Gaussian state [Filip 08] wich can be combined with QND interaction [Lemr 09]. In [Lemr 09] the non gaussianity of a light beam (a heralded photon substracted state) is transfered into the atomic system, and with coherent displacements depending on the result of the QND measurement, a the equivalent of photon subraction or addition can be implemented, allowing to prepare arbitrary Dicke states.

In photonic systems, to demonstrate the non-Gaussianity of the measured state two main techniques have been used. Histograms of the probability distribution function [Wenger 04] have been used as a simple and direct technique. Histograms

are related to the probability distribution but not directly to the non-classicality of the measured state. For this reason, state tomography have been used in several experiments [Ježek 11, Neergaard-Nielsen 06, Ourjoumtsev 07, Takahashi 08].

These approaches needs a significant number of measurements, typically a few  $10^4$ . In material systems like atomic spin measured using QND measurements, the time-scales may be significantly longer than in optical systems<sup>1</sup> making the previous approaches prohibitively expensive. In the following we will consider the use of cumulants which could be seen as global measures of distribution shape, to show non-Gaussianity in an atomic spin ensemble.

Cumulants can be used to show non-classicality [Bednorz 11], [Shchukin 05] and [Eran Kot 11]. Moreover, they can be estimated with few measurements and have known uncertainties [Kendall 58], a critical requirement for proofs of non-classicality. The known uncertainties allows to estimate statistical uncertainty on the measured value, thus allowing to limit the number of measurements.

### 8.1.2 Approach

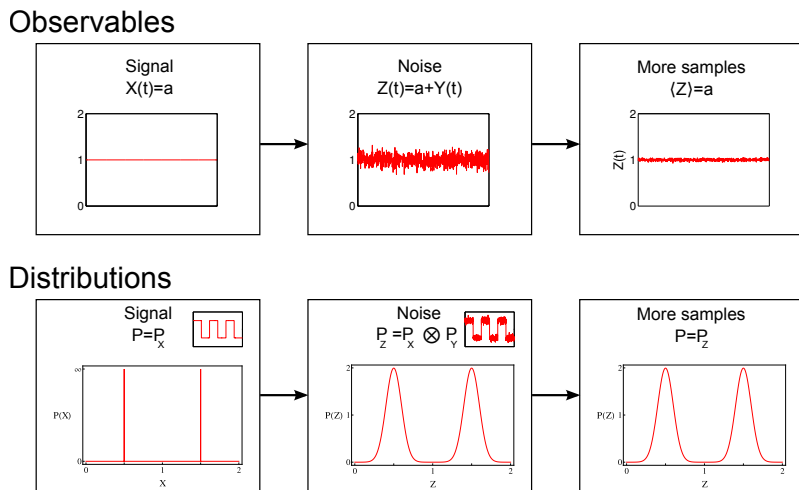


Figure 8.1: Illustration of the difference between observables and distributions estimation. Top: Quantification of observables, the measurement noise (if zero mean) does not change the measured value but only it's precision. Bottom: quantification of distributions, the alteration of the distribution by measurement noise cannot be suppressed by taking additional measurements.

Quantification or testing of distributions has features not encountered in quantification of observables as illustrated on figure Figure 8.1. In particular, experimental noise plays a major role as it distorts the measured distribution and cannot be “averaged away” by additional measurements. Additional, independent measurements

<sup>1</sup>The measurement time scale in an atomic system is typically in the microsecond [Koschorreck 10b] or millisecond range [Zhao 09a]. Optical system can have typical measurement time in the nanosecond or picosecond range [Wenger 04, Neergaard-Nielsen 06].

do not change the shape of the measured distribution, they increases the precision of the estimation of the distribution itself which includes the measurement noise. This situation is naturally handled by the theory of cumulants as will be seen later.

This work presented in this thesis is focused on the fourth-order cumulant  $\kappa_4$ , the lowest-order indicator of non-Gaussianity in symmetric distributions such as Fock [Lvovsky 01] and “Schrödinger kitten” states [Ourjoumtsev 06, Ourjoumtsev 07, Massar 03]. We study theoretically and experimentally the noise properties of Fisher’s unbiased estimator of  $\kappa_4$ , i.e., the fourth “k-statistic”  $k_4$  versus the measured distribution, the measurement noise and the number of samples acquired. Finally we find optimal measurement conditions. Because  $\kappa_4$  is related to the negativity of the Wigner function [Bednorz 11], this estimation is of direct relevance to detection of non-classical states.

## 8.2 Theory

### 8.2.1 Moments, cumulants and estimators

A continuous random variable  $X$  with probability distribution function  $P(X)$  is completely characterized by its moments

$$\mu_k \equiv \int X^k P(X) dX$$

or cumulants

$$\kappa_n = \mu_n - \sum_{k=1}^{n-1} \binom{n-1}{k-1} \mu_{n-k} \kappa_k$$

where  $\binom{n}{k}$  is the binomial coefficient.

This gives the first four cumulants:

$$\begin{aligned} \kappa_1 &= \mu_1 & \kappa_2 &= \mu_2 - \mu_1 & \kappa_3 &= \mu_3 - 3\mu_2\mu_1 + 2\mu_1^3 \\ \kappa_4 &= \mu_4 - 4\mu_1\mu_3 - 3\mu_2^2 + 12\mu_1^2\mu_2 - 6\mu_1^4 \end{aligned}$$

The two lowest-order cumulants are of common use,  $\kappa_1$  being the mean and  $\kappa_2$  the variance. A Gaussian distribution is fully characterized by  $\kappa_1$  and  $\kappa_2$  all other higher order cumulants being null. Thus, the estimation of  $\kappa_4$ , (or  $\kappa_3$  for non-symmetric distributions), is a natural test for non-Gaussianity. Intuitively,  $\kappa_3$  measures the asymmetry of the distribution compared to a Gaussian and  $\kappa_4$  its “peakedness”. For example, a “flat” distribution like  $P(X) = 1$  for  $|X| < 1/2$  and  $P(X) = 0$  elsewhere will have a negative value of  $\kappa_4$ .

In an experiment, a finite sample  $\{X_1 \dots X_N\}$  from  $P$  is used to estimate the  $\kappa$ ’s. Fisher’s unbiased estimators, known as “k-statistics”  $k_n$ , give the correct expectation values  $\langle k_n \rangle = \kappa_n$  for finite  $N$  [Kendall 58]  $\langle k_n \rangle$  being the expectation values of  $k_n$  i.e. the mean of  $k_n$  when it’s computed on several independent experiments. Other “naïve” estimators show a bias for finite  $N$ . The use of unbiased estimators is very

important for small sample numbers. Defining  $S_n = \sum_i X_i^n$  these estimators have been calculated by Fisher [Kendall 58] and can be written:

$$k_1 = \frac{S_1}{N} \quad (8.1)$$

$$k_2 = \frac{NS_2 - S_1^2}{N(N-1)} \quad (8.2)$$

$$k_3 = \frac{N^2 S_3 - 3NS_1 S_2 + 2S_1^3}{N(N-1)(N-2)} \quad (8.3)$$

$$k_4 = \frac{N^2(N+1)S_4 - 4N(N-1)S_1 S_3 - 3N(N-1)S_2^2}{N(N-1)(N-2)(N-3)} \\ + \frac{12NS_1^2 S_2 - 6S_1^4}{N(N-1)(N-2)(N-3)} \quad (8.4)$$

We need the uncertainty in the cumulant estimation to test for non-Gaussianity, or to compare non-Gaussianity between distributions. For hypothesis testing and maximum-likelihood approaches, we need the variances of the estimators  $k_3, k_4$  for a given probability distribution  $P$ . These are found by combinatorial methods and given by Kendall and Stuart [Kendall 58]:

$$\text{var}(k_3) = \frac{\kappa_6}{N} + 9N \frac{\kappa_2 \kappa_4 + \kappa_3^2}{N(N-1)} + \frac{6N^2 \kappa_2^3}{N(N-1)(N-2)} \quad (8.5)$$

$$\begin{aligned} \text{var}(k_4) &= \frac{\kappa_8}{N} + 2N \frac{8\kappa_6 \kappa_2 + 24\kappa_5 \kappa_3 + 17\kappa_4^2}{N(N-1)} \\ &\quad + 72N^2 \frac{\kappa_4 \kappa_2^2 + 2\kappa_3^2 \kappa_2}{N(N-1)(N-2)} \\ &\quad + \frac{24N^2(N+1)\kappa_2^4}{N(N-1)(N-2)(N-3)}. \end{aligned} \quad (8.6)$$

It is possible to estimate the uncertainty in  $k_4$  from data  $\{X\}$  using estimators of higher order cumulants [Kendall 58] (reported on Appendix A). The efficiency of cumulant estimation is illustrated in Fig. 8.2.

### 8.2.2 Measurement noise

When the measured signal is  $Z = X + Y$ , where  $X$  is the true value and  $Y$  is uncorrelated noise, the measured distribution is the convolution  $P(Z) = P(X) \otimes P(Y)$ . The effect of this distortion on cumulants is the following: for independent variables, cumulants accumulate (i.e., add) [Kendall 58], so that  $\kappa_n^{(Z)} = \kappa_n^{(X)} + \kappa_n^{(Y)}$ , where  $\kappa_n^{(Q)}, k_n^{(Q)}$  indicate  $\kappa_n, k_n$  for distribution  $P(Q)$ . For the extremely important case of uncorrelated, zero-mean Gaussian noise,  $\kappa_2^{(Y)} = \sigma_Y^2$  and other cumulants zero, is thus very simple:

$$\kappa_n^{(Z)} = \kappa_n^{(X)} \text{ except for } \kappa_2^{(Z)} = \kappa_2^{(X)} + \sigma_Y^2$$

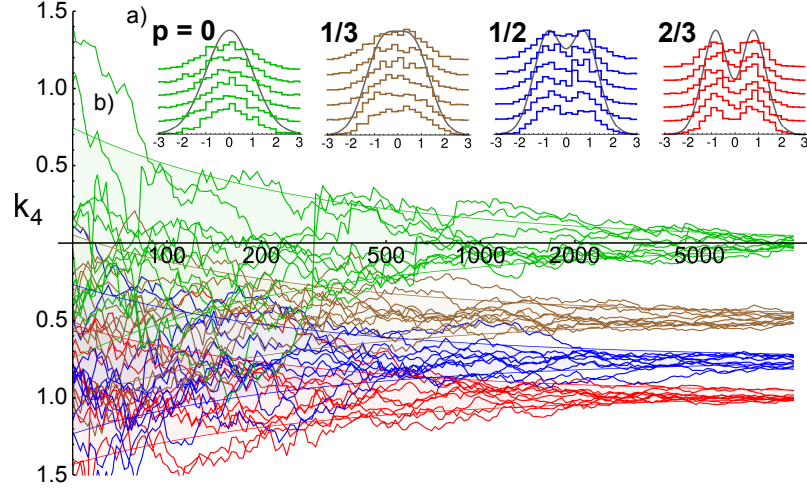


Figure 8.2: Simulated value of estimator  $k_4$  as a function of sample size  $N$  for a bi-Gaussian distribution. a) (insets) black curves show quadrature distributions of states  $\rho = (1 - p)|0\rangle\langle 0| + p|1\rangle\langle 1|$ , scaled to unit variance, and six  $N = 1000$  histograms (offset for clarity) for  $p = 0$  (green),  $1/3$  (brown),  $1/2$  (blue) and  $2/3$  (red). b) Ten realizations of  $k_4$  versus  $N$  drawn from each of the four distributions. Shaded regions show  $\kappa_4 \pm \sqrt{\text{var}(k_4)}$ , from Eqs (8.4), (8.6). With  $N = 1000$ ,  $k_4$  distinguishes  $p = 1/2$  (blue) from  $p = 0$  (green, Gaussian) with  $> 7\sigma$  significance, even though the histograms look similar “to the eye.”

Critically, added Gaussian noise does not alter the observed  $\kappa_3$ ,  $\kappa_4$ , but alters the observed variance see Equation 8.6. This result can also be found by computing the new values of the cumulants on  $P(Z)$ .

## Chapter conclusion

Cumulants are an interesting tool to detect non-Gaussian distributions. They uncertainty can be computed, both because of the finite measurement number and the measurement noise. We characterized this noise in the case of QND measurements, allowing to put a boundary on the detected values.



# Chapter 9

## Experimental set-up and measurement method

### Introduction

The experimental system is based on an atomic ensemble trapped in an elongated far off resonance dipole trap and measured via the induced Faraday rotation on polarized light pulses by a very low noise balanced polarimeter. The elongated geometry allows a strong interaction between the atomic ensemble and the probe light. Non gaussian test states (statistical mixtures) have been produced by partial optical pumping of a spin thermal state. The experimental system and the experimental procedure for producing and measuring non Gaussian states will be presented in this chapter. More information on the experimental system can be found in: [Koschorreck 10b, Koschorreck 10a] and, in particular in [Koschorreck 11].

### 9.1 Experimental system

The experimental set-up is represented in Figure 9.1. It consists in a two stage vacuum chamber pumped differentially with a rubidium source connected to the upper chamber. The laser system used for trapping and cooling is presented in Figure 9.2. It is constituted of two Extended cavity diode laser (ECDL) locked onto a saturated absorption cell using the Pound Drever Hall technique [Drever 83], one slave diode laser. These lasers are used for addressing the  $F = 1 \rightarrow F' = 0 - 2$  and the  $F = 1 \rightarrow F' = 1 - 3$  transitions. A third ECDL is used for the off-resonance probing and is locked using a digital offset lock between  $-400$  MHz and  $-1200$  MHz compared to the  $F = 1 \rightarrow F' = 0$  transition. The 1030 nm source for the dipole trap is a thin disk laser and delivers 15 W CW, single mode. All the laser sources are fiber coupled for delivering light to the trap, allowing easier alignment, clean spatial modes and better stability concerning the trap alignment. The fiber delivering the light for the optical dipole trap is a single mode, large mode area photonic crystal optical fiber. The light polarization is cleaned before and after the fiber. The fiber being not a polarization maintaining fiber, it is attached to the optical table, to

avoid change in the polarization (thus on the output power) due to changes in the stress of the optical fiber. All the other fibers are polarization maintaining fiber. The input polarization is cleaned by using high rejection polarization beam splitters (PBS). The PBS are mounted on rotational stages to allow fine alignment of the input polarization with the fiber axis. After the fibers the polarization is cleaned and adjusted for each light beam.

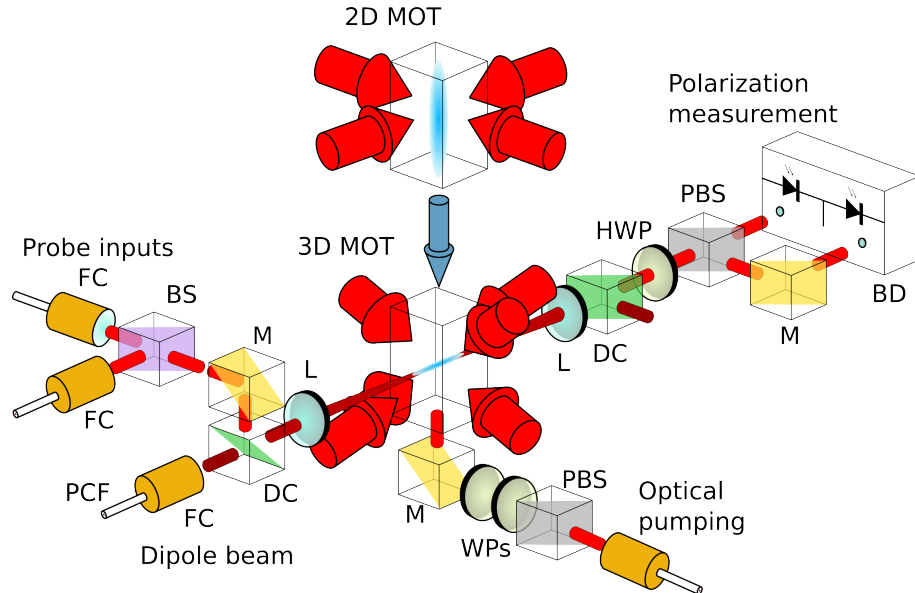


Figure 9.1: Presentation of the experimental setup. See text for details. On axis optical pumping is not represented on this figure.

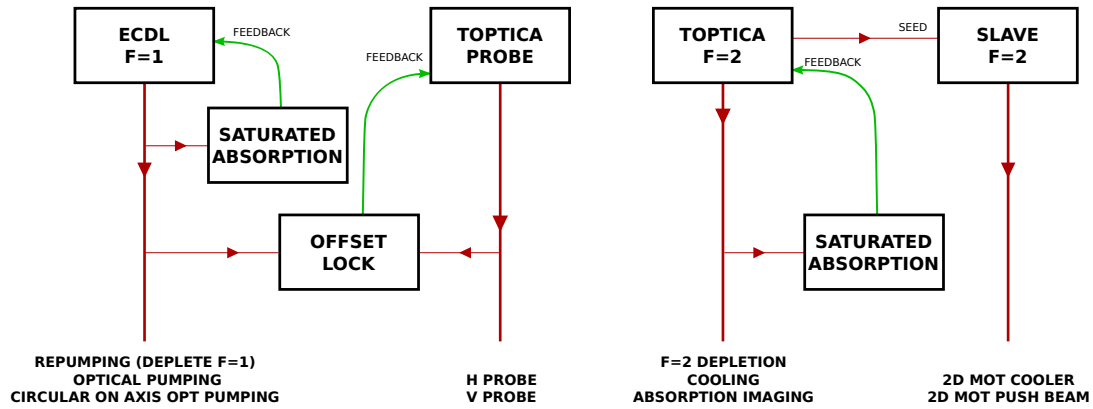


Figure 9.2: Laser system. See text for details.

An ensemble of  $^{87}\text{Rb}$  atoms are first loaded into a 2D magneto optical trap (MOT) in the upper part of the chamber. They are pushed to the lower chamber into

a 3D MOT. After a phase of sub-Doppler cooling, they are transferred into an elongated dipole trap made from a weakly focused single mode 7 W, 1030 nm beam and cooled to 25  $\mu\text{K}$ . The trapping depth of the dipole trap is typically 230  $\mu\text{K}$  limiting the trapped atoms temperature. Typically  $5 \times 10^5$  to  $1 \times 10^6$  atoms can be trapped in the dipole trap. The atomic cloud typically measures  $4 \text{ mm} \times 40 \mu\text{m} \times 40 \mu\text{m}$  (FWHM) allowing a strong light matter interaction, the measured effective optical density on resonance is  $d = 57(3)$  [Koschorreck 11]. An absorption image of a typical atomic cloud is reported on Figure 9.3.

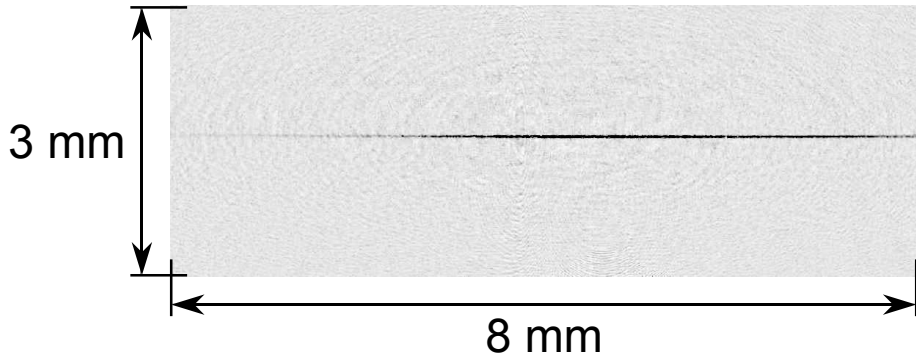


Figure 9.3: Absorption image of a typical atom cloud trapped in the dipole trap. The cloud contains about  $1 \times 10^6$  atoms.

A non-destructive measurement of the atomic state is made using pulses of linearly polarized light detuned 800 MHz to the red of the  $F = 1 \rightarrow F' = 0$  transition of the D<sub>2</sub> line (see Appendix B) and sent through the atoms in a beam matched to the transverse cloud size. The light experiences a polarization rotation proportional to the population difference between the  $|F = 1, m_F = -1\rangle$  and  $|F = 1, m_F = 1\rangle$  states. The linear polarization can be decomposed in two circular polarizations, each of those polarizations experience a phase shift proportional to the population of each Zeeman sublevel it interact with. The rotation of the linear polarization is thus proportional to the population difference.

In this context, the light polarization state is described by the Stokes operators  $\hat{\mathbf{S}}$ :

$$\begin{aligned}\hat{S}_0 &= \frac{1}{2} \left( \hat{a}_+^\dagger \hat{a}_+ + \hat{a}_-^\dagger \hat{a}_- \right) \\ \hat{S}_x &= \frac{1}{2} \left( \hat{a}_-^\dagger \hat{a}_+ + \hat{a}_+^\dagger \hat{a}_- \right) \\ \hat{S}_y &= \frac{1}{2} \left( \hat{a}_-^\dagger \hat{a}_+ - \hat{a}_+^\dagger \hat{a}_- \right) \\ \hat{S}_z &= \frac{1}{2} \left( \hat{a}_+^\dagger \hat{a}_+ - \hat{a}_-^\dagger \hat{a}_- \right)\end{aligned}$$

where  $\hat{a}_\pm^\dagger$ ,  $\hat{a}_\pm$  are respectively the creation and annihilation operators of the  $\sigma^\pm$  modes of the field.

As shown in [Geremia 06] we can express the atomic polarization in terms of the collective atomic pseudo-spin operators  $\hat{\mathbf{J}}$ :

$$\begin{aligned}\hat{J}_0 &= \frac{1}{2} \hat{N} \\ \hat{J}_x &= \frac{1}{2} \sum_k (\hat{F}_{x,k}^2 - \hat{F}_{y,k}^2) \\ \hat{J}_y &= \frac{1}{2} \sum_k (\hat{F}_{x,k} \hat{F}_{y,k} + \hat{F}_{y,k} \hat{F}_{x,k}) \\ \hat{J}_z &= \frac{1}{2} \sum_k \hat{F}_{z,k}\end{aligned}$$

Where  $\hat{N}$  is the atom number operator,  $\hat{F}_{i,k}$  is the  $i$ th component of the spin operator corresponding to the  $k$ th atom. The sum is over all atoms.

With these notations, the interaction Hamiltonian can be written the following way [Geremia 06, de Echaniz 08]:

$$\begin{aligned}\hat{H}_I^{(0)} &= \frac{4}{3} g \alpha^{(0)} \hat{S}_0 \hat{J}_0 \\ \hat{H}_I^{(1)} &= 2g \alpha^{(1)} \hat{S}_z \hat{J}_z \\ \hat{H}_I^{(2)} &= 2g \alpha^{(2)} \left( \hat{S}_x \hat{J}_x + \hat{S}_y \hat{J}_y + \frac{1}{3} \hat{S}_0 \hat{J}_0 \right)\end{aligned}$$

Where  $g$  is a coupling constant,  $\alpha^{(i)}$  are the tensor polarizability components of the atomic transition. The detuning of the probe is chosen such as the  $\alpha^{(1)}$  term dominates over the  $\alpha^{(2)}$  term, this condition is achieved when the probe is significantly detuned to the red of the  $F = 1 \rightarrow F' = 0$  transition. The term  $\hat{S}_0 \hat{J}_0$  which represents a global energy shift, can be ignored.

In this case, the mutual polarization - spin interaction when a pulse (of duration  $\tau$ ) passes through the ensemble can be described as evolution for a time  $\tau$  under an effective Hamiltonian.

$$\hat{H} = \hbar \frac{G}{\tau} \hat{J}_z \hat{S}_z$$

where  $G$  is a coupling constant depending on the detuning, the transition parameters and the spatial matching between the light field and the atomic cloud [Kubasik 09].

When the net polarization rotation is small, in the sense that  $S_y$  changes by much less than  $N_L$ , we can use the first-order input-output relation, giving:

$$\hat{S}_y^{(out)} \approx \hat{S}_y^{(in)} + G\hat{J}_z^{(in)}\hat{S}_x^{(in)}$$

Thus mapping the  $z$  component of the atomic state onto the light polarization state. The light input state is  $\langle \hat{S}_y \rangle = \langle \hat{S}_z \rangle = 0$ ,  $\langle \hat{S}_x \rangle = N_L/2$  with  $N_L$  being the number of photons. After interaction, the detected Stokes operator is proportional to the  $z$  component of the atomic spin. Because  $\langle \hat{S}_y \rangle$ , the input Stokes operator  $S_y^{(in)}$  only contributes to quantum noise. It represent the effect of the light shot noise on the measurement.

The pulses are of 1  $\mu$ s duration, contain  $3.7 \times 10^6$  photons on average, and are spaced by 10  $\mu$ s to allow individual detection. Precise timing is ensured by the use of a digital input output card with a hardware clock and FIFO (NI PCIe-6259) and a hardware pulse generator. The 240:1 aspect ratio of the atomic cloud creates a strong paramagnetic Faraday interaction  $G \approx 6 \times 10^{-8}$  rad/spin. After interaction with the atoms,  $S_y^{(out)}$  is detected with a shot noise limited (SNL) balanced polarimeter in the  $\pm 45^\circ$  basis. The probe photon number  $N_L$  is measured with a beam-splitter and reference detector before the atoms. The probing-plus-detection system is shot-noise-limited above  $3 \times 10^5$  photons/pulse. Previous work with this system has demonstrated QND measurement of the collective spin  $F_z$  with an uncertainty of  $\sim 500$  spins [Koschorreck 10b, Koschorreck 10a].

## 9.2 State preparation

For testing the previous approach Gaussian and non-Gaussian distributions are generated. The non-Gaussian test distribution is a statistical mixture of two displaced Gaussian spin distribution and is defined on Figure 9.4. The non-Gaussian distribution is defined by  $P_\alpha^{(NG)}(F_z) = [P_{\alpha+}(F_z) + P_{\alpha-}(F_z)]/2$  where  $P_{\alpha\pm}(F_z)$  is the gaussian distribution:  $P_{\alpha\pm}(F_z) = (\sigma\sqrt{2\pi})^{-1}\exp(-((F_z \pm \alpha)^2)/(2\sigma^2))$

The non-Gaussian distribution has the following cumulants:

$$\kappa_{odd} = 0 \tag{9.1}$$

$$\kappa_2 = \alpha^2 + \sigma^2 \tag{9.2}$$

$$\kappa_4 = -4\alpha^4 \tag{9.3}$$

$$\kappa_6 = 16\alpha^6 \tag{9.4}$$

$$\kappa_8 = -272\alpha^8 \tag{9.5}$$

The Gaussian and non-Gaussian distributions are prepared with the following strategy: we prepare a “thermal state” (TS), an equal mixture of the  $F = 1, m_F = -1, 0, 1$  ground states, by repeated optical pumping between the  $F = 1$  and  $F = 2$  hyperfine levels. The optical pumping is performed with the 3D MOT laser beams, thus producing a highly varying spatial polarization pattern. The lasers are tuned to the  $F = 1 \rightarrow F' = 2$  and  $F = 2 \rightarrow F' = 2$  transitions. Different phases of

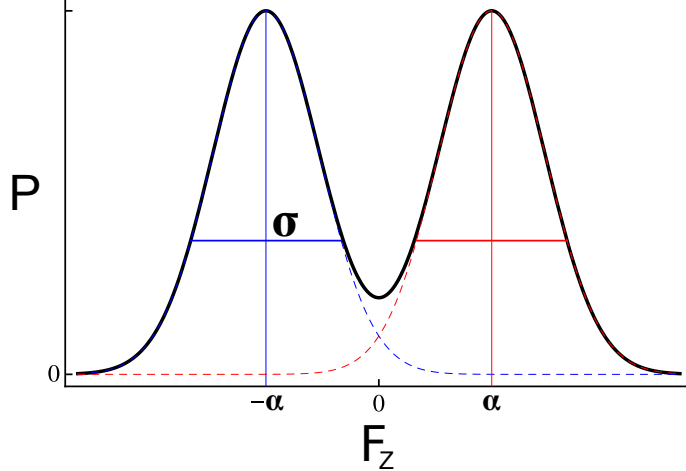


Figure 9.4: The test distribution (black line) is a statistical mixture of two displaced Gaussian distributions (red and blue dashed lines).

optical pumping ( $\approx 300 \mu\text{s}$  long each) are performed with different magnetic field directions to suppress any net polarization [Koschorreck 10b].

Because the thermal spin state of each atom is random and independent, at the limit of a large number of atoms, the macroscopic spin distribution is Gaussian with  $\langle F_z \rangle = 0$  and, for a spin 1 state,  $\text{var}(F_z) = \sigma^2 = 2N_A/3$ .

By optical pumping with pulses of on resonance circularly-polarized light we displace this to  $\langle F_z \rangle = \alpha$ , with negligible change in  $\text{var}(F_z)$ <sup>1</sup> [Tóth 10], to produce

$$P_\alpha(F_z) = \frac{1}{\sigma\sqrt{2\pi}} \exp\left(-\frac{(F_z - \alpha)^2}{2\sigma^2}\right)$$

By displacing different thermal states alternately to  $\alpha_+$  and  $\alpha_-$ , we produce an equal statistical mixture of the two displaced states, represented on Figure 9.4:

$$P_\alpha^{(\text{NG})}(F_z) = \frac{1}{2} (P_{\alpha_+}(F_z) + P_{\alpha_-}(F_z))$$

With properly-chosen  $\alpha_\pm$ ,  $P_\alpha^{(\text{NG})}(F_z)$  closely approximates marginal distributions of mixtures of  $n = 0, 1$  Fock (number) states and  $m = N, N - 1$  symmetric Dicke states. The experimental sequence is shown in Figure 9.5.

The optical pumping beams are matched with the atomic cloud and counter propagating. Both beams are matched with the probe beam, firstly by optimizing the coupling of the probe beam into the fiber of the backward pump beam, adjusting the backward beam mirrors. Then the forward beam is aligned by optimizing its coupling into the backward beam fiber. The beams are controlled independently with their respective AOMs.

---

<sup>1</sup>The noise increase is about  $\sqrt{N_P}$  where  $N_P \approx 10^3$  is the number of photons absorbed by the atoms during the pumping process. Giving a noise significantly lower than the shot noise of  $10^6$  atoms.

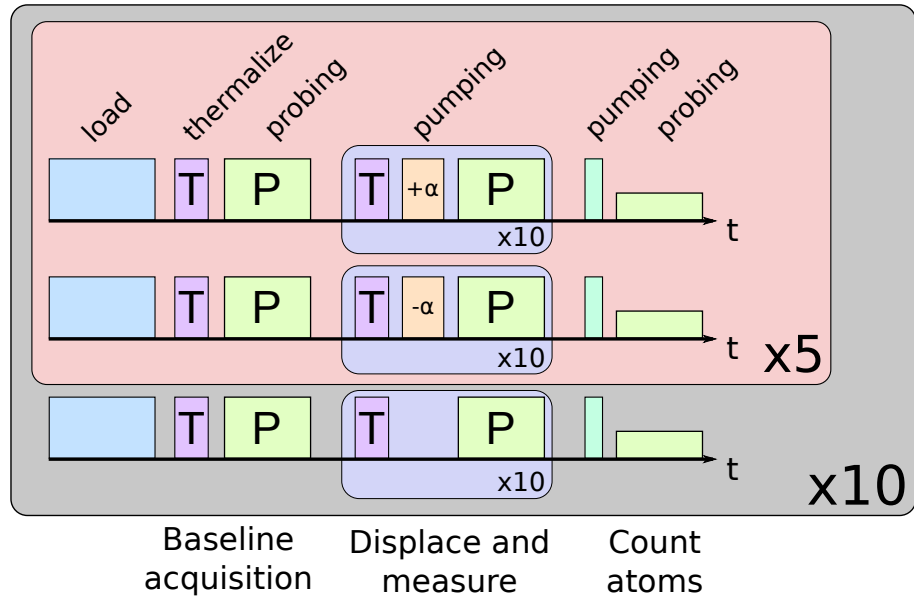


Figure 9.5: Experimental sequence: The experimental sequence divides into distinct tasks. Baseline acquisition: prepare the thermal state and probe to measure the residual rotation. Displace and measure (DM[ $\alpha$ ]): prepare the thermal state, displace by  $\alpha$  and probe. Approx 10% of atoms are lost at each thermalization, so that the number of atoms  $N_A$  drops in steps from  $\approx 8 \times 10^5$  to  $\approx 2.5 \times 10^5$  during the whole sequence. Measure number of atoms  $N_A$ : by pumping the atoms into  $F=1$ ,  $m_F=1$  and probing we measure the number of atoms in the trap. To correct for drifts, a sequence without displacement (DM[0]) is performed every 11 runs. We perform the sequence varying the displacement to acquire a dataset of quantum-noise-limited measurements of  $P_\alpha^{(\text{NG})}(S_y^{(\text{out})})$  for different  $\alpha$ . Durations: loading and cooling 5 s, thermalization 1 ms, probing 1 ms, pumping 100  $\mu$ s.

### 9.3 Data acquisition and normalization

For each preparation, 100 measurements of  $F_z$  are made, with readings (i.e., estimated  $F_z$  values by numerical integration of the measured signal)  $m_i = 2S_y^{(\text{out},i)}/N_L^{(i)}$ . In order to reduce technical noise and compensate for possible drifts, the numerical integration includes a electronic background subtraction step: the electronic level measured before each pulse is subtracted from the corresponding pulse.

Imperfect thermalization produce a small residual atomic polarization. This residual polarization depends on the number of atoms in the trap, and its fluctuation produce excess noise in the data. The change of this polarization versus the number of atoms is measured with the sequences without displacement DM[0] (see Figure 9.5) and subtracted from the main signal using the reference without optical pumping.

The measurement from the pulse  $ip$ , of the load  $il$ , after  $idm$  thermalization is computed the following way

$$m(ip, il, idm) = \frac{S_y^{(\text{out})}(ip, il, idm)}{N_P(ip, il, idm)} - \left\langle \frac{S_y^{(\text{out})}(ip, il, idm = 0)}{N_P(ip, il, idm = 0)} \right\rangle_{ip} \times \frac{\langle S_y^{(\text{out})}(idm) \rangle_{(il, ip, \alpha=0)}}{\langle S_y^{(\text{out})}(idm = 0) \rangle_{(il, ip, \alpha=0)}}$$

With  $idm = 0$ : baseline acquisition,  $N_P$ : probe photon number.

Because the measurement is non-destructive and shot noise limited, we can combine readings in a higher-sensitivity metapulse with reading  $M \equiv \sum m_i$  [Koschorreck 10b]. This metapulse (containing  $N_R$  readings) is equivalent to performing a measurement with  $N_R \times N_L$  photons and can be seen as erasing the time information from the detector. This technique allows to vary the readout noise without performing additional measurements.

# Chapter 10

## Noise performance of cumulant based approach

The non-Gaussian experimental states allow to compare the measured cumulants values, and their noise expectations with the experimental data. In the following chapter the analysis of the experimental data, as well as the calibration of the noise sources and the comparison with the expectations is presented.

### 10.1 Detection, Analysis and Results

For a given optical pumping strength  $\alpha$ , the measurements can be described by the distribution

$$P_{\alpha\pm}(M) = \frac{1}{\sigma_M \sqrt{2\pi}} \exp\left(-\frac{(M \pm \alpha)^2}{2\sigma_M^2}\right)$$

where the variance  $\sigma_M^2 = \sigma_A^2 N'_A{}^2 N_R^2 + \sigma_R^2$  includes atomic noise  $\sigma_A^2 N'_A{}^2$  with  $N'_A = N_A/N_A^{MAX}$  (with  $N_A^{MAX}$  the mean number of atoms after loading) and readout noise,  $\sigma_R^2 = N_R/N_L$  due to the probe light shot noise.

The variance  $\sigma_A^2$  is determined from the scaling of  $\text{var}(M)$  with  $N_A$  and  $N_R$ , as in [Koschorreck 10b]. The variance of the measured distributions (with fixed  $N_A$ ,  $N_R$ ) for each pumping direction is computed. The expression  $\sigma_M^2 = \sigma_A^2 N'_A{}^2 N_R^2 + \sigma_R^2$  is fitted with the measured variance, with  $\sigma_A$  as variable.

The readout noise  $\sigma_R^2$  can be varied over two orders of magnitude by appropriate choice of the number of pulses  $N_R$  used in the metapulses. For one probe pulse and the maximum number of atoms we have  $\frac{\sigma_R^2}{\sigma_A^2 N'_A N_R} = 84.7$ .

The non-Gaussian test distribution is produced by composing metapulses from  $N_R$  samples drawn from displaced thermal state ( $\text{DM}[\alpha_+]$  or  $\text{DM}[\alpha_-]$ ) preparations with equal probability, giving distribution  $P_\alpha^{(NG)}(M) = [P_{\alpha_+}(M) + P_{\alpha_-}(M)]/2$ . With  $\alpha_M \equiv (\alpha_+ - \alpha_-)/2$ .

Our ability to measure the non-Gaussianity is determined by  $\langle k_4 \rangle = \kappa_4$  and from Equation 8.6. The combination of Equation 9.1 and Equation 8.6 gives :

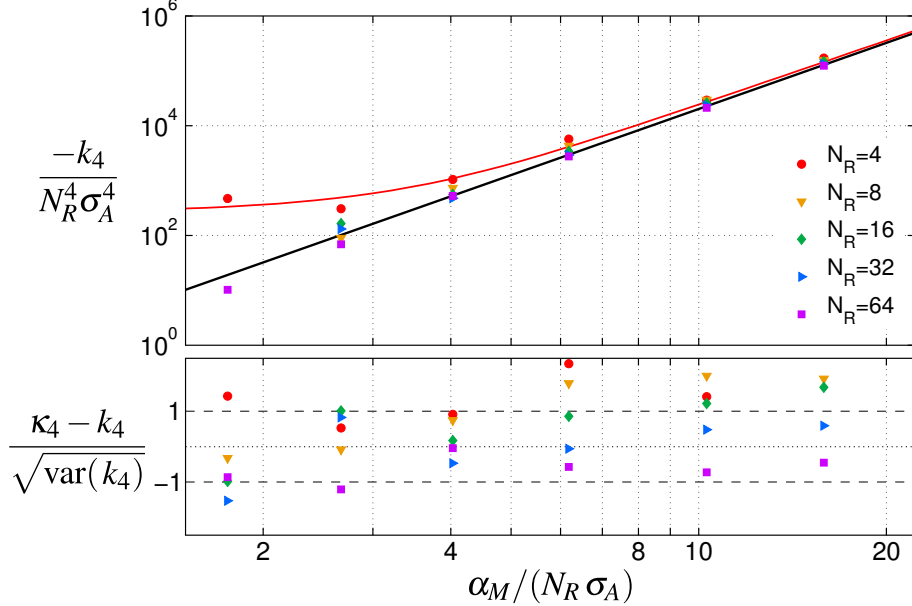


Figure 10.1: Measured and predicted  $k_4$  with residuals for non-Gaussian distributions of different  $\alpha$ . Readout noise is varied by the choice of the number of pulses  $N_R$  used in the metapulses. Top: Points show normalized  $-k_4$  calculated from  $N = 100$  preparations of the ensemble. Black line indicates expected  $-k_4/N_R^4\sigma_A^2$  calculated using equation Equation 9.1 and  $\sigma_A$  determined from the analysis of the independent distributions, red line (top) shows  $-k_4 + \sqrt{\text{var}(k_4)}$  calculated from the distribution parameters for the largest readout noise. Bottom: normalized residuals.

$$\begin{aligned} \text{var}(k_4) &= 136\alpha_M^8 - \frac{144N\alpha_M^4(\alpha_M^2 + \sigma_M^2)^2}{N-1} \\ &\quad + \frac{24N(N+1)(\alpha_M^2 + \sigma_M^2)^4}{(N-1)(N-2)} \end{aligned} \quad (10.1)$$

As shown in Figure 10.1, the experimentally obtained values agree well with theory, and confirm the independence from measurement noise.

The “signal-to-noise ratio” for  $\kappa_4$ ,  $S = \kappa_4^2/\text{var}(k_4)$ , is computed using Equation 10.1,  $\kappa_4 = -2\alpha_M^4$ , and experimental  $\alpha_M$ ,  $N_R$ ,  $\sigma_R$ , is shown as curves in Figure 10.2. We can confirm this  $S$  experimentally by computing  $S_N \equiv \langle k_4 \rangle^2 / \text{var}(k_4)$  using  $k_4$  values derived from several realizations of the experiment, each sampling  $P_\alpha^{NG} N$  times. In the limit of many realizations  $S_N \rightarrow S$ . We employ a bootstrapping technique: From 100 samples of  $P_\alpha^{(NG)}(M)$  for given parameters  $\alpha_M$ ,  $N_R$  and  $N_A$ , we derive thirty-three  $N = 20$  realizations by random sampling without replacement, and compute  $\langle k_4 \rangle$  and  $\text{var}(k_4)$  on the realizations. As shown in Figure 10.2, agreement with theory is observed. The deviations at low signal to noise ratio are coming probably from the statistical noise on the signal to noise.

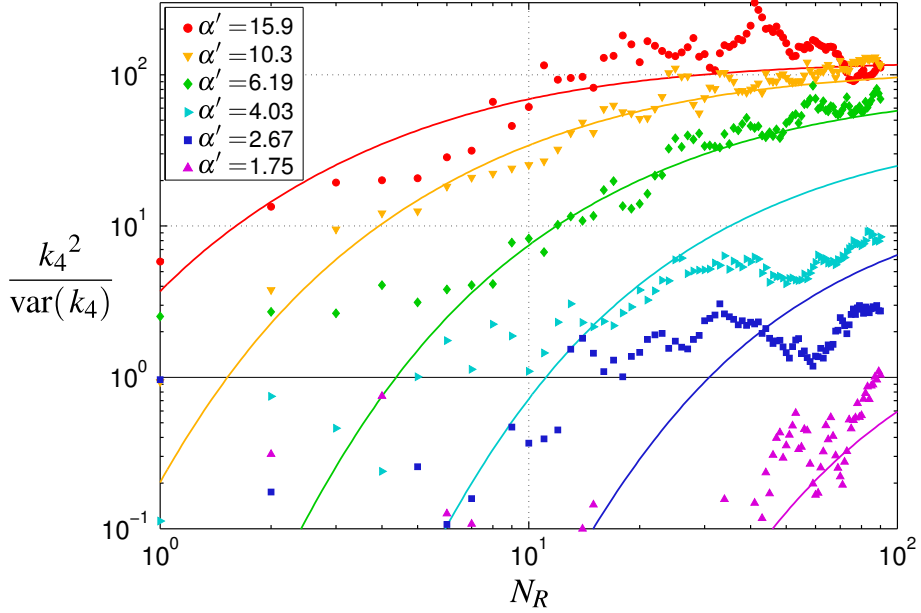


Figure 10.2: Signal-to-noise in estimation of  $\kappa_4$  versus readout noise for different  $\alpha' = \alpha_M/(N_R \sigma_A)$ . Points show measurement results, lines show theory.

## 10.2 Optimum estimation of non-Gaussian distributions

We note that in scenarios where measurements are expensive relative to state preparation (as might be the case for QND measurements of optical fields or for testing the successful storage of a single photon in a quantum memory), optimal use of measurement resources (e.g. measurement time) avoids both too few preparations and too few probings.

We consider a scenario of practical interest for quantum networking: a heralded single-photon state is produced and stored in an atomic ensemble quantum memory[Filip 08]. Assuming the ensemble is initially polarized in the  $\hat{X}$  direction, the storage process maps the quadrature components  $X, P$  onto the corresponding atomic spin operators  $X_A, P_A \propto F_z, -F_y$ , respectively. QND measurements of  $F_z$  are used to estimate  $X_A$ , and thus the non-Gaussianity of the stored single photon. Due to imperfect storage, this will have the distribution of a mixture of  $n = 0$  and  $n = 1$  Fock states:  $\rho = (1 - p)|0\rangle\langle 0| + p|1\rangle\langle 1|$ . For a quadrature  $X$ , we have the following probability distribution

$$P_p(X) = \frac{1}{\sqrt{2\pi}\sigma_0} \exp\left(-\frac{x^2}{2\sigma_0^2}\right) \left(\frac{px^2}{\sigma_0^2} + 1 - p\right)$$

, where  $\sigma_0$  is the width of the  $n = 0$  state.

Taking in account the readout noise  $\sigma_R^2$ , the cumulants are  $\kappa_{\text{odd}} = 0$ ,  $\kappa_2 = (2p + 1)\sigma_H^2 + \sigma_R^2$ ,  $\kappa_4 = -12p^2\sigma_H^4$ ,  $\kappa_6 = 240p^3\sigma_H^6$ ,  $\kappa_8 = -10080p^4\sigma_H^8$ , where the

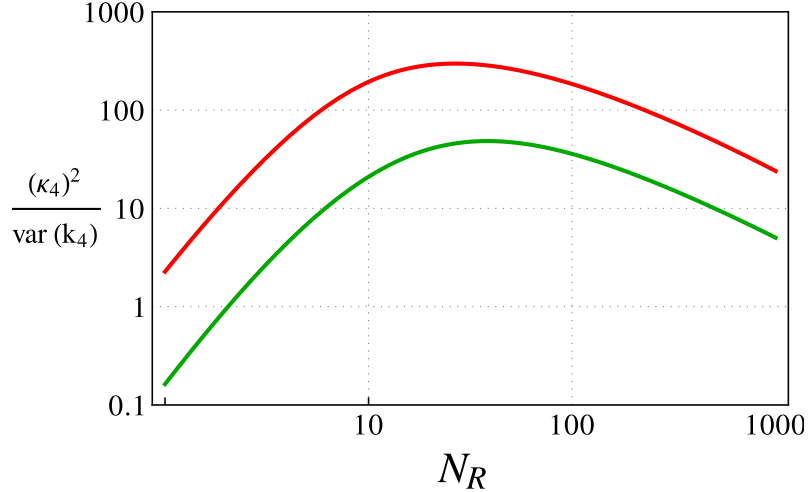


Figure 10.3: Signal-to noise-ratio  $S$  versus  $N_R$  for a fixed probe number  $N_M N_R = 1 \times 10^5$  for the probability distribution associated with Fock state mixture described in the text with a normalized  $n=0$  width  $\sigma_0 = 1$ . Red curve (top):  $p=1$ . Green curve (bottom):  $p=0.5$  with SNL measurement:  $\sigma_R = \sqrt{20/N_R}$ .

readout noise  $\sigma_R^2$  is included as above. Here  $\kappa_4$  is directly related to the classicality of the state, since  $p > 0.5$  implies a negative Wigner distribution [Lvovsky 01].

For a fixed total number of measurement resources  $N_M N_R$ , an optimal distribution of resources per measurement  $N_R$  exists as shown in Figure 10.3. With increasing  $N_R$ , the signal-to-noise first increases due to the improvement of the measurement precision. Then, once the increased measurement precision no longer gives extra information about  $\kappa_4$ , the precision decreases due to reduced statistics because of the limited total number of probes. For a large total number of measurements, we can derive a simplified expression of this optimum. We derive asymptotic expressions of  $S$ :  $S_L$  ( $S_H$ ) for  $\sigma_R \ll \sigma_0$  ( $\sigma_R \gg \sigma_0$ ). The optimal  $N_R$  is found by solving  $S_L = S_R$  giving  $\sigma_R^8 \approx \sigma_0^8(1 + 8p - 12p^2 + 48p^3 - 24p^4)$ . For this optimal  $\sigma_R$ , the measurement noise is in the same order of magnitude as the characteristic width of the non-Gaussian distribution.

### 10.3 Conclusion

We have demonstrated a good agreement between the expected noise and the experimental signal to noise ratio, thus validating the cumulant approach for non-Gaussian atomic states. We have also noted an interesting scenario where the use of the resource can be optimized in order to reduce the noise on the estimation of the fourth order cumulant. The approach described here can be easily extended to other non Gaussian states.

# Chapter 11

## Conclusion

The cumulant-based methods described here should be very attractive for experiments with non-Gaussian states of material systems such as atomic ensembles and nano-resonators, for which the state preparation time is intrinsically longer, and for which measurement noise is a greater challenge than in optical systems. The measurement noise does not affect the measured value, and its contribution to the statistical noise can be evaluated thus allowing to evaluate boundaries on the measured values. This advantage is valid only for noise source with a Gaussian probability distribution. Care have to be taken with technical noise (compared to shot noise) which can have a broad range of probability distributions. Experimental tests have been performed with a cold atomic ensemble that demonstrate the method in a system highly suitable for quantum networking, while the theory applies equally to other quantum systems of current interest.

Non classicality of the measured state can be easily demonstrated if assumptions on the measured states is done. For example in the case of a statistical mixture between  $n = 0$  and  $n = 1$  Fock states  $\rho = (1 - p)|0\rangle\langle 0| + p|1\rangle\langle 1|$ , the fourth order cumulant gives information about the value of the parameter  $p$  and bounds it, allowing to evaluate if the original state is non classical in the sence of having a negative Wigner function. In the general case cumulants can prove non-classicality [Bednorz 11, Shchukin 05, Eran Kot 11] but work have still to be done in order to obtain a simple set of criterion well adapted to experimental systems currently used or proposed.

This approach can be extended to higher order cumulants in order to obtain a higher amount of information on the probability distribution, thus the quantum state. To confirm the interest of this method for evaluating unknown non Gaussian quantum states, the reconstruction problem have still to be addressed. In particular what information is brought by increasing the order of the evaluation. Knowing that the statistical noise is expected to increase with the order of the evaluated cumulant for a given "physical" distribution.



# **Part III**

## **Conclusion**



Two aspects of light matter interaction with atomic ensembles have been studied in the perspective of writing information from light to the atomic state with trapped ion ensembles and studying a new method to read information from the atomic ensemble, in the context of non-Gaussian states measured with Quantum Non Demolition measurements.

The work with trapped ions allowed us to reach significant probe absorption levels in a large coulomb crystal and observing the signature of Electromagnetically Induced Transparency in such a system. Strong absorption combined with the quantum control of the atomic state are necessary building blocks for a ion ensemble based quantum memory. The light matter interaction probability levels observed during this thesis despite being unprecedented in such systems are too low in the context of building a quantum memory with trapped ion ensembles. Radio frequency heating has been identified as the possible main limitation in such system. Further studies are needed to understand this phenomenon in large ion ensembles and improving trap design in order to minimize it. Together with this study, it is necessary to measure and optimize the coherence time in large ion ensembles. These measurements would allow one to evaluate the qualities of large ion ensembles for quantum information storage and processing.

On the other side the question of extracting information from atomic ensemble have been asked in the experimental context of a large cold Rubidium ensemble measured with low noise Quantum Non Demolition measurements. In particular the question of the detection of non Gaussian states in such systems have been addressed. Non Gaussian states are an essential building block for quantum information processing with continuous variables. The production and the measurement of non Gaussian states have been performed in photonic systems and proposals are actively pursued in atomic systems. Since atomic systems are usually more difficult to measure (higher noise and longer time scale), particular tools can be needed to detect such states efficiently. The work performed allowed to evaluate the possibility of using statistical tools as cumulants in this context. Cumulants allow to evaluate non Gaussian state with few measurements and known uncertainty which have been compared against a classical non Gaussian test state. Non classicality is linked with the cumulants, but in a relatively complex way. More theoretical work is needed to obtain simple boundaries adapted to recent experimental proposals.



# Appendices



# Appendix A

## Cumulants estimators and variance

### A.1 Fisher's k-statistics

We define

$$S_n = \sum_{i=0}^N (X_i)^n$$

where  $X_i$  it the  $i^{th}$  measurement

and

$$N_{(m)} = \prod_{i=0}^{m-1} (N - i)$$

From [Kendall 58] we have :

$$\begin{aligned} k_1 &= \frac{1}{N_{(1)}} S_1 \\ k_2 &= \frac{1}{N_{(2)}} \left( N S_2 - S_1^2 \right) \\ k_3 &= \frac{1}{N_{(3)}} \left( N^2 S_3 - 3N S_2 S_1 + 2S_1^3 \right) \\ k_4 &= \frac{1}{N_{(4)}} \left( N^2 (N+1) S_4 - 4N(N+1) S_3 S_1 \right. \\ &\quad \left. + 12N S_2 S_1^2 - 3N(N-1) S_2^2 - 6S_1^4 \right) \end{aligned}$$

$$k_5 = \frac{1}{N_{(5)}} \left( (N^4 + 5N^3)S_5 - 5(N^3 + 5N^2)S_4S_1 - 10(N^3 - N^2)S_3S_2 \right. \\ \left. + 20(N^2 + 2N)S_3S_1^2 + 30(N^2 - N)S_2^2S_1 - 60NS_2S_1^3 + 24S_1^5 \right)$$

$$k_6 = \frac{1}{N_{(6)}} \left( (N^5 + 16N^4 + 11N^3 - 4N^2)S_6 - 6(N^4 + 16N^3 + 11N^2 - 4N)S_5S_1 \right. \\ \left. - 15N(N - 1)^2(N + 4)S_4S_2 - 10(N^4 - 2N^3 + 5N^2 - 4N)S_3^2 \right. \\ \left. + 30(N^3 + 9N^2 + 2N)S_4S_1^2 + 120(N^3 - N)S_3S_2S_1 \right. \\ \left. + 30(N^3 - 3N^2 + 2N)S_2^3 - 120(N^2 + 3N)S_3S_1^3 \right. \\ \left. - 270(N^2 - N)S_2^2S_1^2 + 360NS_2S_1^4 - 120S_1^6 \right)$$

$$k_7 = \frac{1}{N_{(7)}} \left( (N^6 + 42N^5 + 119N^4 - 42N^3)S_7 - 7(N^5 + 42N^4 + 119N^3 - 42N^2)S_6S_1 \right. \\ \left. - 21(N^5 + 12N^4 - 31N^3 + 18N^2)S_5S_2 - 35(N^5 + 5N^3 - 6N^2)S_4S_3 \right. \\ \left. + 42(N^4 + 27N^3 + 44N^2 - 12N)S_5S_1^2 + 210(N^4 + 6N^3 - 13N^2 + 6N)S_4S_2S_1 \right. \\ \left. + 140(N^4 + 5N^2 - 6N)S_3^2S_1 + 210(N^4 - 3N^3 + 2N^2)S_3S_2^2 \right. \\ \left. - 210(N^3 + 13N^2 + 6N)S_4S_1^3 - 1260(N^3 + N^2 - 2N)S_3S_2S_1^2 \right. \\ \left. - 630(N^3 - 3N^2 + 2N)S_2^3S_1 + 840(N^2 + 4N)S_3S_1^4 \right. \\ \left. + 2520(N^2 - N)S_2^2S_1^3 - 2520NS_2S_1^5 + 720S_1^7 \right)$$

$$\begin{aligned}
k_8 = \frac{1}{N_{(8)}} & \left( (N^7 + 99N^6 + 757N^5 + 141N^4 - 398N^3 + 120N^2)S_8 \right. \\
& - 8(N^6 + 99N^5 + 757N^4 + 141N^3 - 398N^2 + 120N)S_1S_7 \\
& - 28(N^6 + 37N^5 - 39N^4 - 157N^3 + 278N^2 - 120N)S_6S_2 \\
& - 56(N^6 + 9N^5 - 23N^4 + 111N^3 - 218N^2 + 120N)S_5S_3 \\
& - 35(N^6 + N^5 + 33N^4 - 121N^3 + 206N^2 - 120N)S_4^2 \\
& + 56(N^5 + 68N^4 + 359N^3 - 8N^2 + 60N)S_6S_1^2 \\
& + 336(N^5 + 23N^4 - 31N^3 - 23N^2 + 30N)S_5S_2S_1 \\
& + 560(N^5 + 5N^4 + 5N^3 + 5N^2 - 6N)S_4S_3S_1 \\
& + 420(N^5 + 2N^4 - 25N^3 + 46N^2 - 24N)S_4S_2^2 \\
& + 560(N^5 - 4N^4 + 11N^3 - 20N^2 + 12N)S_3^2S_2 \\
& - 336(N^4 + 38N^3 + 99N^2 - 18N)S_5S_1^3 \\
& - 2520(N^4 + 10N^3 - 17N^2 + 6N)S_4S_2S_1^2 \\
& - 1680(N^4 + 2N^3 + 7N^2 - 10N)S_3^2S_1^2 \\
& - 5040(N^4 - 2N^3 - N^2 + 2N)S_3S_2^2S_1 \\
& - 630(N^4 - 6N^3 + 11N^2 - 6N)S_2^4 \\
& + 1680(N^3 + 17N^2 + 12N)S_4S_1^4 \\
& + 13440(N^3 + 2N^2 - 3N)S_3S_2S_1^3 \\
& + 10080(N^3 - 3N^2 + 2N)S_2^3S_1^2 \\
& - 6720(N^2 + 5N)S_3S_1^5 \\
& - 25200(N^2 - N)S_2^2S_1^4 \\
& + 20160NS_2S_1^6 \\
& \left. - 5040S_1^8 \right)
\end{aligned}$$

## A.2 Variance of Fisher's k-statistics estimators

$$\begin{aligned}
 \kappa(2^2) &= \frac{\kappa_4}{n} + \frac{2\kappa_2^2}{n-1} \\
 \kappa(3^2) &= \frac{\kappa_6}{n} + \frac{9\kappa_4\kappa_2}{n-1} + \frac{9\kappa_3^2}{n-1} + \frac{6n\kappa_2^3}{(n-1)(n-2)} \\
 \kappa(4^2) &= \frac{\kappa_8}{n} + \frac{16\kappa_6\kappa_2}{n-1} + \frac{48\kappa_5\kappa_3}{n-1} + \frac{34\kappa_4^2}{n-1} + \frac{72n\kappa_4\kappa_2^2}{(n-1)(n-2)} \\
 &\quad + \frac{144n\kappa_3^2\kappa_2}{(n-1)(n-2)} + \frac{24n(n+1)\kappa_2^4}{(n-1)(n-2)(n-3)}
 \end{aligned}$$

# Appendix B

## Rubidium data

### B.1 D<sub>2</sub> line of <sup>87</sup>Rb

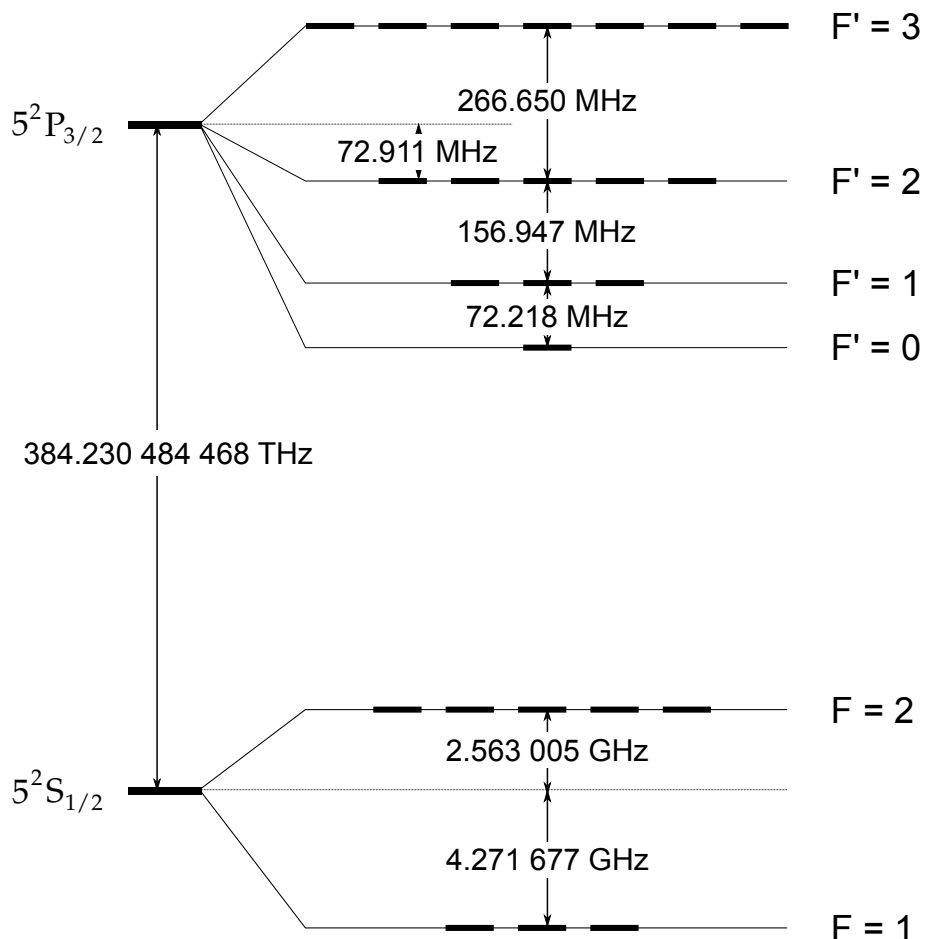


Figure B.1:  $^{87}\text{Rb}$  D<sub>2</sub> line [Steck 03]



# Appendix C

## Offset lock for MBR

**Overview** The general scheme of the offset lock implemented for the Coherent MBR-110 laser is presented on Figure C.1. This offset lock is derived from the design presented in [Appel 09b]. It allows more flexibility on the lock of the laser and improved reliability. The laser is locked to the beatnote with a Toptica DL-100 laser diode locked to a rubidium saturated absorption spectroscopy. A few 100  $\mu\text{W}$  of light from each of the two lasers is used for the beating on a fast photodiode, amplified firstly with a homemade transimpedance amplifier with a gain of  $50 \times 10^3 \text{ V A}^{-1}$ , this signal is then amplified using a Mini-Circuits<sup>®</sup> ZFL-500LN amplifier with a gain of 28 dB. This amplifier is also used as a protection, the saturation output power being lower than the maximum input power of the signal processing stage.

**Particularities** The bandwidth needed being relatively low, this offset lock is based on a analog devices N-divider PLL with a bandwidth of 400 MHz: the ADF4002.

The feedback in the MBR-110 is performed on a piezo of a cavity mirror, allowing a low feedback bandwidth of a few Hz. To avoid oscillations, it is important to increase the typical time constant of the loop filter. The filter being mainly integral, the right time constant to take into account is the time for saturating the output when the error signal is maximum. This time is chosen to be a few 100 ms.

The output signal of the ADF4002 is a charge pump, with the sign of the delivered current depending on the sign of the frequency difference. Whereas this charge pump is able to drive negative current, it is not able to produce negative voltages. Thus it is important that the time constant of the first stage, the passive integral filter, are not too low in order to avoid saturation of the charge pump, in particular for negative currents.

**characterization and results** The offset lock has been characterized using a saturated absorption spectroscopy setup.

A typical error signal is depicted on Figure C.2. The sign change of the error signal at  $\approx \pm 600 \text{ MHz}$  is due to a folding of the spectrum<sup>1</sup> with the (undocumented) effective sampling frequency of the input divider which we measured to be about

---

<sup>1</sup>Third order Nyquist harmonic

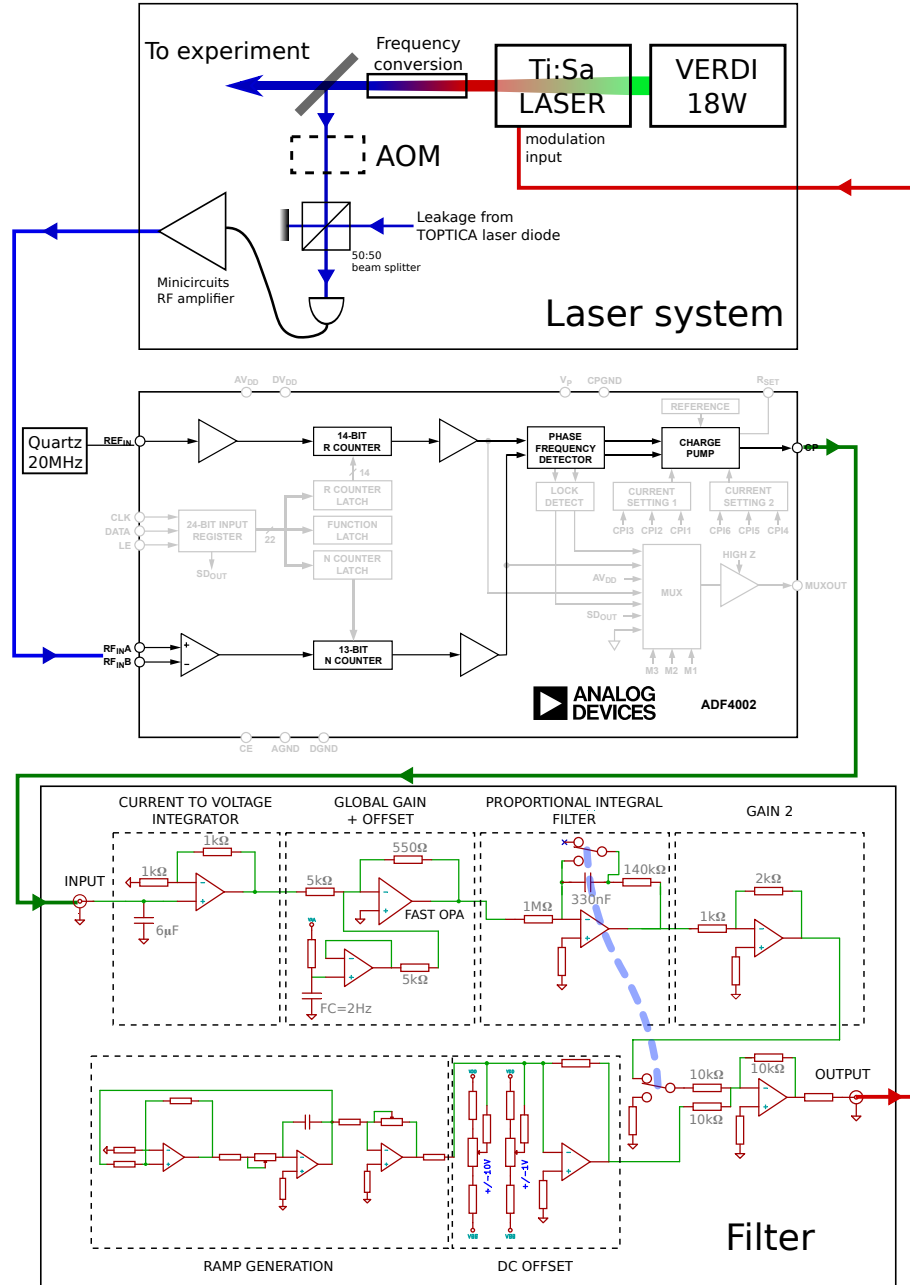


Figure C.1: Offset lock general scheme

The laser to lock is beating with a reference laser (top part), this beating signal is then sent to the detection system (middle part) which will generate an error signal depending on the setpoint. This error signal is then sent to a feedback filter (bottom part). The output signal is then sent back to the laser.

The filter contains also the generation of a triangle ramp and offset.

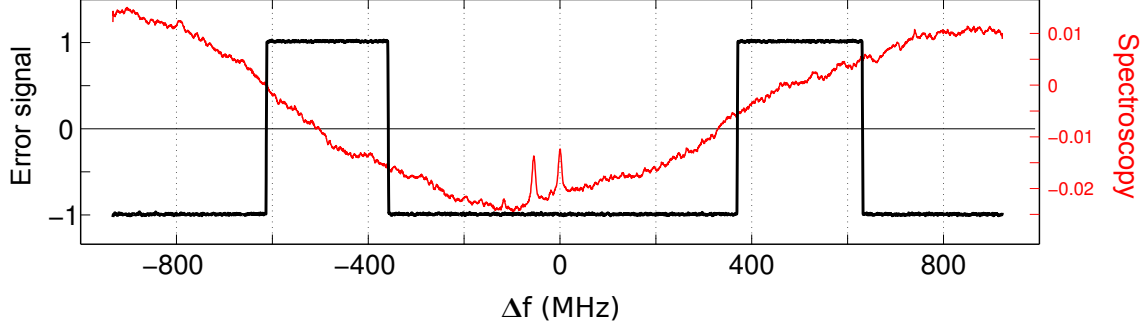


Figure C.2: Black, thick : Typical unfiltered offset lock error signal. Red : simultaneous spectroscopy. The setpoint was 370 MHz

$f_{sample} = 1.2$  GHz. The frequency of this sign change is  $f_{sample} - f_{setpoint}$  and is not extremely stable, thus avoiding it's use for locking. This phenomena have to be kept in mind in the case of high  $f_{setpoint}$  because it reduces the lock capture range.

Once locked, the power beating signal is  $\approx 4$  MHz wide at half height. This width is interpreted to be mainly due to a residual frequency modulation of the etalon lock of the MBR 110

**Possible improvements** The main limitation is the laser linewidth. It can be reduced by adding an AOM at the output of the laser and filtering the high frequency signal of the output of the PLL to perform feedback on the AOM radiofrequency. The bandwidth of an acousto optic modulator being larger than the width of the beating signal, it would allow to reduce the relative laser linewidth.



# Appendix D

## Various

### D.1 Branching ratios

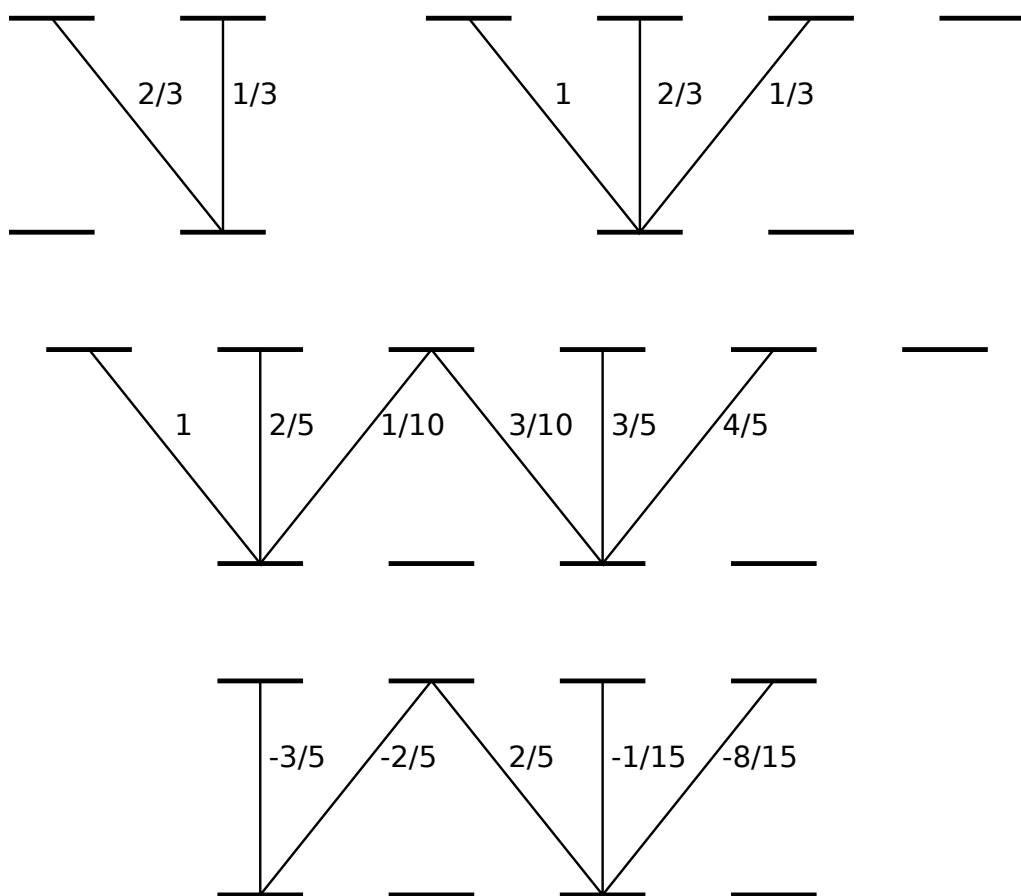


Figure D.1: Clebsch Gordan coefficients for the levels involved in  $\text{Sr}^+$

## D.2 Lifetime and frequencies of low energy levels of Sr+

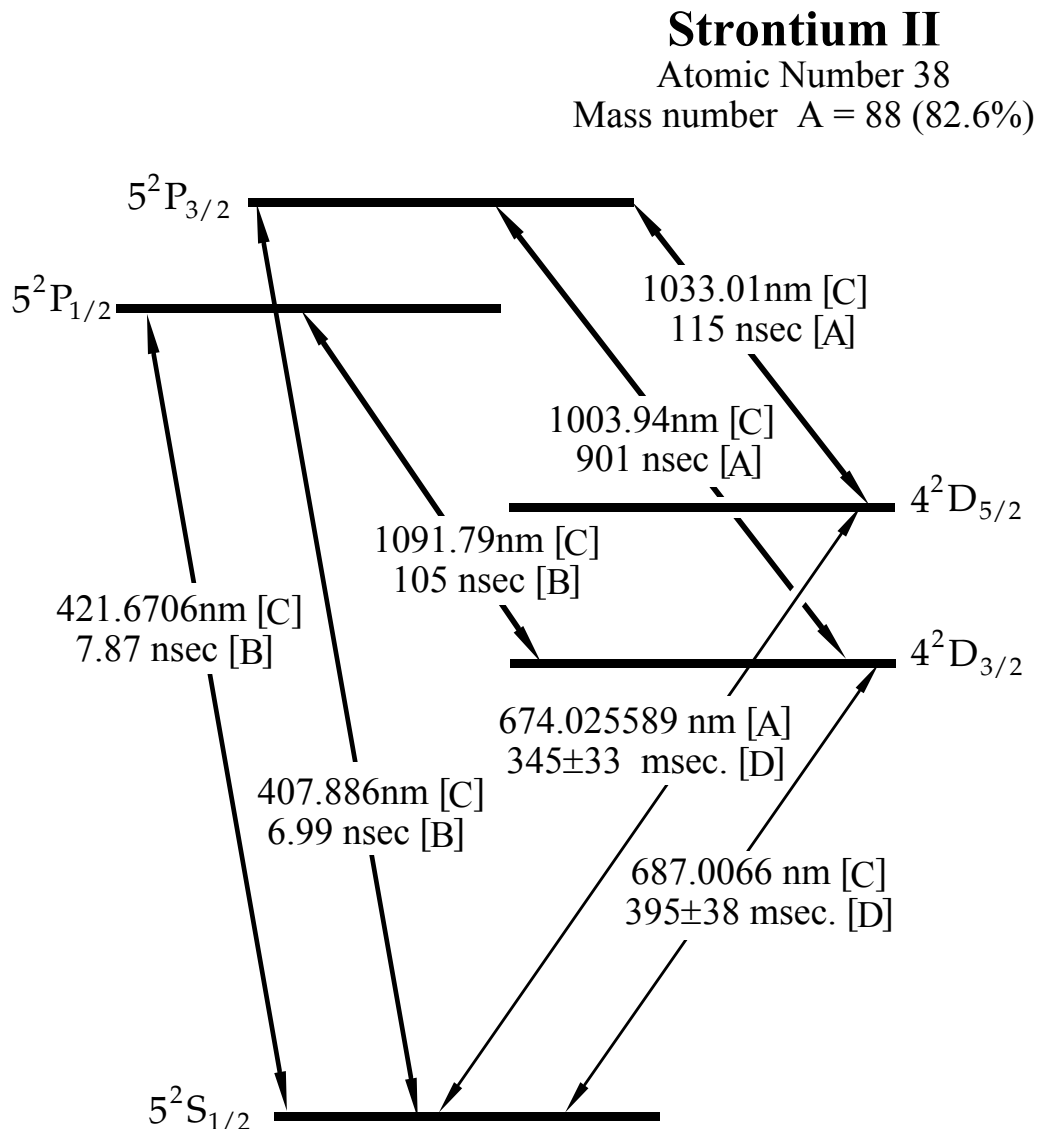


Figure D.2: Sr II transitions from [James 97]

References:

- A: [Barwood 97]
- B: [Gallagher 67]
- C: [Moore 52]
- D: [Gerz 87]

# Bibliography

- [Albert 11] Magnus Albert, Aurelien Dantan & Michael Drewsen. *Cavity electromagnetically induced transparency and all-optical switching using ion Coulomb crystals.* Nat Photon, vol. 5, no. 10, pages 633–636, October 2011.
- [Alheit 96] R. Alheit, K. Enders & G. Werth. *Isotope separation by nonlinear resonances in a Paul trap.* Applied Physics B: Lasers and Optics, vol. 62, pages 511–513, 1996.
- [André 04] A. André, A. S. Sørensen & M. D. Lukin. *Stability of Atomic Clocks Based on Entangled Atoms.* Phys. Rev. Lett., vol. 92, no. 23, page 230801, Jun 2004.
- [Appel 09a] J. Appel, P. J. Windpassinger, D. Oblak, U. B. Hoff, N. Kjærgaard & E. S. Polzik. *Mesoscopic atomic entanglement for precision measurements beyond the standard quantum limit.* Proceedings of the National Academy of Sciences, vol. 106, no. 27, pages 10960–10965, 2009.
- [Appel 09b] Jürgen Appel, Andrew MacRae & A I Lvovsky. *A versatile digital GHz phase lock for external cavity diode lasers.* Measurement Science and Technology, vol. 20, no. 5, page 055302, 2009.
- [Ashkin 70] A. Ashkin. *Atomic-Beam Deflection by Resonance-Radiation Pressure.* Phys. Rev. Lett., vol. 25, no. 19, pages 1321–1324, Nov 1970.
- [Barrett 03] M. D. Barrett, B. DeMarco, T. Schaetz, V. Meyer, D. Leibfried, J. Britton, J. Chiaverini, W. M. Itano, B. Jelenković, J. D. Jost, C. Langer, T. Rosenband & D. J. Wineland. *Sympathetic cooling of  ${}^9\text{Be}^+$  and  ${}^{24}\text{Mg}^+$  for quantum logic.* Phys. Rev. A, vol. 68, page 042302, Oct 2003.
- [Barwood 97] G.P. Barwood, P. Gill, H.A. Klein & W.R.C. Rowley. *Clearly resolved secular sidebands on the  $2S1/2 - 2D5/2$  674-nm clock transition in a single trapped Sr+ ion.* Instrumentation and Measurement, IEEE Transactions on, vol. 46, no. 2, pages 133 –136, apr 1997.
- [Bednorz 11] Adam Bednorz & Wolfgang Belzig. *Fourth moments reveal the negativity of the Wigner function.* Phys. Rev. A, vol. 83, page 052113, May 2011.

- [Benhelm 08] J. Benhelm, G. Kirchmair, C. F. Roos & R. Blatt. *Experimental quantum-information processing with  $^{43}\text{Ca}^+$  ions.* Phys. Rev. A, vol. 77, no. 6, page 062306, Jun 2008.
- [Berkeland 98] D. J. Berkeland, J. D. Miller, J. C. Bergquist, W. M. Itano & D. J. Wineland. *Minimization of ion micromotion in a Paul trap.* Journal of Applied Physics, vol. 83, no. 10, pages 5025–5033, 1998.
- [Berkeland 02] D. J. Berkeland & M. G. Boshier. *Destabilization of dark states and optical spectroscopy in Zeeman-degenerate atomic systems.* Phys. Rev. A, vol. 65, no. 3, page 033413, Feb 2002.
- [Blümel 88] R. Blümel. *Phase transitions of stored laser-cooled ions.* Nature (London), vol. 334, no. 6180, pages 309–313, July 1988.
- [Borghs 83] G. Borghs, P. Bisschop, M. Hove & R. Silverans. *Hyperfine interactions in the alkaline-earth Sr ions by collinear fast beam laser spectroscopy.* Hyperfine Interactions, vol. 15, pages 177–180, 1983.
- [Bowe 99] P. Bowe, L. Hornekær, C. Brodersen, M. Drewsen, J. S. Hangst & J. P. Schiffer. *Sympathetic Crystallization of Trapped Ions.* Phys. Rev. Lett., vol. 82, no. 10, pages 2071–2074, Mar 1999.
- [Buchinger 90] F. Buchinger, E. B. Ramsay, E. Arnold, W. Neu, R. Neugart, K. Wendt, R. E. Silverans, P. Lievens, L. Vermeeren, D. Berdichevsky, R. Fleming, D. W. L. Sprung & G. Ulm. *Systematics of nuclear ground state properties in  $^{78-100}\text{Sr}$  by laser spectroscopy.* Phys. Rev. C, vol. 41, no. 6, pages 2883–2897, Jun 1990.
- [Budker 07] Dmitry Budker & Michael Romalis. *Optical magnetometry.* Nat Phys, vol. 3, no. 4, pages 227–234, April 2007.
- [Burke 05] John H. T. Burke, Ofir Garcia, K. Jeramy Hughes, Brian Livedalen & Charles A. Sackett. *Compact implementation of a scanning transfer cavity lock.* Review of Scientific Instruments, vol. 76, no. 11, page 116105, 2005.
- [Campbell 12] C. J. Campbell, A. G. Radnaev, A. Kuzmich, V. A. Dzuba, V. V. Flambaum & A. Derevianko. *Single-Ion Nuclear Clock for Metrology at the 19th Decimal Place.* Phys. Rev. Lett., vol. 108, page 120802, Mar 2012.
- [Cerè 09] Alessandro Cerè, Florian Wolfgramm, Mario Napolitano & Morgan W. Mitchell. *Narrow-Band Filter for Quantum Light.* In CLEO/Europe and EQEC 2009 Conference Digest, page EA\_P17. Optical Society of America, 2009.

- [Cetina 07] Marko Cetina, Andrew Grier, Jonathan Campbell, Isaac Chuang & Vladan Vuletić. *Bright source of cold ions for surface-electrode traps*. Phys. Rev. A, vol. 76, no. 4, page 041401, Oct 2007.
- [Chou 10] C. W. Chou, D. B. Hume, J. C. J. Koelemeij, D. J. Wineland & T. Rosenband. *Frequency Comparison of Two High-Accuracy Al<sup>+</sup> Optical Clocks*. Phys. Rev. Lett., vol. 104, page 070802, Feb 2010.
- [de Echaniz 08] S. R. de Echaniz, M. Koschorreck, M. Napolitano, M. Kubasik & M. W. Mitchell. *Hamiltonian design in atom-light interactions with rubidium ensembles: A quantum-information toolbox*. Phys. Rev. A, vol. 77, page 032316, Mar 2008.
- [Dehmelt 68] H.G. Dehmelt. *Radiofrequency Spectroscopy of Stored Ions I: Storage*. Advances in Atomic and Molecular Physics, vol. 3, pages 53 – 72, 1968.
- [Dell'Anno 07] F. Dell'Anno, S. De Siena, L. Albano & F. Illuminati. *Continuous-variable quantum teleportation with non-Gaussian resources*. Phys. Rev. A, vol. 76, page 022301, Aug 2007.
- [Deslauriers 06] L. Deslauriers, S. Olmschenk, D. Stick, W. K. Hensinger, J. Sterk & C. Monroe. *Scaling and Suppression of Anomalous Heating in Ion Traps*. Phys. Rev. Lett., vol. 97, page 103007, Sep 2006.
- [DeVoe 02] Ralph G. DeVoe & Christian Kurtsiefer. *Experimental study of anomalous heating and trap instabilities in a microscopic <sup>137</sup>Ba ion trap*. Phys. Rev. A, vol. 65, page 063407, Jun 2002.
- [Drever 83] R. W. P. Drever, J. L. Hall, F. V. Kowalski, J. Hough, G. M. Ford, A. J. Munley & H. Ward. *Laser phase and frequency stabilization using an optical resonator*. Applied Physics B: Lasers and Optics, vol. 31, no. 2, pages 97–105, 1983.
- [Drewsen 98] M. Drewsen, C. Brodersen, L. Hornekær, J. S. Hangst & J. P. Schifffer. *Large Ion Crystals in a Linear Paul Trap*. Phys. Rev. Lett., vol. 81, no. 14, pages 2878–2881, Oct 1998.
- [Drewsen 00] M. Drewsen & A. Brøner. *Harmonic linear Paul trap: Stability diagram and effective potentials*. Phys. Rev. A, vol. 62, page 045401, Sep 2000.
- [Dubessy 09] R. Dubessy, T. Coudreau & L. Guidoni. *Electric field noise above surfaces: A model for heating-rate scaling law in ion traps*. Phys. Rev. A, vol. 80, page 031402, Sep 2009.
- [Dubin 99] Daniel H. E. Dubin & T. M. O'Neil. *Trapped nonneutral plasmas, liquids, and crystals (the thermal equilibrium states)*. Rev. Mod. Phys., vol. 71, pages 87–172, Jan 1999.

- [Dubost 12] B. Dubost, M. Koschorreck, M. Napolitano, N. Behbood, R. J. Sewell & M. W. Mitchell. *Efficient Quantification of Non-Gaussian Spin Distributions*. Phys. Rev. Lett., vol. 108, page 183602, May 2012.
- [Eisert 02] J. Eisert, S. Scheel & M. B. Plenio. *Distilling Gaussian States with Gaussian Operations is Impossible*. Phys. Rev. Lett., vol. 89, page 137903, Sep 2002.
- [Eran Kot 11] Eugene S. Polzik Eran Kot Niels Grønbech-Jensen & Anders S. Sørensen. *Authenticating Non-Classicality*. ArXiv quant-ph/1110.3060, Oct 2011.
- [Eschner 03] Jürgen Eschner, Giovanna Morigi, Ferdinand Schmidt-Kaler & Rainer Blatt. *Laser cooling of trapped ions*. J. Opt. Soc. Am. B, vol. 20, no. 5, pages 1003–1015, May 2003.
- [Filip 08] Radim Filip. *Excess-noise-free recording and uploading of nonclassical states to continuous-variable quantum memory*. Phys. Rev. A, vol. 78, page 012329, Jul 2008.
- [Gallagher 67] Alan Gallagher. *Oscillator Strengths of Ca II, Sr II, and Ba II*. Phys. Rev., vol. 157, pages 24–30, May 1967.
- [Geremia 06] J. M. Geremia, John K. Stockton & Hideo Mabuchi. *Tensor polarizability and dispersive quantum measurement of multilevel atoms*. Phys. Rev. A, vol. 73, page 042112, Apr 2006.
- [Gerz 87] Ch. Gerz, Th. Hilberath & G. Werth. *Lifetime of the 4D3/2 and 4D5/2 metastable states in Sr II*. Zeitschrift für Physik D Atoms, Molecules and Clusters, vol. 5, pages 97–99, 1987.
- [Ghosh 95] Pradip K. Ghosh. Ion traps. Oxford University Press, 1995.
- [Giedke 02] Géza Giedke & J. Ignacio Cirac. *Characterization of Gaussian operations and distillation of Gaussian states*. Phys. Rev. A, vol. 66, page 032316, Sep 2002.
- [Gray 78] H. R. Gray, R. M. Whitley & Jr. C. R. Stroud. *Coherent trapping of atomic populations*. Opt. Lett., vol. 3, no. 6, pages 218–220, Dec 1978.
- [Gross 10] C. Gross, T. Zibold, E. Nicklas, J. Estève & M. K. Oberthaler. *Non-linear atom interferometer surpasses classical precision limit*. Nature, vol. 464, no. 7292, pages 1165–1169, April 2010.
- [Hammerer 10] Klemens Hammerer, Anders S. Sørensen & Eugene S. Polzik. *Quantum interface between light and atomic ensembles*. Rev. Mod. Phys., vol. 82, no. 2, pages 1041–1093, Apr 2010.

- [Hasegawa 00] T. Hasegawa & T. Shimizu. *Removal of irrelevant isotope ions in the presence of laser cooling in a rf trap.* Applied Physics B: Lasers and Optics, vol. 70, pages 867–871, 2000.
- [Hedges 10] Morgan P. Hedges, Jevon J. Longdell, Yongmin Li & Matthew J. Sellars. *Efficient quantum memory for light.* Nature, vol. 465, no. 7301, pages 1052–1056, June 2010.
- [Heinzen 90] D. J. Heinzen & D. J. Wineland. *Quantum-limited cooling and detection of radio-frequency oscillations by laser-cooled ions.* Phys. Rev. A, vol. 42, pages 2977–2994, Sep 1990.
- [Herskind 08] P. Herskind, A. Dantan, M. Langkilde-Lauesen, A. Mortensen, J. Sørensen & M. Drewsen. *Loading of large ion Coulomb crystals into a linear Paul trap incorporating an optical cavity.* Applied Physics B: Lasers and Optics, vol. 93, no. 2, pages 373–379, November 2008.
- [Herskind 09] Peter F. Herskind, Aurelien Dantan, Joan P. Marler, Magnus Albert & Michael Drewsen. *Realization of collective strong coupling with ion Coulomb crystals in an optical cavity.* Nat Phys, vol. 5, no. 7, pages 494–498, July 2009.
- [Hertzberg 10] J. B. Hertzberg, T. Rocheleau, T. Ndukum, M. Savva, A. A. Clerk & K. C. Schwab. *Back-action-evading measurements of nanomechanical motion.* Nat Phys, vol. 6, no. 3, pages 213–217, March 2010.
- [Häffner 05] H. Häffner, F. Schmidt-Kaler, W. Hänsel, C. F. Roos, T. Körber, M. Chwalla, M. Riebe, J. Benhelm, U. D. Rapol, C. Becher & R. Blatt. *Robust entanglement.* Applied Physics B: Lasers and Optics, vol. 81, pages 151–153, 2005.
- [Hilborn 82] R. C. Hilborn. *Einstein coefficients, cross sections, f values, dipole moments and all that.* Am. J. Phys., vol. 50, pages 982–986, 1982.
- [Home 09] Jonathan P. Home, David Hanneke, John D. Jost, Jason M. Amini, Dietrich Leibfried & David J. Wineland. *Complete Methods Set for Scalable Ion Trap Quantum Information Processing.* Science, vol. 325, no. 5945, pages 1227–1230, 2009.
- [Hornekær 02] L. Hornekær & M. Drewsen. *Formation process of large ion Coulomb crystals in linear Paul traps.* Phys. Rev. A, vol. 66, no. 1, page 013412, Jul 2002.
- [Hosseini 11] M. Hosseini, B.M. Sparkes, G. Campbell, P.K. Lam & B.C. Buchler. *High efficiency coherent optical memory with warm rubidium vapour.* Nat Commun, vol. 2, pages 174–, February 2011.

- [Hughes 57] R. H. Hughes. *Isotope Shifts in the Spectra of Strontium*. Phys. Rev., vol. 105, no. 4, pages 1260–1261, Feb 1957.
- [Ichimaru 82] Setsuo Ichimaru. *Strongly coupled plasmas: high-density classical plasmas and degenerate electron liquids*. Rev. Mod. Phys., vol. 54, no. 4, pages 1017–1059, Oct 1982.
- [Itano 98] W. M. Itano, J. J. Bollinger, J. N. Tan, B. Jelenković, X.-P. Huang & D. J. Wineland. *Bragg Diffraction from Crystallized Ion Plasmas*. Science, vol. 279, no. 5351, pages 686–689, 1998.
- [James 97] Daniel F. V. James. *Quantum dynamics of cold trapped ions, with application to quantum computation*. ArXiv quant-ph/9702053, Feb 1997.
- [Ježek 11] Miroslav Ježek, Ivo Straka, Michal Mičuda, Miloslav Dušek, Jaromír Fiurášek & Radim Filip. *Experimental Test of the Quantum Non-Gaussian Character of a Heralded Single-Photon State*. Phys. Rev. Lett., vol. 107, page 213602, Nov 2011.
- [Jost 09] J. D. Jost, J. P. Home, J. M. Amini, D. Hanneke, R. Ozeri, C. Langer, J. J. Bollinger, D. Leibfried & D. J. Wineland. *Entangled mechanical oscillators*. Nature, vol. 459, no. 7247, pages 683–685, June 2009.
- [Katori 99] Hidetoshi Katori, Tetsuya Ido, Yoshitomo Isoya & Makoto Kuwata-Gonokami. *Magneto-Optical Trapping and Cooling of Strontium Atoms down to the Photon Recoil Temperature*. Phys. Rev. Lett., vol. 82, no. 6, pages 1116–1119, Feb 1999.
- [Kendall 58] Maurice G. Kendall & Alan Stuart. *The advanced theory of statistics*. C. Griffin, London, 1958.
- [Kielpinski 02] D. Kielpinski, C. Monroe & D. J. Wineland. *Architecture for a large-scale ion-trap quantum computer*. Nature, vol. 417, no. 6890, pages 709–711, June 2002.
- [Kirilov 09] E. Kirilov & S. Putterman. *2-photon ionization for efficient seeding and trapping of strontium ions*. The European Physical Journal D - Atomic, Molecular, Optical and Plasma Physics, vol. 54, pages 683–691, 2009.
- [Kominis 03] I. K. Kominis, T. W. Kornack, J. C. Allred & M. V. Romalis. *A subfemtesla multichannel atomic magnetometer*. Nature, vol. 422, no. 6932, pages 596–599, April 2003.
- [Koschorreck 10a] M. Koschorreck, M. Napolitano, B. Dubost & M. W. Mitchell. *Quantum Nondemolition Measurement of Large-Spin Ensembles by Dynamical Decoupling*. Phys. Rev. Lett., vol. 105, page 093602, Aug 2010.

- [Koschorreck 10b] M. Koschorreck, M. Napolitano, B. Dubost & M. W. Mitchell. *Sub-Projection-Noise Sensitivity in Broadband Atomic Magnetometry*. Phys. Rev. Lett., vol. 104, page 093602, Mar 2010.
- [Koschorreck 10c] Marco Koschorreck, Mario Napolitano, Brice Dubost, Naeimeh Behbood, Robert Sewell & Morgan W. Mitchell. *Spin Squeezing via Quantum Non-Demolition Measurements in Cold  $^{87}\text{Rb}$  Atomic Ensemble*. In Quantum Electronics and Laser Science Conference, page QThA4. Optical Society of America, 2010.
- [Koschorreck 11] Marco Koschorreck. *Generation of Spin Squeezing in an ensemble of Cold Rubidium 87*. PhD thesis, ICFO - The Institute of Photonic Sciences and Universitat Politècnica de Catalunya, 2011.
- [Kreuter 04] A. Kreuter, C. Becher, G. P. T. Lancaster, A. B. Mundt, C. Russo, H. Häffner, C. Roos, J. Eschner, F. Schmidt-Kaler & R. Blatt. *Spontaneous Emission Lifetime of a Single Trapped  $\text{Ca}^+$  Ion in a High Finesse Cavity*. Phys. Rev. Lett., vol. 92, page 203002, May 2004.
- [Kubasik 09] M. Kubasik, M. Koschorreck, M. Napolitano, S. R. de Echaniz, H. Crepaz, J. Eschner, E. S. Polzik & M. W. Mitchell. *Polarization-based light-atom quantum interface with an all-optical trap*. Phys. Rev. A, vol. 79, page 043815, Apr 2009.
- [Langer 05] C. Langer, R. Ozeri, J. D. Jost, J. Chiaverini, B. DeMarco, A. Ben-Kish, R. B. Blakestad, J. Britton, D. B. Hume, W. M. Itano, D. Leibfried, R. Reichle, T. Rosenband, T. Schaetz, P. O. Schmidt & D. J. Wineland. *Long-Lived Qubit Memory Using Atomic Ions*. Phys. Rev. Lett., vol. 95, no. 6, page 060502, Aug 2005.
- [Leibrandt 09] David R. Leibrandt, Jaroslaw Labaziewicz, Vladan Vuletić & Isaac L. Chuang. *Cavity Sideband Cooling of a Single Trapped Ion*. Phys. Rev. Lett., vol. 103, page 103001, Aug 2009.
- [Lemr 09] Karel Lemr & Jaromír Fiurášek. *Conditional preparation of arbitrary superpositions of atomic Dicke states*. Phys. Rev. A, vol. 79, page 043808, Apr 2009.
- [Lloyd 99] Seth Lloyd & Samuel L. Braunstein. *Quantum Computation over Continuous Variables*. Phys. Rev. Lett., vol. 82, pages 1784–1787, Feb 1999.
- [Longdell 05] J. J. Longdell, E. Fraval, M. J. Sellars & N. B. Manson. *Stopped Light with Storage Times Greater than One Second Using Electromagnetically Induced Transparency in a Solid*. Phys. Rev. Lett., vol. 95, no. 6, page 063601, Aug 2005.

- [Louchet-Chauvet 10] Anne Louchet-Chauvet, Jürgen Appel, Jelmer J Renema, Daniel Oblak, Niels Kjaergaard & Eugene S Polzik. *Entanglement-assisted atomic clock beyond the projection noise limit.* New Journal of Physics, vol. 12, no. 6, page 065032, 2010.
- [Lucas 04] D. M. Lucas, A. Ramos, J. P. Home, M. J. McDonnell, S. Nakayama, J.-P. Stacey, S. C. Webster, D. N. Stacey & A. M. Steane. *Isotope-selective photoionization for calcium ion trapping.* Phys. Rev. A, vol. 69, no. 1, page 012711, Jan 2004.
- [Lvovsky 01] A. I. Lvovsky, H. Hansen, T. Aichele, O. Benson, J. Mlynek & S. Schiller. *Quantum State Reconstruction of the Single-Photon Fock State.* Phys. Rev. Lett., vol. 87, page 050402, Jul 2001.
- [Lybarger 11] Warren E. Lybarger, Julian C. Berengut & John Chiaverini. *Precision measurement of the  $5^2S1/2 - 4^2D5/2$  quadrupole transition isotope shift between  $^{88}Sr^+$  and  $^{86}Sr^+$ .* Phys. Rev. A, vol. 83, no. 5, page 052509, May 2011.
- [Madej 98] A.A. Madej, L. Marmet & J.E. Bernard. *Rb atomic absorption line reference for single Sr+ laser cooling systems.* Applied Physics B: Lasers and Optics, vol. 67, pages 229–234, 1998.
- [Maiwald 09] Robert Maiwald, Dietrich Leibfried, Joe Britton, James C. Bergquist, Gerd Leuchs & David J. Wineland. *Stylus ion trap for enhanced access and sensing.* Nat Phys, vol. 5, no. 8, pages 551–554, August 2009.
- [Margolis 04] H. S. Margolis, G. P. Barwood, G. Huang, H. A. Klein, S. N. Lea, K. Szymaniec & P. Gill. *Hertz-Level Measurement of the Optical Clock Frequency in a Single 88Sr+ Ion.* Science, vol. 306, no. 5700, pages 1355–1358, 2004.
- [Massar 03] S. Massar & E. S. Polzik. *Generating a Superposition of Spin States in an Atomic Ensemble.* Phys. Rev. Lett., vol. 91, page 060401, Aug 2003.
- [Mitchell 98] T. B. Mitchell, J. J. Bollinger, D. H. E. Dubin, X.-P. Huang, W. M. Itano & R. H. Baughman. *Direct Observations of Structural Phase Transitions in Planar Crystallized Ion Plasmas.* Science, vol. 282, no. 5392, pages 1290–1293, 1998.
- [Monroe 95] C. Monroe, D. M. Meekhof, B. E. King, S. R. Jefferts, W. M. Itano, D. J. Wineland & P. Gould. *Resolved-Sideband Raman Cooling of a Bound Atom to the 3D Zero-Point Energy.* Phys. Rev. Lett., vol. 75, pages 4011–4014, Nov 1995.
- [Moore 52] C. E. Moore. Atomic energy levels vol ii. National Bureau of Standards, Washington, 1952.

- [Morigi 00] Giovanna Morigi, Jürgen Eschner & Christoph H. Keitel. *Ground State Laser Cooling Using Electromagnetically Induced Transparency*. Phys. Rev. Lett., vol. 85, pages 4458–4461, Nov 2000.
- [Mortensen 04] A. Mortensen, J. J. T. Lindballe, I. S. Jensen, P. Staanum, D. Voigt & M. Drewsen. *Isotope shifts of the  $4s^2 \ ^1S_0 \rightarrow 4s5p \ ^1P_1$  transition and hyperfine splitting of the  $4s5p \ ^1P_1$  state in calcium*. Phys. Rev. A, vol. 69, no. 4, page 042502, Apr 2004.
- [Mortensen 06] A. Mortensen, E. Nielsen, T. Matthey & M. Drewsen. *Observation of Three-Dimensional Long-Range Order in Small Ion Coulomb Crystals in an rf Trap*. Phys. Rev. Lett., vol. 96, no. 10, page 103001, Mar 2006.
- [Mundt 02] A. B. Mundt, A. Kreuter, C. Becher, D. Leibfried, J. Eschner, F. Schmidt-Kaler & R. Blatt. *Coupling a Single Atomic Quantum Bit to a High Finesse Optical Cavity*. Phys. Rev. Lett., vol. 89, page 103001, Aug 2002.
- [Napolitano 11] M. Napolitano, M. Koschorreck, B. Dubost, N. Behbood, R. J. Sewell & M. W. Mitchell. *Interaction-based quantum metrology showing scaling beyond the Heisenberg limit*. Nature, vol. 471, no. 7339, pages 486–489, March 2011.
- [Neergaard-Nielsen 06] J. S. Neergaard-Nielsen, B. Melholt Nielsen, C. Hettich, K. Mølmer & E. S. Polzik. *Generation of a Superposition of Odd Photon Number States for Quantum Information Networks*. Phys. Rev. Lett., vol. 97, page 083604, Aug 2006.
- [Neuhauser 78] W. Neuhauser, M. Hohenstatt, P. Toschek & H. Dehmelt. *Optical-Sideband Cooling of Visible Atom Cloud Confined in Parabolic Well*. Phys. Rev. Lett., vol. 41, no. 4, pages 233–236, Jul 1978.
- [Nielsen 09] Anne E. B. Nielsen, Uffe V. Poulsen, Antonio Negretti & Klaus Mølmer. *Atomic quantum superposition state generation via optical probing*. Phys. Rev. A, vol. 79, page 023841, Feb 2009.
- [Ostendorf 06] A. Ostendorf, C. B. Zhang, M. A. Wilson, D. Offenberg, B. Roth & S. Schiller. *Sympathetic Cooling of Complex Molecular Ions to Millikelvin Temperatures*. Phys. Rev. Lett., vol. 97, page 243005, Dec 2006.
- [Ourjoumtsev 06] Alexei Ourjoumtsev, Rosa Tualle-Brouri, Julien Laurat & Philippe Grangier. *Generating Optical Schrödinger Kittens for Quantum Information Processing*. Science, vol. 312, no. 5770, pages 83–86, 2006.

- [Ourjoumtsev 07] Alexei Ourjoumtsev, Hyunseok Jeong, Rosa Tualle-Brouri & Philippe Grangier. *Generation of optical ‘Schrödinger cats’ from photon number states.* Nature, vol. 448, no. 7155, pages 784–786, August 2007.
- [Piro 11] N. Piro, F. Rohde, C. Schuck, M. Almendros, J. Huwer, J. Ghosh, A. Haase, M. Hennrich, F. Dubin & J. Eschner. *Heralded single-photon absorption by a single atom.* Nat Phys, vol. 7, no. 1, pages 17–20, January 2011.
- [Prestage 89] J. D. Prestage, G. J. Dick & L. Maleki. *New ion trap for frequency standard applications.* Journal of Applied Physics, vol. 66, no. 3, pages 1013–1017, 1989.
- [Prestage 91] J. D. Prestage, A. Williams, L. Maleki, M. J. Djomehri & E. Harabetian. *Dynamics of charged particles in a Paul radio-frequency quadrupole trap.* Phys. Rev. Lett., vol. 66, no. 23, pages 2964–2967, Jun 1991.
- [Ralph 03] T. C. Ralph, A. Gilchrist, G. J. Milburn, W. J. Munro & S. Glancy. *Quantum computation with optical coherent states.* Phys. Rev. A, vol. 68, page 042319, Oct 2003.
- [Removille 09a] S. Removille. *Vers une mémoire quantique dans les ions piégés.* PhD thesis, Université Paris Diderot - Paris 7, septembre 2009.
- [Removille 09b] S. Removille, R. Dubessy, Q. Glorieux, S. Guibal, T. Coudreau, L. Guidoni & J. P. Likforman. *Photoionisation loading of large Sr+ ion clouds with ultrafast pulses.* Applied Physics B: Lasers and Optics, 2009.
- [Rosenband 08] T. Rosenband, D. B. Hume, P. O. Schmidt, C. W. Chou, A. Brusch, L. Lorini, W. H. Oskay, R. E. Drullinger, T. M. Fortier, J. E. Stalnaker, S. A. Diddams, W. C. Swann, N. R. Newbury, W. M. Itano, D. J. Wineland & J. C. Bergquist. *Frequency Ratio of Al+ and Hg+ Single-Ion Optical Clocks; Metrology at the 17th Decimal Place.* Science, vol. 319, no. 5871, pages 1808–1812, 2008.
- [Ryjkov 05] Vladimir L. Ryjkov, XianZhen Zhao & Hans A. Schuessler. *Simulations of the rf heating rates in a linear quadrupole ion trap.* Phys. Rev. A, vol. 71, no. 3, page 033414, Mar 2005.
- [Schawlow 82] Arthur L. Schawlow. *Spectroscopy in a new light.* Rev. Mod. Phys., vol. 54, pages 697–707, Jul 1982.
- [Schmidt-Kaler 03] F Schmidt-Kaler, S Gulde, M Riebe, T Deusche, A Kreuter, G Lancaster, C Becher, J Eschner, H Haffner & R Blatt. *The coherence*

- of qubits based on single Ca + ions.* Journal of Physics B: Atomic, Molecular and Optical Physics, vol. 36, no. 3, page 623, 2003.
- [Schnabel 10] Roman Schnabel, Nergis Mavalvala, David E. McClelland & Ping K. Lam. *Quantum metrology for gravitational wave astronomy.* Nat Commun, vol. 1, pages 121–, November 2010.
- [Schneider 05] T. Schneider, E. Peik & Chr. Tamm. *Sub-Hertz Optical Frequency Comparisons between Two Trapped  $^{171}\text{Yb}^+$  Ions.* Phys. Rev. Lett., vol. 94, page 230801, Jun 2005.
- [Schubert 89] Michael Schubert, Ingo Siemers & Rainer Blatt. *Line shape of three-level ions in Paul traps.* Phys. Rev. A, vol. 39, no. 10, pages 5098–5105, May 1989.
- [Seymour-Smith 10] Nicolas Seymour-Smith, Peter Blythe, Matthias Keller & Wolfgang Lange. *Fast scanning cavity offset lock for laser frequency drift stabilization.* Rev. Sci. Instrum., vol. 81, no. 7, page 075109, 2010.
- [Shah 10] V. Shah, G. Vasilakis & M. V. Romalis. *High Bandwidth Atomic Magnetometry with Continuous Quantum Nondemolition Measurements.* Phys. Rev. Lett., vol. 104, no. 1, page 013601, Jan 2010.
- [Shchukin 05] E. Shchukin, Th. Richter & W. Vogel. *Nonclassicality criteria in terms of moments.* Phys. Rev. A, vol. 71, page 011802, Jan 2005.
- [Shiner 07] A.D. Shiner, A.A. Madej, P. Dubé & J.E. Bernard. *Absolute optical frequency measurement of saturated absorption lines in Rb near 422nm.* Applied Physics B: Lasers and Optics, vol. 89, pages 595–601, 2007.
- [Shu 10] G. Shu, N. Kurz, M. R. Dietrich & B. B. Blinov. *Efficient fluorescence collection from trapped ions with an integrated spherical mirror.* Phys. Rev. A, vol. 81, page 042321, Apr 2010.
- [Shu 11] Gang Shu, Chen-Kuan Chou, Nathan Kurz, Matthew R. Dietrich & Boris B. Blinov. *Efficient fluorescence collection and ion imaging with the “tack” ion trap.* J. Opt. Soc. Am. B, vol. 28, no. 12, pages 2865–2870, Dec 2011.
- [Silverans 88] R. E. Silverans, P. Lievens, L. Vermeeren, E. Arnold, W. Neu, R. Neugart, K. Wendt, F. Buchinger, E. B. Ramsay & G. Ulm. *Nuclear Charge Radii of  $^{78-100}\text{Sr}$  by Nonoptical Detection in Fast-Beam Laser Spectroscopy.* Phys. Rev. Lett., vol. 60, pages 2607–2610, Jun 1988.
- [Sinclair 01] A. G. Sinclair, M. A. Wilson & P. Gill. *Improved three-dimensional control of a single strontium ion in an endcap trap.* Optics Communications, vol. 190, no. 1-6, pages 193 – 203, 2001.

- [Slattery 80] W. L. Slattery, G. D. Doolen & H. E. DeWitt. *Improved equation of state for the classical one-component plasma.* Phys. Rev. A, vol. 21, no. 6, pages 2087–2095, Jun 1980.
- [Slodička 10] L. Slodička, G. Hétet, S. Gerber, M. Hennrich & R. Blatt. *Electromagnetically Induced Transparency from a Single Atom in Free Space.* Phys. Rev. Lett., vol. 105, page 153604, Oct 2010.
- [Sondermann 07] M. Sondermann, R. Maiwald, H. Konermann, N. Lindlein, U. Peschel & G. Leuchs. *Design of a mode converter for efficient light-atom coupling in free space.* Applied Physics B: Lasers and Optics, vol. 89, pages 489–492, 2007.
- [Steck 03] D. A. Steck. *Rubidium 87 D line data.* <http://steck.us/alkalidata/>, 2003.
- [Stenholm 86] Stig Stenholm. *The semiclassical theory of laser cooling.* Rev. Mod. Phys., vol. 58, pages 699–739, Jul 1986.
- [Sunaoshi 93] H. Sunaoshi, Y. Fukashiro, M. Furukawa, M. Yamauchi, S. Hayashibe, T. Shinozuka, M. Fujioka, I. Satoh, M. Wada & S. Matsuki. *A precision measurement of the hyperfine structure of  $^{87}\text{Sr}^+$ .* Hyperfine Interactions, vol. 78, pages 241–245, 1993.
- [Takahashi 08] Hiroki Takahashi, Kentaro Wakui, Shigenari Suzuki, Masahiro Takeoka, Kazuhiro Hayasaka, Akira Furusawa & Masahide Sasaki. *Generation of Large-Amplitude Coherent-State Superposition via Ancilla-Assisted Photon Subtraction.* Phys. Rev. Lett., vol. 101, page 233605, Dec 2008.
- [Tanaka 07] U. Tanaka, I. Morita & S. Urabe. *Selective loading and laser cooling of rare calcium isotope  $^{43}\text{Ca}^+$ .* Applied Physics B: Lasers and Optics, vol. 89, pages 195–200, 2007.
- [Tey 08] Meng Khoon Tey, Zilong Chen, Syed Abdullah Aljunid, Brenda Chng, Florian Huber, Gleb Maslennikov & Christian Kurtsiefer. *Strong interaction between light and a single trapped atom without the need for a cavity.* Nat Phys, vol. 4, no. 12, pages 924–927, December 2008.
- [Tóth 10] Géza Tóth & Morgan W Mitchell. *Generation of macroscopic singlet states in atomic ensembles.* New Journal of Physics, vol. 12, no. 5, page 053007, 2010.
- [Toyoda 01] K. Toyoda, H. Kataoka, Y. Kai, A. Miura, M. Watanabe & S. Urabe. *Separation of laser-cooled  $^{42}\text{Ca}^+$  and  $^{44}\text{Ca}^+$  in a linear Paul trap.* Applied Physics B: Lasers and Optics, vol. 72, pages 327–330, 2001.

- [Wakui 07] Kentaro Wakui, Hiroki Takahashi, Akira Furusawa & Masahide Sasaki. *Photon subtracted squeezed states generated with periodically poled KTiOPO<sub>4</sub>*. Opt. Express, vol. 15, no. 6, pages 3568–3574, Mar 2007.
- [Wenger 04] Jérôme Wenger, Rosa Tualle-Brouri & Philippe Grangier. *Non-Gaussian Statistics from Individual Pulses of Squeezed Light*. Phys. Rev. Lett., vol. 92, page 153601, Apr 2004.
- [Wilpers 02] G. Wilpers, T. Binnewies, C. Degenhardt, U. Sterr, J. Helmcke & F. Riehle. *Optical Clock with Ultracold Neutral Atoms*. Phys. Rev. Lett., vol. 89, no. 23, page 230801, Nov 2002.
- [Wolfgramm 10a] Florian Wolfgramm, Alessandro Cerè, Federica A. Beduini, Ana Predojević, Marco Koschorreck & Morgan W. Mitchell. *Squeezed-Light Optical Magnetometry*. Phys. Rev. Lett., vol. 105, page 053601, Jul 2010.
- [Wolfgramm 10b] Florian Wolfgramm, Alessandro Cerè & Morgan W. Mitchell. *NOON states from cavity-enhanced down-conversion: high quality and super-resolution*. J. Opt. Soc. Am. B, vol. 27, no. 6, pages A25–A29, Jun 2010.
- [Wolfgramm 11] Florian Wolfgramm, Yannick A. de Icaza Astiz, Federica A. Beduini, Alessandro Cerè & Morgan W. Mitchell. *Atom-Resonant Heralded Single Photons by Interaction-Free Measurement*. Phys. Rev. Lett., vol. 106, page 053602, Feb 2011.
- [Zhao 09a] Bo Zhao, Yu-Ao Chen, Xiao-Hui Bao, Thorsten Strassel, Chih-Sung Chuu, Xian-Min Jin, Jorg Schmiedmayer, Zhen-Sheng Yuan, Shuai Chen & Jian-Wei Pan. *A millisecond quantum memory for scalable quantum networks*. Nat Phys, vol. 5, no. 2, pages 95–99, February 2009.
- [Zhao 09b] R. Zhao, Y. O. Dudin, S. D. Jenkins, C. J. Campbell, D. N. Matsukevich, T. A. B. Kennedy & A. Kuzmich. *Long-lived quantum memory*. Nat Phys, vol. 5, no. 2, pages 100–104, February 2009.